Analog cosmology with two-fluid systems

Zack Fifer

School of Mathematical Sciences

Thesis submitted for the degree of Doctor of Philosophy
at the University of Nottingham

Submitted on December 20th 2021

Prof. Gregory A. Lawrence External Examiner
Prof. Gregor Tanner Internal Examiner

Abstract

Analog models in physics utilize a conceptual metaphore and a mathematical similarity to describe one system in terms of another. In this thesis, we will present the work that has been done regarding a time-dependent analog examining classical fluid interface waves in order to test predictions from cosmology. We will first detail theoretical work regarding interface waves in a strong-gradient magnetic field, conceived to simulate cosmological inflation, and constituting the first proposal for analog cosmology using interface waves. Motivated by this proposal we will then shift our focus towards parametric resonance, a process by which interface waves are exponentially amplified when coupled to an oscillating gravitational field.

We outline an experiment designed to study the effective field theory of the interface, subject to parametric amplification. In this, we demonstrate that it is possible to conduct hundreds of nearly identical experiments while carefully controlling and monitoring the mechanical, optical, chemical, and environmental conditions with previously unachievable levels of precision. Our measurements of the exponential growth and damping rates for the interface waves are believed to be the most precise ever reported. The precise repetitions in the experiment further allow us to comment on the distribution of initial state at sub-micrometer amplitudes, introduce a classical two-mode squeezing model to characterize the linear statistical evolution of the model, and we present preliminary results characterizing the degree of nonlinearity in the system.

Our results show that it is possible to control and interact with two-fluid systems to the accuracy needed to mimic and investigate in depth cosmological processes in a controlled laboratory environment. At the heart of this thesis is the desire to gain a deeper understanding of effective or emergent field theories. Our vision is to establish a fluid interface metrology approach to drive theoretical developments in both, the effective field theories in fluids and cosmology alike.

Acknowledgements

First of all, I would like to thank my advisor, Silke for her continued patience and commitment to my success in this endeavor; during the first difficult year, and through the long periods of experimental refinement. Silke took me under her wing during a summer project in 2015, and has encouraged me since then. I have learned a great deal from our time together, and I hope that she feels the same way.

From our group members and collaborators, I would like to thank Sam and Theo, for their discussions early on, as well as August and Steffen for their help in the past few years. Thank you to Sebastian for your continued help and advice from the very start right through to the end. From our collaborators, I would like to thank Tasos for his role in setting up the 3D printing project back in 2015, and for his discussions regarding the cosmological theory. Thank you to Richard and Naresh for all of your experimental advice, especially for Richard's suggestion to incorporate springs in the early shaker design. Finally, I would like to thank Renaud Parentani. I only knew and worked with Renaud for a short time, however his enthusiastic correspondences were a source of encouragement during a period when I really needed it.

To the technical support staff at the University of Nottingham Physics department, I would like to extend a blanket of gratitude. Without the almost daily support from Pete, Sue, Melvin, Nick, and too many others to name, everything would grind to a halt almost immediately. A special thanks as well to the engineering support staff for building and testing our crazy ideas, especially Terry who knew from the start that the shaker would not work without air bearings, Tommy and Sionnach for always helping us out on short-notice, especially with 3D printing.

Likewise, a tremendous thanks to Ian, Andy, and Jonathan in the electronics support staff. Not only did you help us turn our half-baked electrical ideas into functioning devices, but you also took the time to teach us along the way, and this extra effort was invaluable. Without your support, nearly every experiment in the lab would be driven by hand cranks, measured by eye with rulers, and recorded with a pen and paper.

I would like to extend a special thanks to my labmate Vitor. Despite the fact that this experiment started years before your arrival, the results that we obtained are as much due to your efforts as they are mine. Aside from the

hundreds of hours that you put into understanding and perfecting the chemistry for the final system, understanding and eliminating the inconsistencies in the shaker, quantifying the errors in the measurements, and helping to improve... everything in the setup, you have been a true source of support and inspiration to me since the moment we started together. You are one of the most talented and capable people that I have ever had the pleasure to meet, and I already miss working with you every day.

Finally, I would like to thank my family. To my mother and father back home, thank you for always believing in my ambitions, for teaching me the value of work and imagination, and for understanding when I told you I was starting school an ocean away. Thank you to my sisters for their emotional support, and my brother for his help with all things chemistry. To my sons, Julian and Theodore, thank you for your patience when Daddy was thinking about work while we were playing, and for all of the hugs that helped me on the days that I didn't think I had the energy.

And thank you to my partner Julia. Since the moment that I met you, you have made my life more complete, and I owe every bit of progress that I have made since that day to you, and the purpose that you give to me. Without the superhuman levels of support that you provided, the hours of sleep that you sacrificed, the countless hours of work that you put supplied in order to ensure that our family thrived, even though I have only been half-present for these past five years... Without all of this, and everything else that you have done for us, there would have been no reason to start in the first place. All of that said, I want to be very clear: I could not have done any of this without you.

Acronyms

FLRW (Friedmann–Lemaître–Robertson–Walker)
BEC (Bose–Einstein condensate)
ODE (ordinary differential equation)
FFT (fast Fourier transform)
FTP (Fourier transform profilometry)
LED (light emitting diode)
QFT (quantum field theory)
CWT (continuous wavelet transform)
PIV (pixel intensity value)
SNR (signal to noise ratio)
qSNR (signal to noise ratio, due to quantization error)
RMS (root mean square)
FIR (finite impulse response)

Contents

Chapter 1

Introduction

The question of how the universe began is a very universal one. Physical cosmology attempts to answer this question in a rigorous way. The formulation of modern physical cosmology started in 1915 with the publication of Einstein's general relativity, a radically new theory for gravity. Within this new framework the gravitational field is encoded in a spacetime geometry or metric [1, 2]. This metric contains information regarding distances and spacetime curvature, and is related to the density of matter and energy via the Einstein field equations. In the 1920s, Hubble's measurements of the redshift of distant galaxies provided evidence that the universe was expanding [3]. In the same decade, the Friedmann-Lemaitre-Robertson-Walker (FLRW) metric was developed, and in the 1930s, shown to be the only solution of Einstein's field equations for a spatially homogeneous and isotropic expanding universe [2].

The expanding FLRW spacetime matched the observations of Hubble, however it was soon discovered that the universe was too homogeneous given that regions of the early universe must have been causally disconnected. This is referred to as the Horizon Problem. Further, theories suggested that the curvature of an expanding universe would be extremely sensitive to initial conditions. This is called the Flatness Problem. In 1980, these problems were solved by Guth and Starobinsky independently, by incorporating a brief period during which the universe underwent an exponential growth or inflation into the model [4, 5]. Inflation proposes that each of the three spacial dimensions in our universe is expanding by a factor of e^{60} within a time interval of 10^{-33}s. By this process initially small perturbations get amplified and converted to density fluctuations, eventually leading to the observed large-scale

structure of the universe [1].

The rapid expansion of the universe in the inflation model is driven by a scalar field known as the inflaton, and at the end of inflation it is believed that this begins oscillating. Other fields coupled to the inflaton experience a sinusoidal modulation in frequency, and for certain fields this results in exponential amplification. This phase of the early universe is known as *preheating* [6], and the phenomenon responsible for the exponential amplification of coupled fields is known as *parametric resonance* [7, 8].

Inflation and preheating are elegant, albeit exotic solutions which make modern cosmology compatible with observations. Because of the importance and impossibility of observing inflation in our own universe, we explore the possibility of studying this extraordinary process in a commonplace system encountered in everyday life, namely fluid interfaces at room temperature and pressure. To mimic inflation, we introduced a system consisting of two immiscible fluids moving through a strong magnetic field in the bore of a superconducting magnet. By precisely controlling the propagation speed of the interface waves, we can capture the essential dynamics of inflationary fluctuations.

In order to establish the analogy between fluids and early universe cosmology on a rigorous footing, it is essential to have a deep understanding of the theory of interface waves. The linear theory of traveling waves is generally credited to Airy (1841) [9]. In his analysis, Airy was able to find the correct dispersion relation for small amplitude waves propagating on an open channel flow. The dispersion relation mathematically relates the wavelengths and the frequency of the oscillations for the wave considered, and allows one to accurately predict the wave's propagation speed. It was found that the frequency depends not only on the gravitational acceleration, but also on the hyperbolic tangent of the fluid depth divided by the wavelength. This is in stark contrast to most other wave systems, where the frequency and wavelength have a polynomial relationship. The usual form of this dispersion relation is generally the first indication of the complexities encountered when examining interface waves theoretically.

While Airy described waves accurately in some regimes, at sufficiently short wavelengths small scale effects due to surface tension become important. This scale is commonly referred to as the capillary-length, specified by the ratio of the coefficient of surface tension and the force per unit volume due to gravity. When the ratio is large, gravitational effects can be neglected.

When the ratio is of order one, both forces must be taken into account [10]. The first publication of the dispersion relation for gravity-capillary waves was by Thompson (later Lord Kelvin) in 1871 [10, 11].

The theories of Airy and Thompson apply to inviscid and irrotational, and in this sense idealized or Platonic fluids. In reality, the closer one looks, the more complex interface waves become. Especially at small scales, one must begin to include viscous dissipation, boundary layers, nonlinearities, and meniscus [1] effects. Feynmann summarizes the familiarity and complexity of water-waves nicely: "Now, the next waves of interest, that are easily seen by everyone and which are usually used as an example of waves in elementary courses, are water waves. As we shall soon see, they are the worst possible example, because they are in no respects like sound and light; they have all the complications that waves can have [12]."

In order to develop a cosmology simulator based on two-fluid systems, a comprehensive understanding of the complications and complexities for the effective field theory of the interface dynamics is essential. We designed and implemented an experiment with an unprecedented level of repeatably and precision in order to test the effective field theory of interface fluctuations with hitherto unseen accuracy. In the chapters that follow we will demonstrate that despite the complications mentioned above, we are not only able to make predictions using theories from cosmology, but these theories are observable in a precision experiment.

1.1 Analog Gravity

The origin story of analog gravity goes as follows[13]: In 1972, Bill Unruh was giving a public lecture on black holes, and used a familiar example of a waterfall in order to explain the concept of a black hole horizon. In the analogy, the continuous stream of water falls faster than sound can propagate, creating an effective horizon which only allows sound to travel in one direction. The analogy was put on solid theoretical grounds in 1980, when Unruh realized that the linear equations for sound propagating in a flowing medium matched the equations for a massless scalar field propagating in a general curved spacetime background.

[1] The meniscus describes the curvature of the interface waves at the solid boundaries, and is due to the interaction energy between each fluid and the solid in question.

Unruh raised the possibility of employing the analogue system exhibiting an effective black hole horizon to study black hole evaporation, a process by which a black hole emits thermal radiation, as predicted by Hawking [14]. Unruh's vision was to use the introduced analog system to bring the elusive Hawking proccess, usually found in remote parts of the universe, into a controlled laboratory environment. The advantage of an analog experiment is perhaps best stated by Unruh himself: "Does the thermal radiation emission by a dumb hole [2] survive the generalization of hydrodynamics to a fully atomic description of the fluid? If it does not, then one has no faith that the Hawking effect would survive a fully quantum treatment of gravity [13]."

This perhaps simple analogy started a whole new line of research. To this end, a large variety of systems have been proposed, including the original acoustic analog [15, 16, 17], interface waves [18], acoustics waves in BECs [19, 20, 21, 22], ripplons in superfluid helium [23, 24], and electromagnetic waves in dielectric media [25, 26]. For a more comprehensive list, and for an excellent introduction to analog gravity in general, see [21].

While the field of analog gravity is built on the idea of turning abstract ideas from field theory on curved spacetimes into reality, the experimental efforts only started relatively recently. Arguably, one of the most experimentally fruitful analog systems for black hole phenomena employ interface waves. Starting with the first experimental observation of Hawking radiation in [27], interface wave analogs have shown remarkable promise in the investigation of other black hole phenomena. In 2017, the first observation of superradiant scattering was made in a bathtub vortex [28]. In the same system, a black hole ringdown was observed in 2018 [29] and a backreaction with the background fluid flow was observed in 2021 [30].

Also relevant to this thesis however, are time-dependent analogs for investigating cosmological scenarios. The investigation of analog simulators for cosmology has been much more limited in comparison to analog black holes. Most have considered implementation in BECs on theoretical grounds, e.g.[31, 32, 33, 34, 35, 36], though in the past decade several experiments have been reported. In 2012, signatures of the analog Dynamical Casimir effect [3] were observed in a BEC [37], and in 2013 Sakharov Oscillations [4] were ob-

[2]Dumb, meaning mute; sound can enter but not escape.

[3]The dynamic Casimir effect predicts the production of particles in the presence of an accelerating mirror.

[4]Sakharov oscillations correspond to a multi-peak structure in the power spectrum of the cosmic microwave background radiation left over from the Big Bang. They are due to

served in a superfluid [38]. Later, in 2018, phonon production and red-shift due to a rapidly expanding BEC ring was observed [39] in an inflationary analog. While this experiment simulated the expansion of the early universe by directly expanding the BEC, this strategy dillutes the condensate, and it is impossible to maintain this type of expansion for long [40]. Another strategy is to modify the propagation speed of a wave, which effectively modulates the system size by changing the distance it can propagate in a given time.

This thesis will focus on two interrelated fluid-phenomenon, touching on diamagnetic levitation and focusing on parametric resonance. In either case, we have an effective modulation of the gravitational acceleration, which alters the dispersion relation for the interface waves in such a way that the propagation speed becomes time dependent. The fluid system examined in this thesis represents the first theoretical and experimental demonstration of a cosmological analog using interface waves. In addition to being the first time-dependent analog, fluid systems on a large scale (such as the scales found in [27, 28, 29, 30]) with wavelengths on the order of one meter behave very differently than fluid systems on the centimeter scale. Surface tension and meniscus effects alter the boundary conditions of the fluid [41, 42], boundary layer effects may need to be taken into account when calculating the dispersion relation [43, 44], and predicting the rate of dissipation in the system becomes highly nontrivial [45].

1.2 Diamagnetic levitation and parametric resonance.

Levitation experiments which demonstrated that stable levitation is possible in a solenoidal magnetic field were first demonstrated by Simon and Geim [46] using a 16T superconducting magnet. In these experiments, diamagnetic graphite, water droplets, and even a living frog were levitated within certain regions of the solenoidal field.

The zones of stability within the solenoid were later calculated by Berry and Geim [47], providing rigorous theory to back up the experiments. Later experiments (more pertinent to this thesis) explored fluid physics phenomena for systems which allowed the effective gravitation acceleration to be modulated in time. In particular, investigations were made regarding the

acoustic pressure waves in the early universe.

stabalization of the Rayleigh-Taylor instability (in which a heavy liquid is supported above a less dense liquid in an unstable equillibrium) in rotating systems [48], and in the predicted fissure of levitating, rotating water droplets [49]. In this spirit, Chapter 2 outlines a proposal to investigate phenomena in analog cosmology induced by a system mimicing exponential inflation in a strong-gradient magnetic field [50]. It was this investigation which motivated the experiment detailed in the rest of this thesis.

Paremetric resonance offered a promising starting point for these investigations. This phenomenon, studied by Faraday in 1831, considers the rapid growth of standing waves from a seeminly flat interface in a vessel of fluid undergoing vertical oscillations [51]. When the entire vessel oscillates vertically, the motion acts to modulate the acceleration due to gravity. The mathematical description of this includes an oscillating *parameter* in the equation of motion, and when the oscillation is large enough, this leads to *parametric resonance*. This behavior was first put on solid theoretical ground by Benjamin and Ursell in 1954, when they demonstrated that the oscillation in the gravitational acceleration entered Airy's dispersion relation for linear waves, and that each wavelength in the system corresponded to a different parametric equation [52]. This theory predicts that at low amplitudes the waves would undergoe exponential amplification, and corresponds to a period of initial growth before nonlinear interactions distribute the energy throughout each of the eigenmodes in the system. At late times, one observes a standing wave pattern with a relatively fixed amplitude [51, 52].

Since this theory was published, a large number of experimental and theoretical investigations have been conducted. In the words of Miles and Henderson: "Faraday waves have been of special interest in recent years as a (possibly) tractable problem in fluid mechanics to which the techniques of modern bifurcation and chaos theory are applicable after a normal-mode expansion [53]." The seeming tractability of the problem is rather deceptive. The most notable leap in theory was by Kumar and Tuckerman (1994), who used a more comprehensive fluid model by Chandrasekhar [43]. The theory of Chandrasekhar incorporates viscous boundary layers at the top and bottom of the fluid container, as well as at the fluid interface. While this did lead to an improvement in stability predictions, matches between theory and experiment are still somewhat sparse [53], and it seems that there is always one more detail left unaccounted for.

In the system presented for example, even full hydrodynamic simulations are not possible without additional information. The surface tension between

the fluids creates a meniscus at the inner and outer radii of the fluid vessel. Not only is the shape of this meniscus dependent on the gravitational acceleration in the system, but the contact angle between the fluid-fluid interface and the vessel also exhibits a form of hysteresis [54]. This dynamic contact angle prevents an accurate prediction of the wavenumbers in the system, which in turn prevents an accurate prediction of the system's response to parametric oscillations.

1.3 Overview

The theory presented in [50] was the first to propose a cosmological analog utilizing interface waves. In it, we presented the idea of creating an exponential expansion of the analog metric, mimicking inflation. By utilizing a strong-gradient magnetic field used in previous fluid physics experiments [48, 49], we demonstrated that it was possible to exponentially change the effective gravity in a two-fluid system from approximately 200 ms^{-2} to 0 ms^{-2} within a 2s interval.

Beginning as a humble petri dish taped to a large speaker, the experiment underwent a complete redesign of the oscillation apparatus, the detection method, three iterations of fluid cell designs, and months of work trying to come to grips with wavelet analysis. The experiment presented in this thesis has grown into something which will (hopefully) be of interest to both the analog gravity and fluid physics communities. We believe that the measurements that we made of the exponential growth and damping rates of the interface waves in our system are the most precise ever reported. Further, we believe that the unprecedented repeatability and precision of our experiment enables us to explore statistical predictions from cosmological theories in our fluid system, opening the way to future analog investigations of cosmological phenomena that have previously not been possible.

The thesis is organized as follow:

- In Chapter 2, we will present and develope the original analog inflation simulator that was first published in [50]. The work presented in this chapter represents the first work investigating the potential of an interface wave analog for cosmology. We will then make some comments regarding the importance of dissipation in the system, and present some new predictions.

- In Chapter 3, we will develope the fluid physics equations leading to the analogy in a different direction, focusing on parametric resonance. While the existing literature focuses on finding stable and unstable experimental parameters, we will extend the analysis in order to obtain predictions for the parametric amplification rate. Several theories will be developed and a phenomenological approach will be discussed.

- In Chapter 4, the experimental setup and methodology will be presented. This begins with an aparatus hereafter referred to as *the shaker*, designed to produce vertical oscillations and currently believed to be the most precise ever produced. We will then describe the detection method for the interface waves, optimized according to a new analysis presented in appendix A. This is followed by a description of the automization process, and finally the fluid cell, a purpose-built vessel which allows a repeatable, standardized filling procedure for the fluids used.

- In Chapter 5, the analytic methods used to describe the system and extract information are presented. This includes a mapping from the real-valued height field, and a novel implementation of wavelets in order to obtain the complex eigenmodes commonly used in the analog field theory. We close the chapter with a detailed description of the statistical quantities from cosmology, wherein we extend the existing predictions in order to account for a finite number of measurements.

- In Chapter 6, we present the results of the shaker experiment. Starting with the parameters most relevant to the fluid physics theories, we detail first the repeatability and precision of the experiment. Then, the exponential amplification rate, the dissipation rate, and an approximate initial amplitude for the waves considered are presented. In the second half, results pertinent to the analogy are presented, with a focus on classical two-mode squeezing.

1.4 Statement of originality

Below is an explaination of which portions of this thesis represent original work by the author, which portions were done in collaboration, and which

portions are the work of other members of the group and or physics department at the University of Nottingham.

- Chapter 2 is based on the publication in [50]. The derivation of the analog wave equation and the results in this chapter are the result of my own work as principal investigator. It also contains recent simulations conducted by a group memmber.

- Chapter 3 is my own interpretation, and in sections, (minor) extension of theories presented in the existing literature. Most of the work is based off of Landau and Lifshitz [10], Chandrasekhar [44], Kumar and Tuckerman [43], and the overview of the Mathieu equation given in [8].

- Chapter 4 represents a great deal of work by dozens of people, though most of the design and nearly all of the initial setup were my own. Of course, the experimental aparatus could not have been built without the expertise of the mechanical technicians in the physics department. Likewise, all measurements would have been recorded with a pen and paper had it not been for the electronics technicians in the physics department.

- The time-frequency analysis presented in Chapter 5 was mainly taken from [55], but has never been applied to analog cosmology experiments, nor (to my knowledge) has it been applied to parametric resonance in order to extract amplification and damping rates. The field theory concepts in this chapter are mainly adapted from [56] and [57], and the squeezing analysis is an extension of the analysis presented in Chapter 2.

- Chapter 6 reflects Chapter 4, in that it represents the work of a large number of people, though most of the initial work in obtaining these results was done by me. Much of the work presented in this chapter (especially relating to the free field theory) is part of current research, and its interpretation is ongoing.

Chapter 2

Analog cosmology in a strong-gradient magnetic field

The experiment presented in the chapters that follow were initially motivated by the possibility of verifying cosmological predictions in a time-dependent analog spacetime, in line with the experiments conducted in [27], and [58], with the final goal of creating an analog simulator for exponential inflation using a strong-gradient magnetic field [50]. In this chapter, we will present the original work relating to this proposed experiment. While this experiment was never conducted, the numerical results in this chapter served as motivation for the shaker experiments investigated in the rest of this thesis. This chapter will include the first derivation of a time-dependent analog metric for an interface wave system, and constitutes the only proposal capable of simulating inflationary dynamics in a two-fluid system that has been reported to date.

Based off of the work published in [50], we will start with an abridged derivation of the wave equation for the velocity potential in the two fluid system, demonstrating that this potential obeys the same equations of motion as a massless scalar field in an FLRW spacetime (a more detailed treatment of the fluid equations is given in Chapter 3). We will then present some more recent predictions for the height field, motivated by the insights gained in the parametric resonance experiments. These predictions incorporate dissipation for a height field simulation in the proposed magnet experiment.

2.1 Analogue cosmology

We consider a system of two immiscible liquids, a diamagnetic layer lying atop a paramagnetic one, that can be moved at a precisely controllable rate through a strong, spatially varying magnetic field generated by a superconducting solenoid or a Bitter magnet (c.f. Ref. [59, 60]). The body forces applied to the liquid sample amount to an effective gravitational force, whose time dependence can be controlled by the geometry of the magnetic field and the sample's velocity. Thus, the fluids are subject to a time-varying effective gravitational field.

It is well-known [15] that small perturbations on the surface of irrotational fluids experience an effective geometry whose properties are determined by the background flow. The corresponding metric in our system takes the form $g_{\mu\nu} \propto \mathrm{diag}(-c^2, 1, 1)$, where c is the propagation speed of the interface perturbations. A key property of surface waves is that the propagation speed depends on gravity, which in our system is rendered time-dependent.

This provides the versatility to engineer analogue cosmological spacetimes and study in detail the dynamics of perturbations in various time-dependent backgrounds. We discuss our experimental setup, and show that within this system an inflationary regime arises naturally: the effective speed of propagation of surface waves can be tailored to decrease in an exponential fashion giving rise to a shrinking 'effective horizon'. Thus, the interface fluctuations exit the horizon mode by mode, transitioning from uncorrelated oscillatory behavior to frozen and squeezed regimes, in direct analogy to inflationary perturbations.

2.2 The two-fluid system

The derivation here is included in order to clarify the analogy with cosmology. Many steps are skipped, however everything that follows is correct, despite being abridged. For a more detailed derivation, see section 3.1.1.

We consider an immiscible two-fluid system (2.1), with densities $\rho_1 > \rho_2$, heights $h_2 = -h_1 = h_0$, small magnetic susceptibilities $|\chi_{1,2}| \ll 1$, and flow velocities $v_{1,2}$. The system is subjected to a magnetic field $B(\vec{x}, t) \sim 10\,\mathrm{T}$ with a large vertical field gradient $\sim 150\,\mathrm{T/m}$. To model this system, we consider Euler's momentum equation for an invicid and incompressible fluid

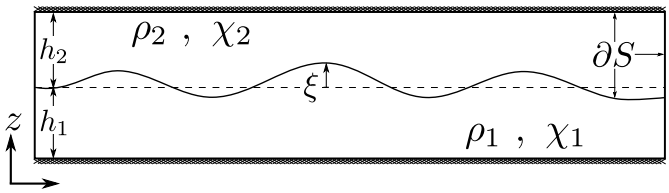

Figure 2.1: Schematics of the two-fluid system. Two immiscible fluids, with densities $\rho_{1,2}$, magnetic susceptibility $\chi_{1,2}$, and height $h_{1,2}$, separated by the equilibrium interface at z_0 (dotted line). Gravity interface waves distort the interface layer (solid line) where each point is characterized by its amplitude ξ and velocity U_θ (U_r). ∂S are the boundaries (here depicted for fluid 2) given by a hard wall (upper), an interface boundary (right), and a moving boundary at the interface of the two fluids (lower).

with the inclusion of the magnetic potential energy [47, 46, 61]:

$$\vec{\nabla} \cdot \vec{U}_j = 0 \tag{2.1}$$

$$\rho_j \left(\partial_t + \vec{U}_j \cdot \vec{\nabla}\right) \vec{U}_j = \vec{\nabla} \left(-p_j + \frac{\chi_j}{2\mu_0} B^2\right) + \rho_j \vec{g} \; . \tag{2.2}$$

In the above, the indices $i = \{1, 2\}$ label the lower and upper fluids respectively; p_j is the fluid pressure, μ_0 the vacuum permeability, and $\vec{g} = (0, 0, -g)$ is the acceleration due to gravity. We assume an irrotational velocity field $\vec{U}_j = \vec{\nabla}\phi_j$, and a fluid-fluid interface ξ given by $z = z_0 + \xi(\theta, r, t)$. We then linearise equations (2.1) and (2.2) around a stationary background flow, so that $\phi_j = \phi_0 + \varphi_j$, with $\phi_0 = 0$. We further take $\partial_z B \gg \partial_r B$. Expanding the B^2 term in a Taylor series about ξ, the linearized Euler equations for each fluid at the interface can be written as

$$\rho_j \partial_t \varphi = -p_j - \left(\rho_j g + \frac{\chi}{\mu_0} B \partial_z B\right) \xi \tag{2.3}$$

At the impermeable upper and lower boundaries h_1 and h_2, equation (2.1) leads to the Ansatz

$$\varphi_j = \sum_k \cosh[k(z - h_j)] \varphi_{j,k}(\theta, r, t), \tag{2.4}$$

where k^2 represents the eigenvalues of the 2D-Laplacian in cylindrical coordinates (in this case the wavenumber squared) and the sum is over all

eigenvalues. The dynamic boundary condition at the interface is obtained by subtracting (2.3) for fluid 2 from fluid 1:

$$\rho_1 \partial_t \varphi_1 - \rho_2 \partial_t \varphi_2 = \left(-(\rho_1 - \rho_2) g_0 + \frac{(\chi_1 - \chi_2)}{\mu_0} B \partial_z B \right) \xi - \Delta p, \tag{2.5}$$

and the change in pressure across the interface is related to the height field by

$$\Delta p = \tau \nabla^2 \xi, \tag{2.6}$$

where τ is the coefficient of the surface tension [10].

The kinematic boundary condition can be written as

$$\partial_t \xi = \partial_z \varphi_1 = \partial_z \varphi_2, \tag{2.7}$$

which, together with the ansatz above evaluated at $z = 0$ leads to

$$k \sinh(-k h_0) \varphi_{2,k} = k \sinh(k h_0) \varphi_{1,k}, \tag{2.8}$$

which implies that

$$\varphi_{2,k} = -\varphi_{1,k}. \tag{2.9}$$

Relabeling $\varphi_k \equiv \varphi_{1,k}$, and substituting equation (2.6) into equation (2.5) in k-space, we get

$$(\rho_1 + \rho_2) \partial_t \varphi_k \cosh(k h_0) = \left(-(\rho_1 - \rho_2) g_0 + \frac{(\chi_1 - \chi_2)}{\mu_0} B \partial_z B + \tau k^2 \right) \xi_k. \tag{2.10}$$

Defining the effective gravity [59],

$$g_{\text{eff}} = g - \frac{[\chi_1 - \chi_2]}{[\rho_1 - \rho_2]\mu_0} B \partial_z B \ , \tag{2.11}$$

and the gravitational term

$$G_k = \frac{([\rho_1 - \rho_2] g_{\text{eff}} + \tau k^2)}{\tilde{\rho}} \, , \tag{2.12}$$

(where $\tilde{\rho} = \rho_1 + \rho_2$), we can rewrite equation 2.10 so that the ξ_k term is isolated:

$$G_k^{-1} (\rho_1 + \rho_2) \dot{\varphi}_k = \xi_k. \tag{2.13}$$

Taking the time derivative of both sides, and noting that $\dot{\xi}_k = k\sinh(kh_0)\varphi_k$ by equation (2.7), we finally arrive at our wave equation for φ_k:

$$\ddot{\varphi}_k + \omega_k^2 \varphi_k = \frac{\dot{g}_{\text{eff}}}{G_k}\dot{\varphi}_k \ , \tag{2.14}$$

where the left hand side of (2.14) describes the familiar oscillatory behaviour with frequency

$$\omega_k^2 = G_k k \tanh(kh) \, . \tag{2.15}$$

The effective gravity, g_{eff} in our setup can be modulated by the motion of the sample (and thus of the interface $z_0(t)$) through the external magnetic field $B(z)$. This introduces an explicit time dependence of the frequency $\omega_k \equiv \omega_k(t)$ as well as an additional friction term (right hand side of (2.14)) corresponding to the Hubble friction well known in cosmology [1]. The acceleration of the sample, $\ddot{z}_0$, is taken into account by substituting $g \to g + \ddot{z}_0$ in (2.11).

2.3 Massless scalar fields in FLRW spacetimes

In order to make the connection with cosmology transparent we consider the shallow water (or long wavelength) limit $kh \ll 1$. The change in the effective gravity (2.11) directly translates to a change in the propagation speed c_k of long wavelength perturbations. We define the mode-dependent scale factor

$$a_k^{-2}(t) \equiv c_k^2(t) = G_k(t)h \ , \tag{2.16}$$

with which the equation of motion (2.14) take the form

$$\ddot{\varphi}_k + 2\frac{\dot{a}_k}{a_k}\dot{\varphi}_k + \frac{k^2}{a_k^2}\varphi_k = 0 \ . \tag{2.17}$$

Thus, our two fluid system in the shallow water limit is equivalent to a massless scalar field in a FLRW-type rainbow universe [33]. In the long wavelength regime, the k-dependence of the scale factor remains due to the surface tension τ (see equation (2.12)). This regulatory part vanishes when $\tau \to 0$, and the effective metric for the perturbations is then:

$$ds^2 = g_{\mu\nu}dx^\mu dx^\nu = -dt^2 + a^2(t)(dx^2 + dy^2) \ . \tag{2.18}$$

This is the exact FLRW solution to the Einstein's equations for an expanding, homogeneous, and isotropic universe described by one k-independent scale factor $a(t)$. In addition, it is possible to change the sign of $G_k(t)$ by inverting the direction of g_{eff} (see Fig. 2.2B), previously exploited in magnetic levitation experiments e.g. [59, 47, 46, 49]. In our setup, this corresponds to a Hartle-Hawking-like [62, 63] change from Lorentzian to Euclidian signature in the analogue spacetime geometry, as can be seen from Eqs. (2.16) and (2.18).

Note that even for $\tau \neq 0$ the ability to change the sign of the effective gravity g_{eff} allows for an infinite expansion for a single mode in our system. This can be explicitly seen by calculating the number of e-folds

$$N = \ln\left(\frac{a_k(t_{\text{f}})}{a_k(t_{\text{i}})}\right) = \frac{1}{2}\ln\left(\frac{\tau k^2 + [\rho] g_{\text{eff}}(t_{\text{i}})}{\tau k^2 + [\rho] g_{\text{eff}}(t_{\text{f}})}\right) , \tag{2.19}$$

used in cosmology to describe the length of the inflationary period, where here the denominator can approach zero if g_{eff} becomes negative. Thus, by changing the magnetic field accordingly, it is possible to engineer the exact time-dependence of the scale factor $a_k(t)$ to correspond to exponential expansion for a specific k-value, or (as in what follows) inflation in the linear dispersion limit:

$$a_k^2(t) = \frac{\tilde{\rho}}{([\rho_1 - \rho_2]\, \mathrm{e}^{-2Ht} + \tau k^2)} \simeq \frac{\tilde{\rho}}{[\rho_1 - \rho_2]}\, \mathrm{e}^{2Ht}, \tag{2.20}$$

where H is the effective Hubble parameter. This includes, in principle, an arbitrarily high number of e-folds for certain values of k.

2.3.1 Effective horizon and mode freezing

One of the hallmarks of inflation, giving rise to the large scale structure formations observed in our universe, is the freezing of modes once they exit the Hubble horizon. It is common to introduce the auxiliary field $\chi_k = a_k\, \varphi_k$ for which the wave equation (2.14) takes the form of a time-dependent harmonic oscillator with frequency

$$\Omega_k^2(t) = \frac{k^2}{a_k^2} - \frac{\ddot{a}_k}{a_k} . \tag{2.21}$$

Horizon crossing occurs at $\Omega_k^2 = 0$, separating the oscillating solution dominated by the first term on the right hand side from exponentially growing / decaying solutions at late times, dominated by the time-independent

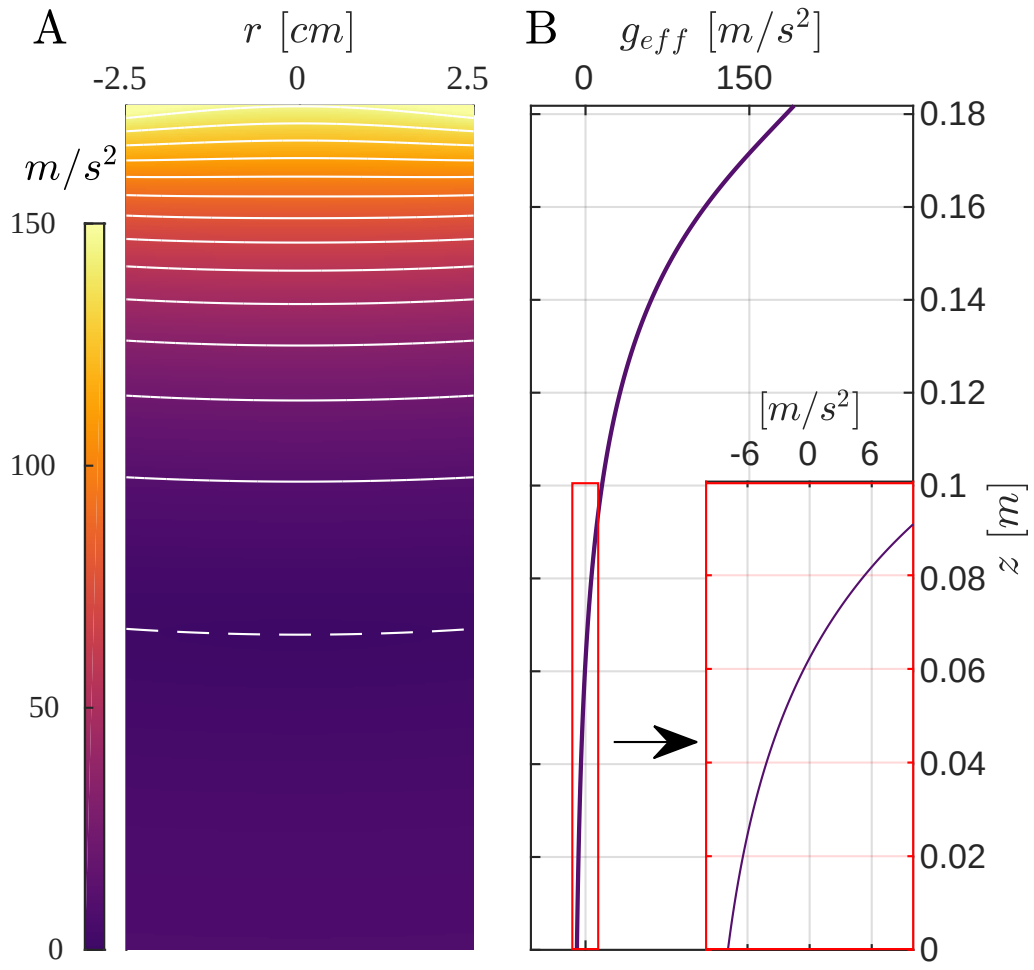

Figure 2.2: Panel A depicts the effective gravity g_{eff} in the bore of the magnet for the butanol-aqueous solution ($\ddot{z}_0 = 0$). The vertical axis gives the vertical position in the magnet z, and the horizontal axis the radial position r. The magnitude is given by the colorbar. The solid white lines are contours of the effective gravity, with the dashed line depicting the region over which g_{eff} changes sign. Panel B is the effective gravity along the axis of the solenoid ($r = 0$). The inset rescales the horizontal axis to better demonstrate the sign change of g_{eff}.

second term. The essence of inflationary dynamics is fully captured for late times after a mode has crossed the horizon, since the dynamics of the physical field φ_k freezes and becomes trivial, obeying a constant solution in time.

Our system exhibits an analogue behaviour, where each mode crosses the shrinking effective horizon beyond which it freezes. In Figure 2.2 panel B the solution of the field equation (2.14) for the longest wavelength of our system is shown for the full non-linear dispersion relation (2.15), computed numerically using a Runge-Kutta fourth-order scheme. For $t < 0$ the system is evolved in flat space, reducing (2.14) to a simple harmonic oscillator. At $t = 0$ the system begins to expand, leading to an oscillatory, damped time evolution of the field, which upon crossing the effective horizon approaches rapidly a nearly constant field solution.

The non-dissipative model (including dispersive effects) exhibits minor differences to a completely frozen field solution, caused by the interfacial tension. For the expansion parameter outlined in equation (2.20), the surface tension introduces a small time-depence to $\ddot{a}_k/a_k$ and in turn a slow further evolution of the field outside the horizon. Apart from a different effective expansion experienced by high momentum modes, this regulatory part leads to the mode re-entering the Hubble horizon, exhibiting oscillatory behaviour at later times. [1]

Returning to figure 2.3 (panel B), we further present the evolution of the surface height $\xi_k = a_k^2\dot{\varphi}_k$, directly accessible in the experiment, which exhibits a growing, non-oscillatory solution after horizon crossing. The continuous observation of the field dynamics provides direct evidence for the inflationary dynamics of the system.

2.3.2 Classical squeezing for inflation model

While the above evolution and mode freezing describe the full dynamics during inflation, there is an equivalent description in terms of squeezed states [64, 65]. This approach is in close analogy to condensed matter systems undergoing rapid changes (e.g. quenches [38]) in the propagation speed of long-wavelength perturbations.

For a quadratic field theory the quantum nature of the system is only determined by the initial conditions, while each trajectory evolves according

[1] When dissipation is included in the wave equation from the onset, this behavior is not present. See equation (2.34) and the discussion thereof below.

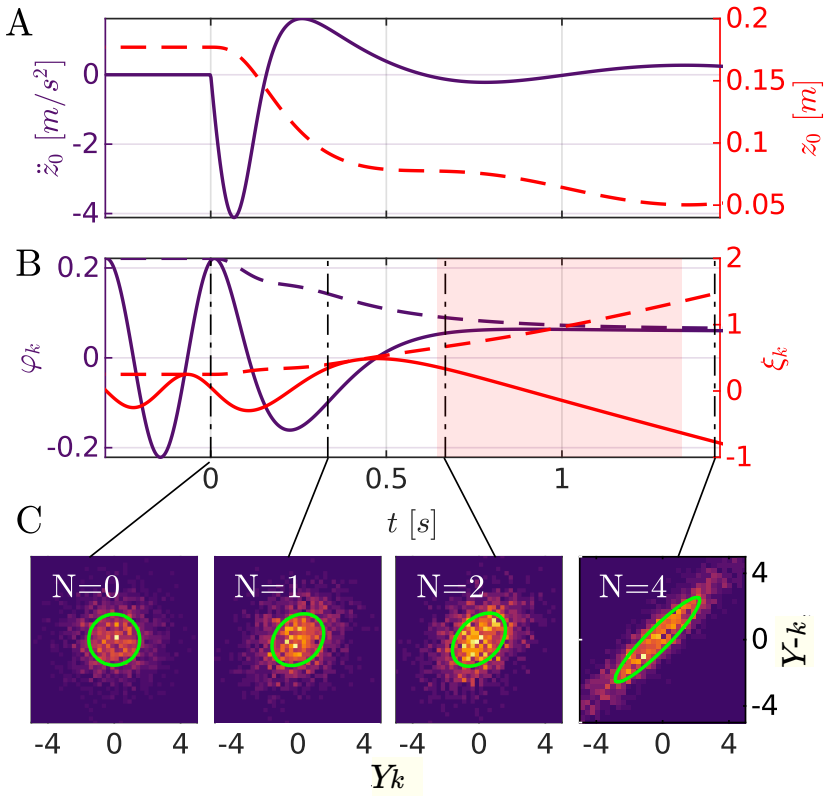

Figure 2.3: Panel A shows the evolution of the vertical position $z_0(t)$ (dashed red) and acceleration $\ddot{z}_0(t)$ (solid purple) of the vessel in the magnet corresponding to an exponentially inflating analogue universe with Hubble parameter $H = 3\,s^{-1}$.
Panel B depicts the solution to the wave equation (2.17). The solid lines represent the real part, and the dashed lines represent the absolute value of the velocity potential ϕ_k (purple) and of the height field ξ_k (red). The black dash-dotted lines represent different number of e-folds $N = 0, 1, 2$ and 4 for the mode. The shaded region indicates where the mode is outside the Hubble horizon.
Panel C depicts the maximal two-mode squeezing of the system projected onto the instantaneous eigenbasis at the times (equivalently number of e-folds) indicated. The solid line indicates the theoretical full width at half maximum for each distribution. The intensity plots represent the probability of a given measurement of Y_k and Y_{-k} after 2000 simulated experimental runs.

to the classical equation of motion [66]. Therefore, by emulating the quantum statistics of the initial state, we can study the full time evolution of inflationary physics within the linear regime of fluid dynamics.

Our system allows us to stop the expansion and to analyse the inflationary signatures in the resulting flat spacetime through the statistical properties of the state. The associated definition of a well defined ground (vacuum) state leads to cosmological quasi-particle production (mode amplification) and two-mode squeezed states. This is the result of the rapid effective expansion of our analogue universe connecting two flat regions of spacetime $a(t_\mathrm{i}) \to a(t_\mathrm{f})$ [57]. Note that while the freezing of the modes is sensitive to $\ddot{a}_k/a_k \approx$ const, squeezing effects are rather generic and occur for more general types of expansion. [2] In line with quantum field theory in curved spacetime, we introduce the classical quasi-particle amplitudes b_k in the initial flat region of spacetime by expanding the field

$$X_k(x,t) = \left(f_k^\mathrm{i}(t) b_k + f_k^\mathrm{i}(t)^* b_{-k}^*\right) \exp(\mathrm{i}kx), \tag{2.22}$$

where the $b_{\pm k}$ are complex constants representing the initial state, and the $f_k(t)$ represent the field evolution in time. The time-dependent mode functions (f_k, f_k^*), normalized by the Wronskian:

$$\langle f_k\,;\, f_k\rangle \equiv \mathrm{i}\,(f_k^* \partial_t f_k - (\partial_t f_k^*) f_k) = 1.$$

As the conservation of the Wronskian implies $|\alpha_k|^2 - |\beta_k|^2 = 1$, the initial and final flat regions of spacetime are related by a Bogoliubov transformation $f_k^\mathrm{i}(t) = \alpha_k f_k^\mathrm{f}(t) + \beta_k f_{-k}^\mathrm{f}(t)^*$. The final state is fully described by the corresponding transformation of the quasi-particle amplitudes

$$d_k \equiv \langle f_k^\mathrm{f}(t)\,;\, X_k\rangle = \alpha_k b_k + \beta_k^* b_{-k}^*. \tag{2.23}$$

The measurable mode intensity after the effective expansion in our system is

$$\langle d_k^* d_k\rangle = \left(2|\beta_k|^2 + 1\right) \langle b_k^* b_k\rangle\ , \tag{2.24}$$

[2] In light of the work done on the shaker experiment, it is not clear whether the d_k and d_{-k} amplitudes can be observed separately, since the concept of positive and negative frequency modes (or equivalently, propagating and counter-propagating) is nullified when $\omega_k \to 0$ (see equations (2.22) and (2.23)). The interpretation of the squeezing results presented in the original publication is ongoing, however the following is presented here in order to provide context for the predictions in figure 2.3. For a more detailed treatment, see Chapter 5, sections 5.2, 5.3.1, and 5.3.2.

where $\langle \dots \rangle$ denotes the classical expectation value over sufficiently many measurements, allowing us to assume $\langle b^*_{-k} b_{-k} \rangle = \langle b^*_k b_k \rangle$.

As anticipated from translational invariance in equation (2.17), the Bogoliubov coefficients α_k, β_k only mix modes of opposite momenta:

$$\langle d_{-k} d_k \rangle = 2\alpha_k \beta^*_k \langle b^*_k b_k \rangle \ . \tag{2.25}$$

Quasi-particle amplification therefore occurs in the form of correlated, counter-propagating pairs, and our system exhibits the classical analogue of two-mode squeezing. Therein the fluctuations in one quadrature are lowered below their initial value at the cost of increasing the fluctuations in the other. Defining the position variable

$$Y_k = \left(f^{\mathrm{f}}_k(t) d_k + f^{\mathrm{f}}_k(t)^* d^*_k \right) / |f^{\mathrm{f}}_k|, \tag{2.26}$$

we show in figure 2.3, panel C, the two-mode squeezed states for varying number of e-folds N during the expansion.

For each parameter we sampled 2000 trajectories from an initial uncorrelated Gaussian state. At the times presented, the maximum squeezing $|\alpha_k - \beta_k|^2$ caused by the correlations (2.25) increases with N, due to the increasing number of created quasi-particle pairs. A similar behaviour is found by increasing the effective Hubble parameter H, as shown in Fig. 2.3 for $H = 2,4\ s^{-1}$ and the limit of an instantaneous quench, $H \to \infty$. Note that each mode itself shows no sign of squeezing and is simply amplified according to (2.24).

2.4 Proposed experimental implementation

In order to minimise the influence of non-linear contributions to the dispersion relation, we choose a two-fluid system consisting of 1-butanol and a weak aqueous paramagnetic solution, with a small interfacial surface tension, $\tau = 1.8\mathrm{mN/m}$ [67] (immiscibility requires $\tau \neq 0$). We take an annular basin for which the azimuthal degrees of freedom obey periodic boundary conditions with a maximal wavelength $\lambda_{\max} = \pi d$. The diameter d is limited by the size of the bore of the superconducting magnet, which for our experimental setup is $d = 4\mathrm{cm}$.

A significant advantage of our proposed system is the ability to make non-destructive measurements of interface-waves. For example, using a "Fast

Checkerboard Demodulation" (FCD) method [68] enables the time-resolved measurement of the full dynamics. Another benefit to the proposal stems from our ability to repeat a single experiment under the same laboratory conditions, enabling us to test the statistical predictions of cosmology in a way that was never before possible.

We tune the scale factor $a(t)$ to be exponential in the linear dispersion limit. This can be achieved by combining the spatially dependent magnetic forces within the bore with a small mechanical acceleration of the system. The time-dependent position and acceleration of the basin in the magnet is given in 2.3 panel A, determined by solving the differential equation

$$g_{\text{eff}}(z_0, \ddot{z}_0) = g_0 \exp(-2Ht), \tag{2.27}$$

where g_{eff} is a function of z_0 and $\ddot{z}_0$, and g_0 is the initial effective gravitational acceleration. In Figure 2.2, we show the effective gravity in the magnet bore for our butanol-aqueous system. Panel A depicts the effective gravitational acceleration for a cross-section of the magnet bore, and panel B provides a plot of g_{eff} as a function of the vertical position.

2.5 Predictions for the height field including dissipation

The previous sections describe the theoretical motivation for a proposed experiment. At the time of the original proposal, little was known regarding how the small scale of the experiment would affect our findings. In Chapter 3, we will provide a more detailed derivation of the equations of motion, and provide some discussion on the importance of dissipation and boundary layers for small systems. In this section, we will present some newer results, simulating the height field (which is directly observable) for the same system in the same magnet, this time including an additional damping term with coefficient γ_k and a stochastic source (see equation (6.21), section 6.2.1 for more details). The damping rate is calculated using the theory of [45], modified to accomodate an annulus instead of a cylinder.

If we use equation (2.7) to note that

$$\varphi_k = \frac{1}{k \sinh(kh_0)} \dot{\xi}_k, \tag{2.28}$$

we can eliminate φ_k from equation (2.13) to obtain

$$\ddot{\xi}_k + \omega_k^2 \xi_k = 0. \tag{2.29}$$

Adding a phenomenological damping term, and a stochastic source term, we have,

$$\ddot{\xi}_k + 2\gamma_k \dot{\xi}_k + \omega_k^2 \xi_k = \Gamma_k(t). \tag{2.30}$$

Figure 2.4 depicts the results for a set of eigenmodes. Each curve represents the mean result of 1000 simulations, and the trajectory through the magnet is chosen so that $a_k(t) = \mathrm{e}^{Ht}$ (with $H = 5$), for the selected $m = 1$, $k = 68\mathrm{m}^{-1}$ mode (chosen because it has the smallest value of γ_k). As can be seen, the chosen mode is sharply amplified when the expansion begins, however instead of increasing linearly as seen for the ξ_k field in figure 2.3 (panel B), it seems to increase monotonically with decreasing velocity.

To see why this is, we examing the damped equation of motion, in the limit $\omega_k \to 0$:

$$\ddot{\xi}_k = -2\gamma_k \dot{\xi}_k \tag{2.31}$$

$$\implies \dot{\xi}_k(t) = \dot{\xi}_k(t_0)\, \mathrm{e}^{-2\gamma_k (t - t_0)} \tag{2.32}$$

$$\implies \xi_k(t) = \xi_k(t_0) + \frac{\dot{\xi}_k(t_0)}{2\gamma_k} \left(1 - \mathrm{e}^{-2\gamma_k (t - t_0)}\right) \tag{2.33}$$

Thus, we can see that the inclusion of damping stabilizes the system (minimizing the chance of nonlinearities), and the modes should approach a constant amplitude so long as a stable g_{eff} can be maintained.

In terms of mode freezing, these results require some extra interpretation. In equation (2.21), we see that mode freezing is due to the Hubble friction term in equation (2.17), and occurs for φ_k when the scale factor a_k outgrows the wavenumber k.

As it happens, the equations leading up to the wave equation (2.30) do not lead to a Hubble friction term in the ξ_k field, and the only parameter which is capable of 'freezing' the height field is the damping term γ_k. We know from the familiar example of the damped harmonic oscillator [69] that the ξ_k field oscillates with natural frequency

$$\tilde{\omega}_k = \sqrt{\omega_k^2 - \gamma_k^2}, \tag{2.34}$$

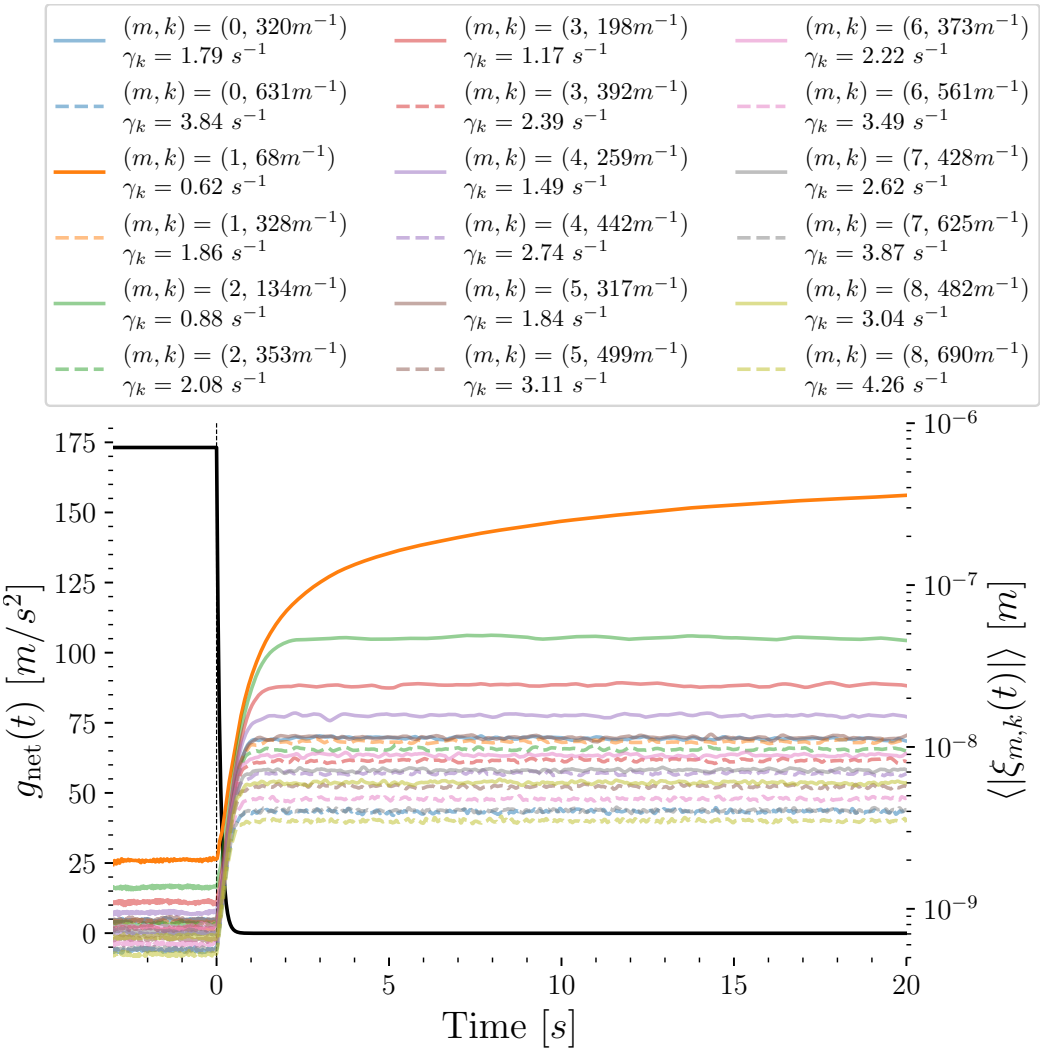

Figure 2.4: Simulated damped ξ_k evolution in the superconducting magnet. The fluid parameters are the same as in figure 2.3, however dissipation and a stochastic source are included as in equation (2.30).
The left-hand axis shows the effective gravitational acceleration in black. The right-hand axis depicts the mean evolution of each of the mode functions, and the corresponding values of (m, k) and γ_k are listed in the legend at the top.

and it is clear that the modes will become 'frozen' once $\omega_k \leq \gamma_k$.

Figure 2.5 shows the natural frequency of each of the simulated modes with respect to time. Because the effective gravity in these simulations prefers the $m = 1$, $k = 68\text{m}^{-1}$ dispersion relation, this is the only mode which undergoes freezing as described above. The inset of the plot shows the real and imaginary parts of the natural frequency for the chosen mode with respect to time. As can be seen, for the chosen mode freezing happens at roughly $t = 0.8\text{s}$, corresponding to 4 e-folds of analog inflation. Comparing mode freezing in a system without damping to these results will be a future line of investigation.

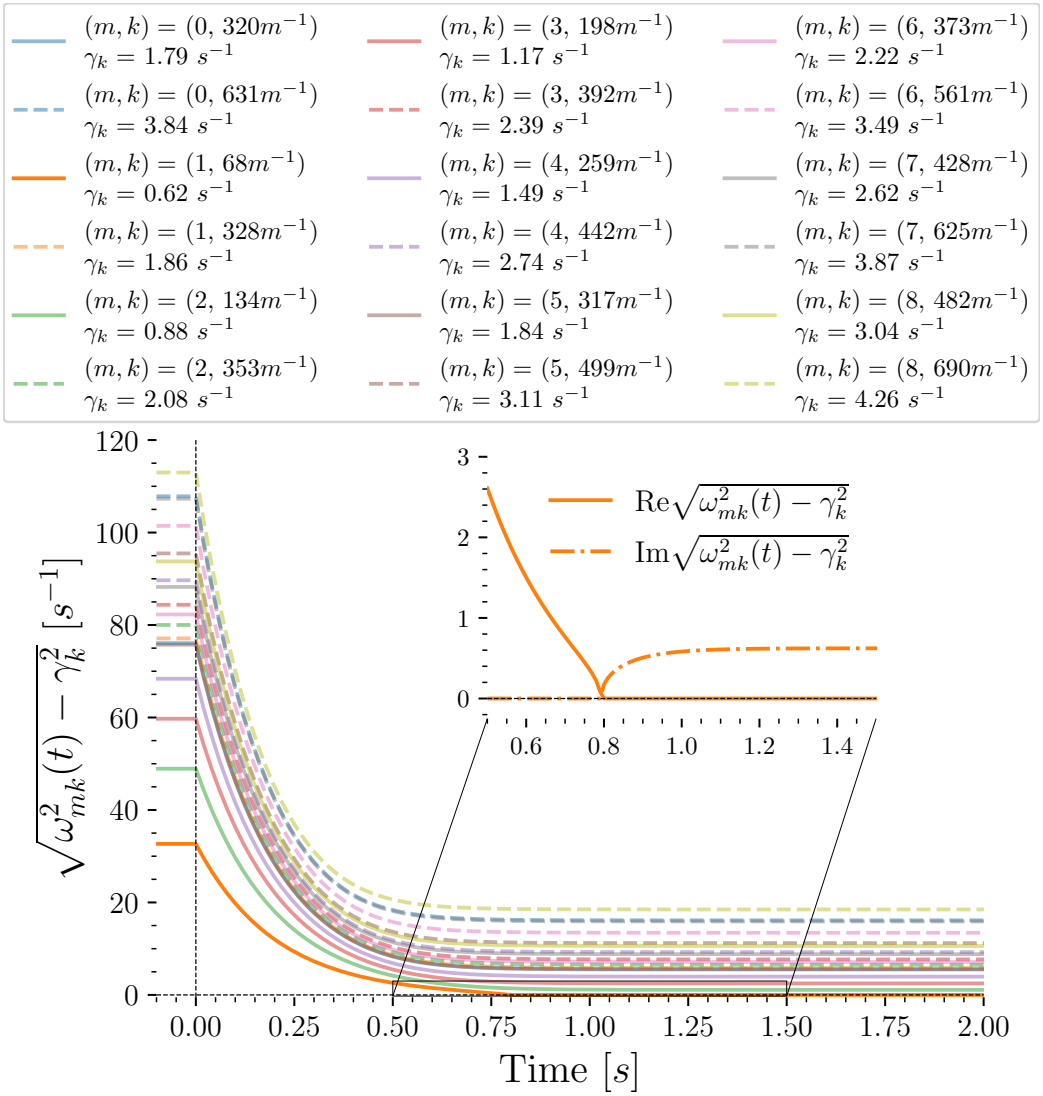

Figure 2.5: Simulated natural frequency for each of the eigenmodes in the superconducting magnet. The chosen mode function 'freezes' at $t = 0.8$s, corresponding to 4 e-folds of analog inflation. The inset demonstrates that after the mode freezes, the mode evolves exponentially. This is in line with the predictions of equation (2.33).

Chapter 3

Fluid theory and parametric amplification

The modelling of interface waves has varying degrees of complexity, and when the system size is large compared to the capillary length it is possible to start from the simple case of an invicid, irrotational fluid as presented in the previous chapter. At smaller scales, rotational boundary layer effects due to viscosity are believed to become important [44, 43], and these effects are taken into account at the solid walls of the fluid container as well as at the interface.

The motion of a fluid is governed by the continuity equation, and the Navier Stokes equations. The continuity equation represents the conservation of mass in the fluid system. For incompressible fluids, the continuity equation can be written as

$$\nabla \vec{U} = \nabla \vec{u} + \nabla^2 \phi = 0, \tag{3.1}$$

where $\vec{U}$ is the fluid's velocity field, and $\vec{u}$ and ϕ are the solenoidal and irrotational components respectively. For incompressible fluids with constant density *and viscosity*, the Navier Stokes equations can be written as

$$\partial_t \vec{U} + \left(\vec{U} \cdot \nabla\right) \vec{U} - \frac{\mu}{\rho} \nabla^2 \vec{U} = -\frac{1}{\rho} \nabla p + \vec{g}, \tag{3.2}$$

where μ is the dynamic viscosity of the fluid, ρ is the fluid density, $\vec{g}$ is an external acceleration (often the acceleration due to gravity) [10, 70, 71, 44]. The pressure p is defined by the stress tensor σ [10]:

$$\sigma_{ab} = -p\delta_{ab} + \mu \left(\frac{\partial u_a}{\partial x_b} + \frac{\partial u_b}{\partial x_a} \right), \tag{3.3}$$

where the indices $a, b \in \{\theta, r, z\}$ indicate the spacial dimension.

The Navier Stokes equation represents the conservation of momentum in a fluid and are famously difficult to solve, even numerically [72]. Because of this, certain assumptions and approximations are often necessary when attempting to find tractable equations of motion for a system. These assumptions often come in the form of linear approximations, subject to rule-of-thumb conditions, such as the small amplitude condition for interface waves [10]:

$$a \ll L, \tag{3.4}$$

where a is the amplitude of the interface wave, and L is the wavelength.

In the following sections, we will first derive the wave equation which most closely corresponds to the time-dependent gravitational analogy. A theoretical treatment of interface waves undergoing parametric resonance will then be given for the simple dispersion relation derived previously. This theory will then be expanded to include a more comprehensive treatment of the boundary layers in the system. Finally, some practical considerations regarding a full theoretical description of the system will be listed, as well as a simplified, phenomenological model.

3.1 Simple dispersion relation

Figure 3.1 depicts the fluid system under consideration. We have an annular volume of fluid, bounded at inner and outer radii r_1 and r_2 respectively by ridged, concentric (right circular) cylindars. The upper and lower boundaries consist of parallel ridged plates, located at h_1 and h_2 respecively.

In the following section, we will derive the equation of motion for the perturbed height field for eigenmodes in the system. The vertical position of the interface is defined at $z = z_0 + \xi$ (and in what follows we choose our coordinate system such that $z_0 = 0$). We will refer to the lower and upper fluids using the index $j = \{1, 2\}$ respectively, and we assume that the flow in the system is everywhere irrotational, so that $\vec{u} = 0$, and the velocity field is fully described by a velocity potential, ϕ_j:

$$\vec{U}^{(j)} = \vec{\nabla}\phi_j. \tag{3.5}$$

We further assume that the system is perturbed from rest, and we neglect any terms of order $\mathcal{O}(\phi_j^n)$, and $\mathcal{O}(\xi^n)$ for $n > 1$.

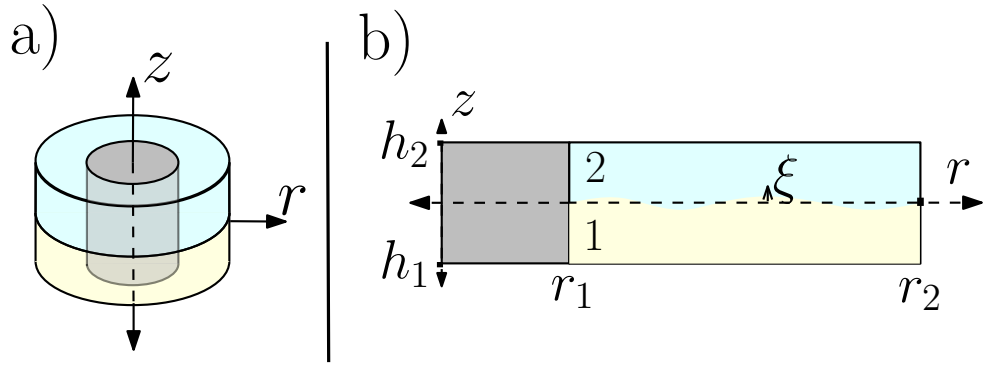

Figure 3.1: The left-hand panel, a) depicts a schematic of the two-fluid system. In panel b), we see an azimuthal slice of the vessel. The denser fluid, labeled 1 sits below the lighter fluid, labeled 2. The coordinate axes are chosen such that the equillibrium height is at $z = 0$, and the vertical boundary walls are axisymmetric.

3.1.1 Laplace's Equation

From the continuity equation, we have

$$\vec{\nabla} \cdot \vec{U}^{(j)} = \nabla^2 \phi_j = 0. \tag{3.6}$$

From this, we can see that the equation of motion for the fluid height is the result of the boundary conditions to Laplace's equation, the solutions for which are quite well known. Defining $\nabla^2 = \nabla_x^2 + \partial_z^2$, we have that

$$\nabla_x^2 \phi_j = -k^2 \phi_j, \tag{3.7}$$

where ϕ_j is given by

$$\phi_j = \sum_m \sum_k \mathrm{e}^{im\theta} \left(a_r H_m^{(1)}(kr) + b_r H_m^{(2)}(kr) \right) f_j(z) \varphi_{j,k}(t). \tag{3.8}$$

In the above, $H_m^{(1)}$ and $H_m^{(2)}$ are Hankel functions of order m of the first and second kind respectively. $f(z)$, and $\varphi_k(t)$ are as-yet-unknown functions, and k is found by assuming that the fluid does not penetrate the ridged boundaries at $r = r_i$, which implies that

$$u_r\big|_{r=r_i} = \partial_r \phi\big|_{r=r_i} = 0 \tag{3.9}$$

$$\implies a_r k H_m^{(1)\,\prime}(kr_i) + b_r k H_m^{(2)\,\prime}(kr_i) = 0. \tag{3.10}$$

The two equations at r_1 and r_2 are used to determine the two unknowns a_r and b_r. It is easy to show that if we do not want to have $a_r = b_r = 0$, then we must have

$$H_m^{(1)\,\prime}(kr_2)H_m^{(2)\,\prime}(kr_1) - H_m^{(1)\,\prime}(kr_1)H_m^{(2)\,\prime}(kr_2) = 0, \tag{3.11}$$

which must be solved for k numerically.

Using the expansion (3.8), equation (3.7) and equation (3.6) together imply that

$$\partial_z^2\phi - k^2\phi = 0 \tag{3.12}$$

$$\implies f''(z) = k^2 f(z). \tag{3.13}$$

With a bit of foresight, we can write the general solution to this equation as

$$f_j(z) = a_j \sinh(k[z - h_j]) + b_j \cosh(k[z - h_j]), \tag{3.14}$$

where h_j has already been defined as the location of the ridged z-boundaries. Since we have impenetrability at the top and bottom boundaries as well, we have

$$u_z^{(j)}\big|_{z=h_j} = \partial_z\phi_j\big|_{z=h_j} = 0, \tag{3.15}$$

which immediately implies that $a_j = 0$ for $j = \{1, 2\}$. Absorbing the b_j into the $\varphi_{j,k}$ terms, and setting the radial function equal to $R_k(r)$, we have

$$\phi_j = \sum_m \sum_k \mathrm{e}^{im\theta} R_k(r) \cosh(k[z - h_j])\varphi_{j,k}(t). \tag{3.16}$$

3.1.2 The Boundary Conditions at the Interface

The above equation does not describe the time-dependent behavior of the interface waves, as we still do not know the form of the $\varphi_{j,k}$. In order to obtain this description, we need to examine the boundary at the free-surface ξ. The kinematic boundary condition at the surface is given by

$$\partial_t \xi = \lim_{z \to 0^{\pm}} u_z, \tag{3.17}$$

where the limit is from below for fluid 1, and from above for fluid 2. This allows us to expand ξ in terms of the eigenfunctions in equation (3.16),

$$\xi = \sum_m \sum_k \mathrm{e}^{im\theta} R_k(r)\xi_k(t). \tag{3.18}$$

Equation (3.16), together with equations (3.17) and (3.5), imply that

$$\dot{\xi}_k = k \tanh(kh_j) \cosh(kh_j) \varphi_{j,k}, \tag{3.19}$$

which in turn implies (via continuity of the velocity field across the interface) that

$$\varphi_{2,k} = \frac{\sinh(kh_1)}{\sinh(kh_2)} \varphi_{1,k}. \tag{3.20}$$

Throughout the fluid, the velocity field obeys the Euler momentum equation for a fluid at rest:

$$\rho_j \partial_t \vec{U}^{(j)} - \frac{\mu_j}{\rho_j} \nabla^2 \vec{U}^{(j)} = -\vec{\nabla} p_j - \rho_j g \hat{z}. \tag{3.21}$$

The continuity equation implies that the viscous term is zero for irrotational flow in the fluid bulk. Further, since $\vec{U}^{(j)} = \vec{\nabla}\phi_j$ we can simplify the momentum equation by factoring out the gradient:

$$\rho_j \partial_t \phi_j = p_j - \rho_j g z. \tag{3.22}$$

Equation (3.22) is valid throughout each of the fluids, but of particular interest is the boundary between the two. At $z = \xi$, we subtract the $j = 2$ equation from the $j = 1$ to get the dynamic boundary condition at the free surface:

$$\rho_1 \partial_t \phi_1 - \rho_2 \partial_t \phi_2 = \Delta p - (\rho_1 - \rho_2) g \xi, \tag{3.23}$$

where Δ signifies the difference between the fluid 1 component and the fluid 2 component.

It is well-known that the curvature of the interface between two immiscible fluids produces a discontinuity in the stress-tensor [70, 10, 71] and pressure terms. Rearranging the zz component of the stress tensor in equation (3.3) and subtracting fluid 2 from fluid 1, we find that

$$\Delta p = -\Delta \sigma_{zz} - 2 \frac{\partial^2}{\partial z^2} \left(\mu_1 \phi_1 - \mu_2 \phi_2 \right). \tag{3.24}$$

The change in the normal component of the stress tensors, $\Delta\sigma_{zz}$ is related to the curvature via the surface tension coefficient τ,

$$\Delta \sigma_{zz} = \tau \left(\frac{1}{R_1} + \frac{1}{R_2} \right) \simeq -\tau \nabla_x^2 \xi, \tag{3.25}$$

where the R_i represent the orthogonal radii of curvature at the point of interest [71, 10].

Inserting equation (3.25) into equation (3.24), we can eliminate the pressure term from the dynamic boundary equation to get

$$\rho_1 \partial_t \phi_1 - \rho_2 \partial_t \phi_2 = -2\frac{\partial^2}{\partial z^2}\left(\mu_1 \phi_1 - \mu_2 \phi_2\right) - (\rho_1 - \rho_2) g\xi + \nabla^2 \tau. \tag{3.26}$$

In order to eliminate one of the velocity potentials, we use equation (3.16) to note that $\partial_z^2 \cosh(kh_j)\varphi_{j,k} = k^2 \cosh(kh_j)\varphi_{j,k}$, together with equation (3.20) and the map $\nabla_x^2 \xi \mapsto -k^2 \xi_k$ to get:

$$\begin{aligned}
&\left(\rho_1 \cosh(kh_1) - \rho_2 \cosh(kh_2)\frac{\sinh(kh_1)}{\sinh(kh_2)}\right)\partial_t \varphi_{1,k} = \\
&-\left([\rho_1 - \rho_2]g + \tau k^2\right)\xi_k - 2\left(\mu_1 \cosh(kh_1) - \mu_2 \cosh(kh_2)\frac{\sinh(kh_1)}{\sinh(kh_2)}\right)k^2 \varphi_{1,k}.
\end{aligned} \tag{3.27}$$

Dividing both sides of the equation by $\cosh(kh_1)$, and using (3.19) to eliminate the velocity potential term, we have

$$\tilde{\rho}\partial_t \dot{\xi}_k = -\left([\rho_1 - \rho_2]\, g + \tau k^2\right) k \tanh(kh_1)\xi_k - 2k^2 \tilde{\mu}\dot{\xi}_k, \tag{3.28}$$

where we have defined the weighted sums, $\tilde{\rho}$, and $\tilde{\mu}$ by

$$\tilde{\rho} = \rho_1 - \frac{\tanh(kh_1)}{\tanh(kh_2)}\rho_2,$$

and equivalently for $\tilde{\mu}$. Rearranging, we now have a simple wave equation in terms of the interface eigenmode ξ_k:

$$\ddot{\xi}_k + 2\gamma_k \dot{\xi}_k + \omega_k^2 \xi_k = 0, \tag{3.29}$$

where we have defined the exponential damping coefficient [1]

$$\gamma_k = \frac{\tilde{\mu}}{\tilde{\rho}}k^2, \tag{3.30}$$

[1]It should be noted here that this damping term is exactly half the damping term derived in [10], where the total change in energy in the volume of fluid is considered. Attempts to reconsile the results above with the energy derivation have not been successful, however including a generic damping term γ_k from the start seems necessary, as this term changes the equation of motion for the velocity potential field φ_k below.

as well as the natural frequency

$$\omega_k^2 = \left(\frac{\rho_1 - \rho_2}{\tilde{\rho}} g + \frac{\tau}{\tilde{\rho}} k^2 \right) k \tanh(kh_1) \tag{3.31}$$

$$\equiv G_k k \tanh(kh_1). \tag{3.32}$$

3.1.3 The Wave Equation in terms of φ_k

In the previous derivation, no assumptions were made on the gravitional acceleration, g. If we would like to obtain a wave equation in terms of the velocity potential $\varphi_k \equiv \varphi_{1,k}$, we require a bit more care if we want $g \equiv g(t)$ to be a function of time.

We begin by once again dividing both sides of equation (3.27) by $\cosh(kh_1)$:

$$\tilde{\rho}\partial_t \varphi_k = -\frac{1}{\cosh(kh_1)} \left([\rho_1 - \rho_2]g + \tau k^2 \right) \xi_k - 2\tilde{\mu}k^2 \varphi_k. \tag{3.33}$$

From here, we divide each side by $\tilde{\rho}$; isolating the ξ_k term on one side of the equation, we have

$$\partial_t \varphi_k + 2\gamma_k \varphi_k = -\frac{1}{\cosh(kh_1)} G_k \xi_k. \tag{3.34}$$

We require the equation to contain $\partial_t \xi_k$ on its own, so that we may use equation (3.19) to eliminate ξ_k. The usual practice is to operate on both sides with ∂_t, however the time-dependent G_k term prevents this from working directly. Instead, we first divide both sides by G_k,

$$\partial_t \left[G_k^{-1} \left(\partial_t \varphi_k + 2\gamma_k \varphi_k \right) \right] = -\frac{1}{\cosh(kh_1)} \partial_t \xi_k. \tag{3.35}$$

Substituting in equation (3.19), and multiplying both sides by G_k, we are left with [2]

$$\partial_t^2 \varphi_k + \left(2\gamma_k - \frac{\dot{G}_k}{G_k} \right) \partial_t \varphi_k + \left(\omega_k^2 - 2\gamma_k \frac{\dot{G}_k}{G_k} \right) \varphi_k = 0. \tag{3.36}$$

Finally, in the inviscid limit, we have that $\gamma_k \mapsto 0$ and we return to the familiar analog in equation (2.14),

$$\partial_t^2 \varphi_k - \frac{\dot{G}_k}{G_k} \partial_t \varphi_k + \omega_k^2 \varphi_k = 0. \tag{3.37}$$

[2] It should be noted here that the derivation given in Chapter 2 assumes from the start that the fluids considered are invicid. Because of this, the $2\gamma_k \frac{\dot{G}_k}{G_k} \varphi_k$ term is not included.

3.2 Floquet theory for simple dispersion relation

We are interested in the dynamic behavior of linear waves undergoing parametric amplification. The first systematic theoretical description of parametric amplification for (invicid) interface waves was given by Benjamin and Ursell [52], in which equation (3.29) is derived [3] in an oscillating gravitational field, namely,

$$\ddot{\xi}_k + 2\gamma_k\dot{\xi}_k + \left(\frac{\rho_1-\rho_2}{\tilde{\rho}}\left[g+\tilde{\epsilon}\cos(2\omega_d t)\right] + \frac{\tau}{\tilde{\rho}}k^2\right)k\tanh(kh_1) = 0. \quad (3.38)$$

This is a damped Mathieu equation, which is well-known to have stable and unstable solutions depending on the relative values of γ_k, ω_k, ω_d and $\tilde{\epsilon}$. When the interface is unstable, the linear equation above predicts exponential solutions $\mathrm{e}^{(\eta_1-\gamma_k)t}$ and $\mathrm{e}^{(\eta_2-\gamma_k)t}$, and it can be demonstrated that $\mathrm{e}^{\eta_1 t}\,\mathrm{e}^{\eta_2 t} = 1$ [73, 74].

Thus, unstable solutions come in pairs, with $\eta_2 = -\eta_1$. These modes correspond to exponentially growing and decaying oscillations [8, 43, 53], with amplitudes which will be most conveniently described by

$$A_k = \mathrm{e}^{-\gamma_k t}\cosh(\eta_k t), \quad (3.39)$$

$$B_k = \mathrm{e}^{-\gamma_k t}\sinh(\eta_k t). \quad (3.40)$$

Due to the fact that the interface waves cannot actually grow without bound in a real system, the exponential growth predicted by the linear equation of motion for the interface waves breaks the linearity assumption (for example, equation (3.4)) used on the Navier Stokes equation (3.2). Once this threshold amplitude is reached, the system is observed to stabalize in a pattern of constant-amplitude standing waves [51, 75, 76].

In most experimental and theoretical investigations of parametric resonance of interface waves, the exponentially decaying terms are neglected and research tends to focus on so-called stability curves. These are the boundaries between stable and unstable regions of the parameter space defined by $\tilde{\epsilon}$ and ω_k for fixed ω_d and γ_k.

[3] It should be noted that Benjamin and Ursell's invicid derivation left out the damping term completley. This is equivalent to setting $\gamma_k = 0$ in what follows.

To this author's knowledge, no theoretical or experimental investigations have been made regarding the exponential amplification rate, hereafter referred to as $\lambda_k = (\eta_k - \gamma_k)$, described by this linear theory. Instead, the literature tends to focus on stable versus unstable solutions, without regard for the amplification rate.

In order to apply the Floquet analysis to equation (3.38) we will make some definitions:

$$\delta_k = \left(\frac{\tau}{\tilde{\rho}} k^2 + \frac{\rho_1 - \rho_2}{\tilde{\rho}} g \right) k \tanh(k h_0), \tag{3.41}$$

and

$$\epsilon_k = \left(\frac{\rho_1 - \rho_2}{\tilde{\rho}} \tilde{\epsilon} \cos(\omega_d t) \right) k \tanh(k h_0). \tag{3.42}$$

we can re-write equation (3.38) as

$$\ddot{\xi} + 2\gamma_k \dot{\xi} + \delta_k \xi + \tfrac{1}{2}\epsilon_k \left(\mathrm{e}^{i\omega_d t} + \mathrm{e}^{-i\omega_d t} \right) \xi = 0. \tag{3.43}$$

The periodicity of acceleration implies that the solutions are also periodic. We write the general solution as [8, 43]

$$\xi = \mathrm{e}^{(\lambda_k + i\vartheta_k)t} \sum a_n \, \mathrm{e}^{in\omega_d t}, \tag{3.44}$$

where $(\lambda_k + i\vartheta_k)$ is the Floquet exponent for the system, and the sum is over all $n \in \mathbb{Z}$.

It can be demonstrated that when an instability is present, we will have either $\vartheta_k = \frac{1}{2}\omega_d$, or $\vartheta_k = 0$. These cases are referred to as the subharmonic (with frequency $\frac{\omega_d}{2}$) and harmonic (with frequency ω_d) cases respectively [77, 43]. [4]

The first and second derivatives of (3.44) with respect to time are easily calculated to be

$$\dot{\xi} = \mathrm{e}^{(\lambda_k + i\vartheta_k)t)} \sum a_n \left[(\lambda_k + i\vartheta_k) + in\omega_d \right] \mathrm{e}^{in\omega_d t}, \tag{3.45}$$

and

$$\ddot{\xi} = \mathrm{e}^{(\lambda_k + i\vartheta_k)t)} \sum a_n \left[(\lambda_k + i\vartheta_k) + in\omega_d \right]^2 \mathrm{e}^{in\omega_d t}. \tag{3.46}$$

[4] In particular, this implies that the oscillations of the unstable modes have a frequency set exactly by the driving frequency ω_d, regardless of the natural frequency as defined by the dispersion relation (3.29).

Defining $\Omega_n = [(\lambda_k + i\vartheta_k) + in\omega_d]$, we can write equation (3.43) in terms of the generalized solutions:

$$\mathrm{e}^{(\lambda_k+i\vartheta_k)t}\Big\{\sum a_n\left(\Omega_n^2+2\gamma_k\Omega_n+\delta_k\right)\mathrm{e}^{in\omega_d t} + \sum a_n\left(\tfrac{1}{2}\epsilon_k\,\mathrm{e}^{i(n+1)\omega_d t}+\tfrac{1}{2}\epsilon_k\,\mathrm{e}^{i(n-1)\omega_d t}\right)\Big\}=0. \quad (3.47)$$

Rearranging the second sum, we can group terms with the same frequency (this procedure has the name *harmonic balancing*) and we have

$$\mathrm{e}^{(\lambda_k+i\vartheta_k)t}\sum\left[a_n\left(\Omega_n^2+2\gamma_k\Omega_n+\delta_k\right) + \tfrac{1}{2}\epsilon_k a_{n-1}+\tfrac{1}{2}\epsilon_k a_{n+1}\right]\mathrm{e}^{in\omega_d t}=0. \quad (3.48)$$

Since equation (3.48) is valid for each n, we can disregard the exponentials, and rewrite it as an infinite tridiagonal system:

$$\mathscr{H}_\infty\cdot\vec{a}_\infty=\begin{pmatrix}\ddots & \ddots & \ddots & 0 & 0 & 0 & \vdots\\ \dots & \frac{1}{2}\epsilon_k & D_{n-1} & \frac{1}{2}\epsilon_k & 0 & 0 & \dots\\ \dots & 0 & \frac{1}{2}\epsilon_k & D_n & \frac{1}{2}\epsilon_k & 0 & \dots\\ \dots & 0 & 0 & \frac{1}{2}\epsilon_k & D_{n+1} & \frac{1}{2}\epsilon_k & \dots\\ \dots & 0 & 0 & 0 & \ddots & \ddots & \ddots\end{pmatrix}\begin{pmatrix}\vdots\\ a_{n-2}\\ a_{n-1}\\ a_n\\ a_{n+1}\\ a_{n+2}\\ \vdots\end{pmatrix}=0, \quad (3.49)$$

where we have defined $D_n = (\Omega_n^2 + 2\gamma_k\Omega_n + \delta_k)$ as the nth diagonal entry.

Since equation (3.48) is homogeneous, the determinant of the above matrix (called *Hill's determinant*) must vanish [8]. This, in turn provides an equation for the complex number $(\lambda_k + i\vartheta_k)$.

In practice, the infinite sum in equation (3.44), as well as the linear system in (3.49) is truncated so that $n \in [-N, N]$,

We can write the truncated equation for $(\lambda_k + i\vartheta_k)$ as

$$\mathscr{H}_N\cdot\vec{a}_N=\begin{pmatrix}D_{-N} & \frac{1}{2}\epsilon_k & 0 & \dots & 0\\ \frac{1}{2}\epsilon_k & D_{-N+1} & \frac{1}{2}\epsilon_k & \dots & 0\\ \ddots & \ddots & \ddots & \ddots & \ddots\\ 0 & \dots & \frac{1}{2}\epsilon_k & D_{N-1} & \frac{1}{2}\epsilon_k\\ 0 & \dots & 0 & \frac{1}{2}\epsilon_k & D_N\end{pmatrix}\begin{pmatrix}a_{-N}\\ a_{-N+1}\\ \vdots\\ a_{N-1}\\ a_N\end{pmatrix}=0. \quad (3.50)$$

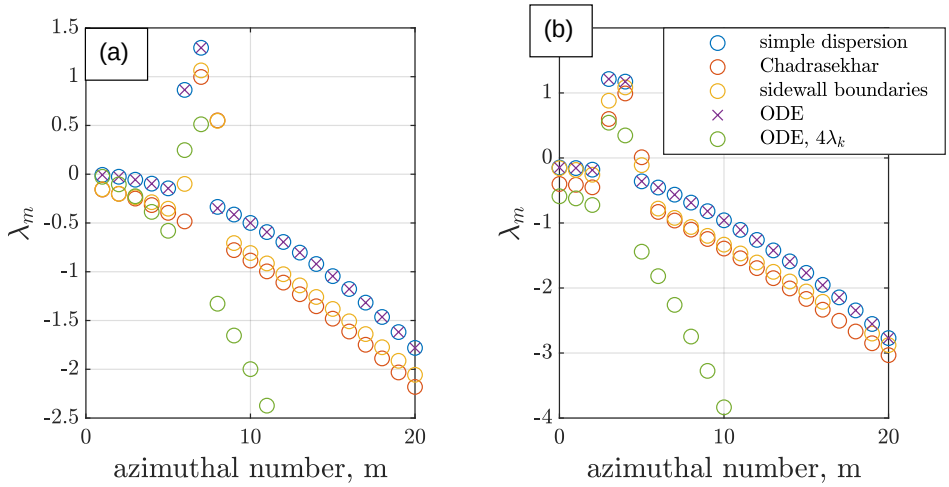

Figure 3.2: Results for simulations of the shaker for each of the presented theories in this chapter. Panel a) depicts the predicted amplification rates for each azimuthal number m corresponding to the first k-value of the order-m Bessel equations (3.11), and panel b) corresponds to the second. Values of λ_m below zero represent modes for which damping is dominant.

The truncated Hill's determinant produces a single equation,

$$\det\left[\mathscr{H}_N(\lambda_k + i\vartheta_k)\right] = 0, \tag{3.51}$$

which can be solved for $(\lambda_k + i\vartheta_k)$ numerically, using generalized eigenvalues. The results of this analysis (using measured fluid parameters) are shown in Figure 3.2.

3.3 Including horizontal boundary layers, and viscosity at the interface

While the work done in [52] did much to align the theory of Mathieu equations and Floquet analysis with the fluid theory, more often than not, there were large discrepancies in theoretical and experimentally obtained stability curves [53]. Kumar and Tuckerman [43] expanded the simple dispersion theory above to include boundary layers with nonzero vorticity at the upper and lower boundaries of the fluids, as well as at the interface. This treatment

follows the stability analysis of Chandrasekhar in [44], and special mention is made of the importance of the continuity of the transverse component of the stress tensor across the interface. [5]

The following is adapted from both [44] and [43], in order to approximate the Floquet exponent λ_k (as opposed to identifying regions of stability). We assume that the equation of motion is still separable, and linear. When the background velocity is negligible, the Navier Stokes equations for the velocity perturbations can be factorized as [78]:

$$(i\rho\omega_k - \mu\nabla^2)\left(\vec{U} + \frac{1}{i\omega}\nabla p\right) = 0. \tag{3.52}$$

We can write the solution $\vec{U}$ as a sum of irrotational and viscous components:

$$\vec{U} = \vec{u} + \nabla\phi. \tag{3.53}$$

$\vec{u}$ is a boundary layer satisfying $(i\rho\omega - \mu\nabla^2)\vec{u} = 0$, and ϕ is a velocity potential satisfying $\left(\nabla\phi + \frac{1}{i\omega}\nabla p\right) = 0$. It is assumed that the boundary layer $\vec{u}$ goes rapidly to zero away from the vessel walls.

For two fluids, indexed by j, we once again denote the velocity components as $\vec{U}_j = \vec{u}_j + \nabla\phi_j$, and in what follows, W_j indicates the z component of the velocity in fluid j. In the fluid bulk, we are governed by equation (3.52). In the z-direction, this has solutions given by $W_j = \partial_z\phi_j + w_j$, where the velocity potential can once again be expanded according to equation (3.8). For the sake of clarity, we repeat the general solution here, supressing the radial and azimuthal components:

$$\phi_1 = \sum_k \left(a_1 \sinh(k[z + h_0]) + b_1 \cosh(k[z + h_0])\right)\varphi_{1,k}, \tag{3.54}$$

$$\phi_2 = \sum_k \left(a_2 \sinh(k[z - h_0]) + b_2 \cosh(k[z - h_0])\right)\varphi_{2,k}. \tag{3.55}$$

The boundary layer equation has the general solution

$$w_1 = \sum_k c_1 \, \mathrm{e}^{-q_{1,k}[z+h_0]} + d_1 \, \mathrm{e}^{q_{1,k}z}, \tag{3.56}$$

$$w_2 = \sum_k c_2 \, \mathrm{e}^{q_{2,k}[z-h_0]} + d_2 \, \mathrm{e}^{-q_{2,k}z}. \tag{3.57}$$

[5] Unfortunately, this implies that the boundary layers at the interface are rather important, making further simplifications to the theory questionable.

The eigenvalues $q_{j,k}$ satisfy the boundary layer equation in (3.52):

$$q_{j,k}^2 = \frac{i\rho_j\omega_k}{\mu_j} + k^2. \tag{3.58}$$

In everything that follows, we will suppress the k subscript in the q_j to improve readability.

The boundary equations at $z = \pm h_0$ are described by impenetrability ($W_j = 0$), and the no-slip condition ($U_r = U_\theta = 0$ paired with the continuity equation together imply that

$$\partial_z W_j = 0. \tag{3.59}$$

Since the d_j terms are exponentially suppressed far from the interface, the impermiability condition at $z = \pm h_0$ gives,

$$W_j = ka_j + c_j = 0 \tag{3.60}$$

for each j. Likewise, the no-slip condition gives

$$\partial_z W_1 = k^2 b_1 - q_1 c_1 = 0, \qquad \text{and} \tag{3.61}$$

$$\partial_z W_2 = k^2 b_2 + q_2 c_2 = 0. \tag{3.62}$$

Eliminating the c_j from equations (3.60) and (3.61) we find that

$$a_1 = -\frac{k}{q_1} b_1, \tag{3.63}$$

$$a_2 = \frac{k}{q_2} b_2. \tag{3.64}$$

This, in turn, allows us to define simplified expressions for ϕ_1 and ϕ_2. Starting with,

$$\Gamma_1 = \left(-\frac{k}{q_1} \sinh(k[z + h_0]) + \cosh(k[z + h_0]) \right), \tag{3.65}$$

$$\Gamma_2 = \left(\frac{k}{q_2} \sinh(k[z - h_0]) + \cosh(k[z - h_0]) \right). \tag{3.66}$$

We have

$$\phi_j = b_j \Gamma_j \varphi_j. \tag{3.67}$$

At the fluid-fluid interface, the boundary equations come from the requirements of continuity for the velocity, the incompressibility condition, continuity of the tangential component of the stress tensor, and the dynamic boundary condition [44, 43]. These are, respectively:

$$\Delta W_j = 0, \tag{3.68}$$

$$\Delta \partial_z W_j = 0, \tag{3.69}$$

$$\Delta \mu_j \left(\partial_z^2 + k^2\right) W_j = 0, \tag{3.70}$$

$$\Delta \left[\rho_j \partial_t - \mu_j(\partial_z^2 - k^2) + 2\mu_j k^2\right] \partial_z W_j = -\left[\Delta \rho_j g(t) k^2 - \tau k^4\right] \xi. \tag{3.71}$$

At the interface, the c_j terms are exponentially suppressed, leaving us with four equations for the four unknowns b_1, b_2, d_1, d_2. While it is possible in theory to obtain an exact equation for the interface height, in practice the resulting equations are completely intractable. Instead, we use a computer algebra system (either Sage or Matlab's symbolic package) to find expressions for d_1, d_2 and b_2, and then we plug these expressions into the dynamic boundary condition.

The resulting system can be written in terms of a new dispersion function D_n, as well as a new parametric amplitude function ϵ_k. This leads once again to the same system of equations as in equation (3.49), and Hill's determinant, equation (3.51). The predicted results for measured fluid parameters are once again given in Figure 3.2.

3.4 Vertical boudaries

The analysis of Kumar and Tuckerman did not take into account finite system size. As a final effort to estimate the Floquet exponents for different modes in the system, an attempt was made to include lateral boundary layers at the inner and outer sidewalls. This attempt was modeled after the analysis of Chandrasekhar in [44].

We examing the radial component of equation (3.52), and we once again assume that the fluid does not penetrate the vessel walls, which produces the boundary condition

$$U_r = 0 \quad \text{at} \quad r = \{r_1, r_2\}. \tag{3.72}$$

The no-slip condition together with the continuity equation (see equation

(3.59)) produces

$$\begin{aligned}\nabla\vec{U} = \nabla U_r\hat{r} = \frac{1}{r}\partial_r r U_r = 0,& \\ \implies U_r + \partial_r U_r = 0,& \\ \implies \partial_r U_r = 0 \quad \text{at} \quad r = \{r_1, r_2\},& \end{aligned} \tag{3.73}$$

where the last line is due to impenetrability. The velocity potential has the familiar solutions from the invicid flow theory, given in equation (3.8).

Since the boundary layer goes rapidly to zero away from the vessel walls, the rotational component of equation (3.52) can be very well-approximated by [78]

$$\left[i\rho\omega_k - \mu^2\left(\frac{1}{r}\partial_r + \partial_r^2\right)\right] u_r = 0. \tag{3.74}$$

This equation has a general solution of the form [72],

$$u_r(r) = \sum_k c_r K_0(s_k r) K_0(s_k r_1)^{-1} + d_r K_0(s_k r_2) K_0(s_k r)^{-1} \tag{3.75}$$

$$\simeq \sum_k c_r\, \mathrm{e}^{-s_k(r-r_1)} + d_r\, \mathrm{e}^{s_k(r-r_2)}\,. \tag{3.76}$$

In the above, K_0 is a modified Bessel function (of order zero) of the second kind, and c_r and d_r are constants. [6] The eigenvalue s_k is a solution to equation (3.74), and is related to the frequency ω_k by

$$s_k^2 = \frac{-i\omega_k\rho}{\mu}. \tag{3.77}$$

The summation in equation 3.75 is over the variable k due to the eigenexpansion of the velocity potential in equation (3.8), and the subscript in the variable s_k is included to make the frequency and wavenumber dependence of the boundary equation explicate.

[6] The final line is justified via the first-order term in the asymptotic relation [79],

$$K_\nu(z) \sim \sqrt{\frac{\pi}{2z}}\,\mathrm{e}^{-z}\left(1 + \frac{4\nu^2 - 1}{8z} + \frac{(4\nu^2-1)(4\nu^2-9)}{2!(8z)^2} + \ldots\right.$$

and has been verified numerically to be within 10^{-8} for all relevant values of the complex number z.

Substituting the above solutions into the boundary equations (3.72) and (3.73) produces the following transcendental system of equations for the constants of integration:

$$U_r(r_i) = c_r\,\mathrm{e}^{-s_k(r_i-r_1)} + d_r\,\mathrm{e}^{s_k(r_i-r_2)} + a_r k H_m^{(1)\,\prime}(kr_i) + b_r k H_m^{(2)\,\prime}(kr_i) = 0 \tag{3.78}$$

$$U_r'(r_i) = -c_r s_k\,\mathrm{e}^{-s_k(r_i-r_1)} + d_r s_k\,\mathrm{e}^{s_k(r_i-r_2)} + a_r k^2 H_m^{(1)\,\prime\prime}(kr_i) + b_r k^2 H_m^{(2)\,\prime\prime}(kr_i) = 0 \tag{3.79}$$

where r_i denotes $r_{1,2}$, and the prime indicates a derivative with respect to r.

When evaluating $u_r(r)$ at r_1 and r_2, it is readily seen from equation (6) that $u_r(r_1) = c_r + \varepsilon$, and $u_r(r_2) = d_r + \varepsilon$, where $\varepsilon \sim e^{-|s_k|(r_2-r_1)}$, which is essentially zero. [7] By approximating $u_r(r_1) = c_r$ and $u_r(r_2) = d_r$, equation (3.78) at r_1 and r_2 gives

$$c_r = -\,a_r k H_m^{(1)\,\prime}(kr_1) - b_r k H_m^{(2)\,\prime}(kr_1) \tag{3.80}$$

$$d_r = -\,a_r k H_m^{(1)\,\prime}(kr_2) - b_r k H_m^{(2)\,\prime}(kr_2). \tag{3.81}$$

Plugging these equations into equation (3.79) at r_1 and r_2, while approximating $u_r'(r_1) = -s_k c_r$ and $u_r'(r_2) = s_k d_r$ we find that either $a_r = b_r = c_r = d_r = 0$, or

$$\begin{aligned}&\big(s_k H_m^{(1)\,\prime}(kr_1) + k H_m^{(1)\,\prime\prime}(kr_1)\big)\big(k H_m^{(2)\,\prime\prime}(kr_2) - s_k H_m^{(2)\,\prime}(kr_2)\big)\\ &-\big(s_k H_m^{(2)\,\prime}(kr_1) + k H_m^{(2)\,\prime\prime}(kr_1)\big)\big(k H_m^{(1)\,\prime\prime}(kr_2) - s_k H_m^{(1)\,\prime}(kr_2)\big) = 0.\end{aligned} \tag{3.82}$$

For fixed ω_k, this equation can be solved for k numerically. The results comparing this analysis with the theories in the previous sections are shown in Figure 3.2.

Note that equation (3.77) produces a dynamic relationship between the wavenumber and the frequency. This needs to be taken into account when one solves for the allowable modes in the system. The solution is obtained by first assuming that $s_k = 0$, and then recursively approximating k and the Floquet exponent λ_k. Further, for a two-fluid system indexed by j, it is not generally true that the kinematic viscosity $\nu_j = \frac{\mu_j}{\rho_j}$ will be the same

[7] This is due to the magnitude of the eigenvalues s_k. Even for low frequencies and conservative estimates for the density and viscosity, the magnitude of s_k will still be quite large (as can be seen immediately from equation (3.77).

in each fluid. In this case, equation (3.82) must be solved independently for each fluid, and consequently each fluid will have disparate values of k (even though the geometry of the boundaries remains the same).

3.5 A phenomenalogical model

It should be noted that none of the above theories were successful in predicting the Floquet exponents that we observed in experiments. In fact, none of the analysis above were even able to predict the correct eigenmodes to be excited. These findings are consistent with the general agreement that even if the fluid theory is accurate, it can be extremely difficult to match this theory with fluid parameters such as viscosity and surface tension (see [76] for a bit of meta-analysis on this topic). Universally, we observed a great deal more damping than any of the theories predicted. [8]

As it turns out, accurately predicting the dissipation rate of interface waves is a rather difficult task. In one study, agreement with the disipation rates predicted by theory was only found when the fluid vessel (made of brass) was polished to a mirror finish [45]. In this study, it was noted that "Roughnesses whose depth was small compared to the boundary layer thickness had a remarkably large effect." This is even more remarkable when one consideres that boundary layer thickness is again much smaller than the wavelength of the modes in question (since wavelength is generally the length-scale considered in the irrotational theory) [10].

To complicate things further, none of the above theories account for meniscus effects on the lateral boundaries. A nonzero meniscus will result in different eigenvalues k allowable in the fluid vessel, and it has been noted that unless the interface is somehow pinned to a specific height, the strict quantization of the allowable k values in the system is somewhat blurred (resulting in a less discrete range of frequencies) [41, 42]. In all of the above theories, it is assumed that the velocity potential obeys Von Neumann boundary conditions, equivalent to a contact angle of 90°.

Theoretical treatments allowing for various contact angles have been given (see [53] in addition to the above), however to this author's knowledge, there has been no rigourous confirmation of these predictions beyond demonstration that the stability curves are altered when the contact angle is

[8] Even when we multiplied the daming term from section 3.1 by the customary factor of 2.

changed [80], or that theories have a "plausible agreement [53]" with experiments when certain physical parameters are assumed .

All of these complications can perhaps make the prospect of predictions seem pretty bleak, however there is a bit of light at the end of the theoretical rabbit-hole. A more recent experimental study investigated stability curves using the simple dispersion theory outlined in section 3.1. This group found very good agreement with theoretical predictions using equation (3.29), so long as they multiplied the damping found in [10] by a factor of 8. [9]

The efficiency of this methodology cannot be argued with. One may simply adjust the value of γ_k until it matches experiments, and then one is free to use any standard numerical method to solve equation (3.29) as an ODE. All of the uncertainty when dealing with fluid parameters vanishes!

Approximating the Floquet exponents with an ODE also has a secondary benefit. In the Floquet theories presented above, a perfect (and eternal) sinusoidal acceleration is assumed, making it difficult to estimate the effects of finite shaking intervals, and shaker noise. The final method of predicting the Floquet exponent therefore consists of solving the ODE given by equation (3.29), and numerically extracting the exponential amplification rate that results by fitting a linear polynomial to $\log|\xi_k|$. The value of γ_k used can be either adjusted to provide the best experimental fit, or set directly using experimentally obtained dissipation rates.

Figure 3.2 compares the predictions of the different methods. In both panels, we see that there is a cluster of modes which interact with the shaker strongly enough to become amplified. This occurs around the $m = 7$ mode for the first radial wavenumbers (panel a), and around $m = 4$ for the second (panel b). [10] The ODE simulations (denoted by the $\times$ symbol) match the simple dispersion Floquet predictions for the same simulated parameters, as expected. The Chadrasekhar Floquet theory used by Kumar and Tuckerman does produce different predictions than the simple dispersion relation. However it appears that correcting for the boundary layers on the sidewalls does not significantly change the predicted amplification rates for most modes when comparing to the Chandrasekhar theory. The modes that do change significantly appear to be at the extreme ends of the amplified clusters, suggesting that a small shift in natural frequency is causing a significant shift

[9] Recall that the value in equation (3.30) is off from standard predictions found in [10] by a factor of 2. Compared to our damping result, the authors had to multiply by 16.

[10] The first and second radial wavenumbers correspond to the smallest and second smallest nonzero solutions of equations (3.11) and (3.82).

in the predicted amplification rate.

The simulations labeled 'ODE, $4\lambda_k$' show significantly smaller amplification rates then any of the other simulations. These correspond to the ODE equation (3.29) with $4\times$ the theoretical damping found in [10]. In Chapter 6, we will see that the ODE simulation produces excellent results for the $m = 4$ mode when we simulate the system using accelerometer data from the experiment and experimental values of the dissipation rate. As we shall see this correspondence with a completely linear simulation will provide a valuable comparison to data, as a way of testing whether deviations from expected behavior are due to nonlinearities.

Chapter 4

Experimental concept and methodology

The theories described in the previous chapter pertain to a system which undergoes sinusoidal oscillations perfectly aligned with the acceleration due to gravity, and the analysis described in Chapter 2 is predicated on a large number of individual experiments with identical laboratory conditions and parameters. Theoretically and numerically, these constraints are quite easy to implement, but in practice matching these assumptions requires careful design and calibration.

In this chapter, we will examine some of the more imporant mechanical aparatus developed to ensure that we are as close to the theoretical framework as experimental precision will allow. The first item discussed will be the aparatus used to produce vertical oscillations, hereafter referred to as the shaker. After this, we will examine the detection method for measuring the interface waves. We will then provide a brief discussion of the automation process, and the steps taken in order to procure a large number of experimental runs. We will close this chapter with the design of the fluid cell.

4.1 Vertical sinusoidal oscillations, and the design of the Shaker

In order to enable reliable statistical analysis, the conditions of individual experimental runs must be kept as consistent as possible. In this section, the overall design of the apparatus used to subject the two-fluid system to

approximately vertical sinusoidal oscillations will be discussed.

We will first explain the concept behind the shaker design, pointing out the most important components and explaining their relavance. The procedure for aligning the shaker so that the oscillations are approximately vertical (parallel to the acceleration due to gravity) will be briefly explained. For more details on the calibration of the accelerometer, and the alignment process, see Appendix B.

4.1.1 Concept and Mechanics

The shaker was designed as a driven simple harmonic oscillator, and is depicted in Figure 4.1. In the following, the components detailed will be referenced by their corresponding number in the figure. The entire system rests on an active noise-cancellation, auto-leveling optical table corresponding to (0) in the figure. [1] The springs (1) are selected such that the natural frequency of the spring-mass system matches the desired frequency of the shaker's oscillations.

Vertical guides were incorporated into the design in order to reduce unwanted horizontal motion. The vertical guides were built using frictionless air-bearings (2), confined to move along 20mm diameter steal posts, chosen to drastically exceed the expected horizontal forces from the shaker motion, without taking up too much space in the experimental design. The air-bearings themselves provided a frictionless surface of air $\sim 10\mu$m thick, and provided a restoring force of $23\text{N}\mu\text{m}^{-1}$ whenever the system was pushed out of equillibrium [81].

The resonant spring-mass system acts as a mechanical filter reducing mechanical noise, and ensuring that higher harmonics of the driving frequency are unlikely. In addition, the resonant system can be driven with very little input, and a simple 8Ω speaker (3) [2] driven at less than 1.5V was found to be more than adaquate. In order to ensure that the oscillations produced were sinusoidal, and restricted to vertical, an accelerometer [3] (4) was used to measure the driving frequency oscillations in three orthogonal directions, and adjustment screws (5) were used to minimize horizontal accelerations. The accelerometer was also used to set the driving frequency of the shaker as in the following procedure: Starting with the observed frequency for damped

[1] Thorlabs, PTS602

[2] Tectonic, TEBM65C20F-8

[3] Analog Devices, EVAL-ADXL354

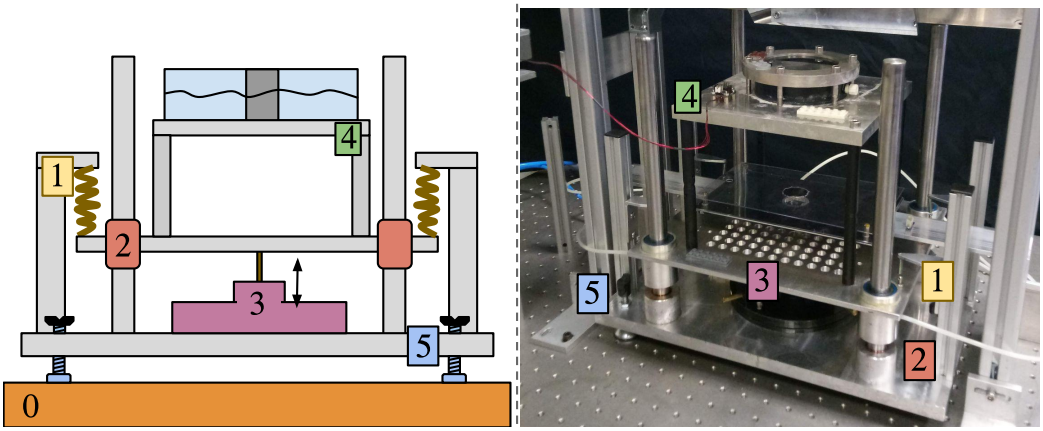

Figure 4.1: Schematic of the shaker design.
The entire system rests on a noise-isolating, auto-leveling optical table (0).
The springs (1) are selected so that the natural frequency of the spring-mass system matches the desired frequency of shaker oscillations.
The vertical guides (2) restrain the system on a frictionless cushion of air.
Since the system is driven at resonant frequencies, a small electromagnetic driver (3) is capable of producing the required oscillations.
The motion is recorded using a high-precision accelerometer (4), and the system is aligned to vertical using leveling screws (5).

oscillations measured when the spring-mass system was pertubed from rest, a narrow frequency sweep, in increments of 0.025 Hz was conducted. The driving frequency was then chosen to correspond to the peak amplitude of this frequency sweep.

Figure 4.2 shows an example of the accelerometer data for a single shaker experiment. In panel a), we can see the acceleration data as a function of time. The vertical dashed lines indicate the window for the FFT analysis, which is much more informative. In panel b), we see that the x and y components of the accelleration are more than two orders of magnitude smaller than the vertical at the driving frequency (6 Hz in this example). The higher harmonic peak for $\tilde{a}_z$ at 12 Hz is due to distortion of the sine wave.

4.2 The Detection Method

The detection method for the interface waves was a type of Fourier Transform Profilometry (FTP)[82], modified to reduce occlusion and localized errors, and to utilize refraction as in a Schlieren technique [83]. Essentially, the Schlieren method provides a map between optical displacements (due to refraction) in a sinusoidal pattern and the gradient of the fluid interface. The FTP method is able to measure sub-pixel optical displacements by comparing this deformed sinusoid to a stationary reference pattern. For a more detailed analysis of the detection method's precision and noise level, see Appendix A.

The interface waves can be modeled as a height field $\xi(x, y, t)$, where ξ describes the perturbed height (relative to the equillibrium height of the fluid interface), and x, y, and t are the laboratory coordinates. When the height field ξ is perturbed away from its horizontal equillibrium, light from a point $p(x, y, t)$ is refracted by the curvature of the interface, which causes an apparent displacement, $\delta\vec{x}$, of the position of p as measured by the camera. A schematic of the optical setup for the detection method is shown in figure 4.3, with the main optical components labeled.

These displacements are related to the gradient of the height field,

$$\nabla\xi = -h_*^{-1}\delta\vec{x}, \tag{4.1}$$

where $\delta\vec{x}$ is the vector displacement, and h_* is an optical parameter given by

$$h_* = \left(\frac{1}{\alpha h_p} - \frac{1}{H}\right)^{-1}. \tag{4.2}$$

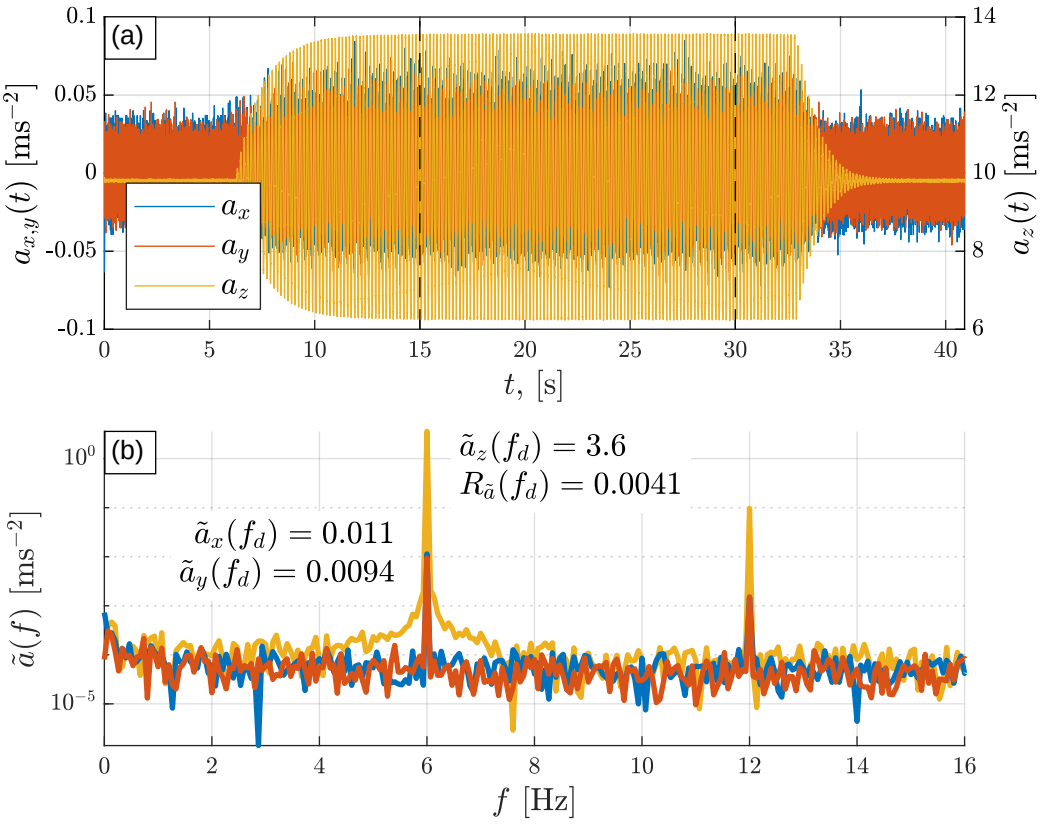

Figure 4.2: Accelerometer data from the shaker .
Panel (a) depicts the acceleration versus time for each of the three axis. Note the scale used for $a_{x,y}$ is two orders of magnitude smaller than the scale used for a_z. The vertical, dashed lines indicate the window used for the Fourier transform in panel (b).
Panel (b) depicts the spectral amplitude for each of the three filters. The spectral amplitude of the x, y and z components are listed, along with the ratio $R_{\tilde{a}}$.

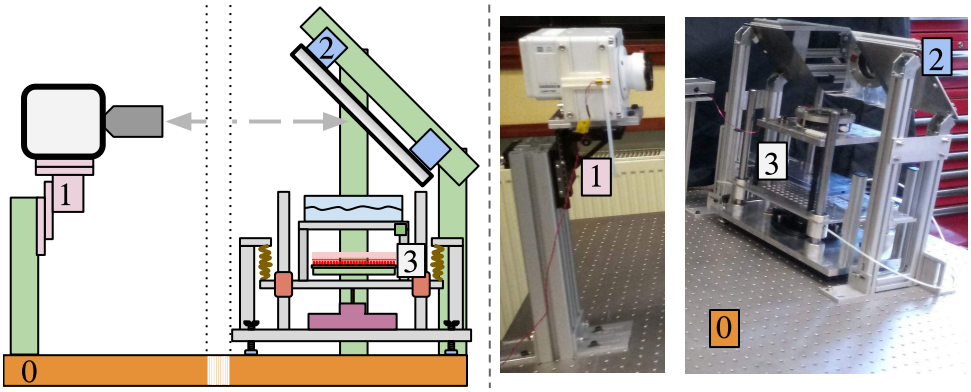

Figure 4.3: Schematic of the optical aparatus for the shaker setup. The entire system is bolted to the optical table (0), so that the relative motion between each of the components is zero. The camera is mounted on translation stages (1) allowing adjustments perpendicular to the optical axis. A custom built kinematic mount for the imaging mirror (2) allows us to align the optical axis to be approximately parallel with the fluid cell's axis of symmetry (see Figure 4.4). The periodic pattern used in the detection method is illuminated from below (3).

In the above, h_p is the distance between the pattern and the interface, H is the distance between the pattern and the camera, and α is a constant function of the index of refraction for both fluids:

$$\alpha = 1 - \frac{n_{\text{upper}}}{n_{\text{lower}}}. \tag{4.3}$$

The obtained gradient is then integrated to recover the height field ξ.

In order to efficiently measure the displacements $\delta\vec{x}$, a method of Fourier Transform Profilometry (FTP) based on Schlieren analysis is performed [68, 83]. In this method, a periodic pattern is placed below the fluid interface, and images at time t are compared to a reference image, assumed to represent zero displacement. Figure 4.4 shows an example, where we have chosen the mean of 100 stationary images to represent the reference (taking the mean negates possible fluctuations in the reference, better approximating zero displacement).

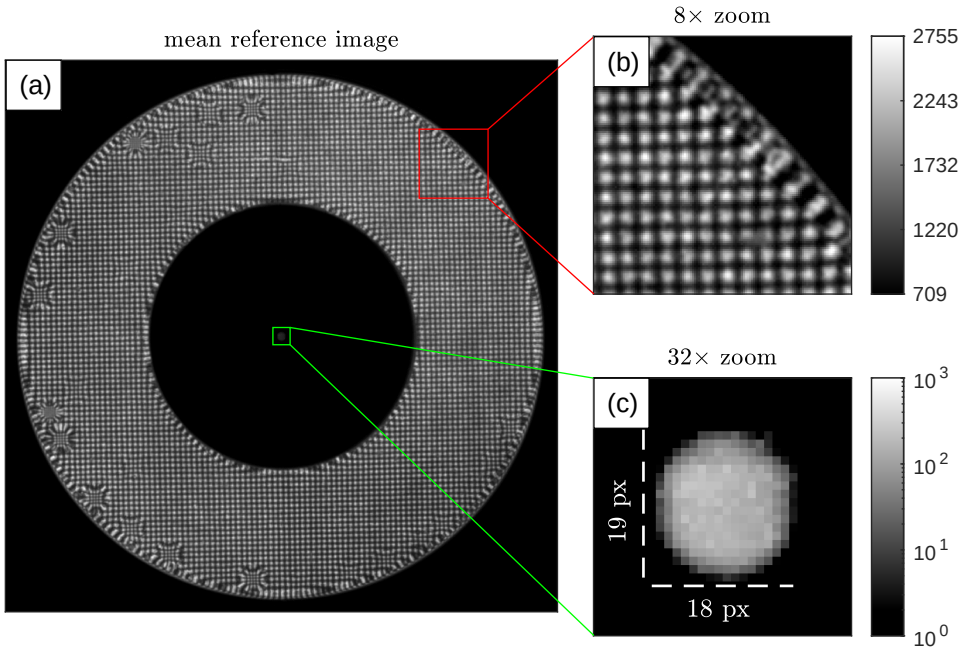

Figure 4.4: Panel (a) is an averaged set of images from the experimental setup. The pattern is a 2-dimensional sinusoid, with equal period in the x and y directions. Note that nearly half of the image is masked by the fluid cell, necessitating the use of a compactly supported filter in the FTP method.
Panel (b) depicts a zoomed-in portion of the image. The color-scale ranges from the minimum pixel intensity value to the maximum pixel intensity value within the pattern, and all pixels obscurred by the fluid cell are zero. At the edge of the fluid cell, we can see that meniscus effects distort the pattern making this region untrustworthy.
Panel (c) depicts the hole drilled into the inner cylindar of the fluid cell. The hole is 1.5mm in diameter, and the height of the cylindar is 30mm. By observing the light that passes through, and comparing the major and minor diameters of the resulting elipse, we can estimate the angle θ between the camera's optical axis and the axis of the fluid cell. By adjusting the mirror shown in figure 4.3, we have reduced θ to less than 0.1°.

4.2.1 Measurement of a known interface

In order to ensure that our detection method produces accurate results, we have tested the method on plano-convex spherical lenses, [4] with focal lengths of $f_1 = 1000$mm, $f_2 = 750$mm, $f_3 = 500$mm, and $f_4 = 250$mm. The lenses are made of N-BK7 glass with a refractive index of $n_{\text{lens}} = 1.515$ [84], and were submerged in pure water $n_{\text{upper}} = 1.33$. The radius of curvature for these lenses, R_i is related to the focal length, f_i by the known formula [84]

$$R_i = f_i(n_{\text{lens}} - 1), \tag{4.4}$$

and the precise specifications of manufacture provide an excellent resource for testing the detection method.

The raw data, and the wrapped phase information is depicted in Figure 4.5. Figure 4.6 depicts the reconstructed height profiles $h(x, y)$ for each of the lenses. Panel (d), which depicts the ratio of a reconstructed diameter over the theoretical radius of curvature provided by equation (4.4) is of special interest. The solid lines represent a reconstruction in which the integration is done in Fourier space, as described in equation (A.51). The dotted line represents the arithmetic mean of trapezoidal integration in the x and y directions separately. In general, spectral integration is expected to produce better results, since it is not based on any finite difference approximations, and is global in nature.

Another interesting feature in panel (d) is the nearly flat nature of each curve. This is indicative that the reconstructions are off by a linear factor in each case, and that this linear factor changes with each lens. Though this may at first seem troubling, we might account for this linear error by noting that each lens has a different thickness according to its method of manufacture. This thickness alters the value of h_p (assumed constant) in equation (4.2) by a small amount. This, in turn causes a change in scale of the approximated gradient in equation (4.1).

4.2.2 Lighting, and other imaging considerations

This section will briefly describe the optical setup for the experiment, including camera alignment, the lighting system, as well as the reasoning behind the camera distance and the camera aperture setting. Figure 4.3 represents

[4] Thorlabs, ESK53-A

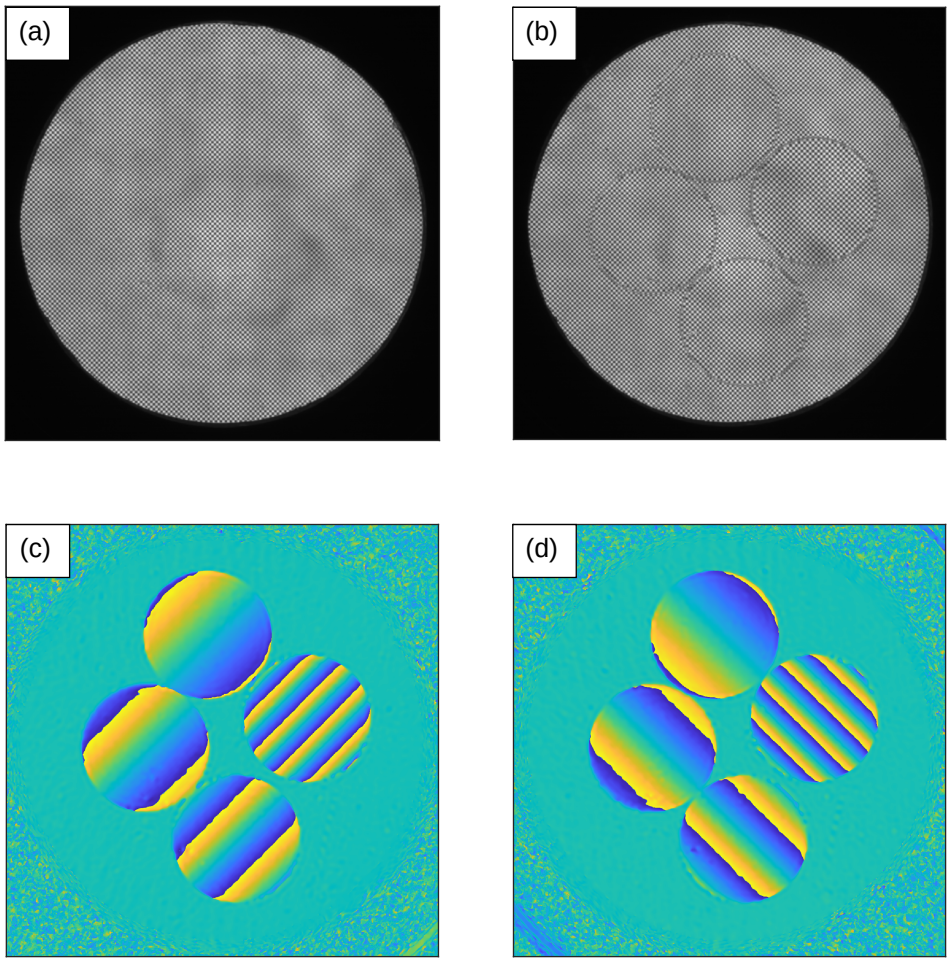

Figure 4.5: Panel (a) depicts the mean reference image, I_0, and panel (b) shows the deformed surface with the lenses. The lower panels show the wrapped phases for the signal extracted from the $(x-y)$ [panel (c)], and the $(x+y)$ [panel (d)] components of the pattern. The range of the colorbar is from $-\pi$ to π. In the experiment conducted, the pattern used was of the form $P(x,y) = A\cos(2\pi k_0 x + 2\pi k_0 y) + A\cos(2\pi k_0 x - 2\pi k_0 y)$, and the resulting phase differences represent displacements in the direction of $\pm 45^\circ$ to the horizontal, and the x and y components are recovered algebraically.

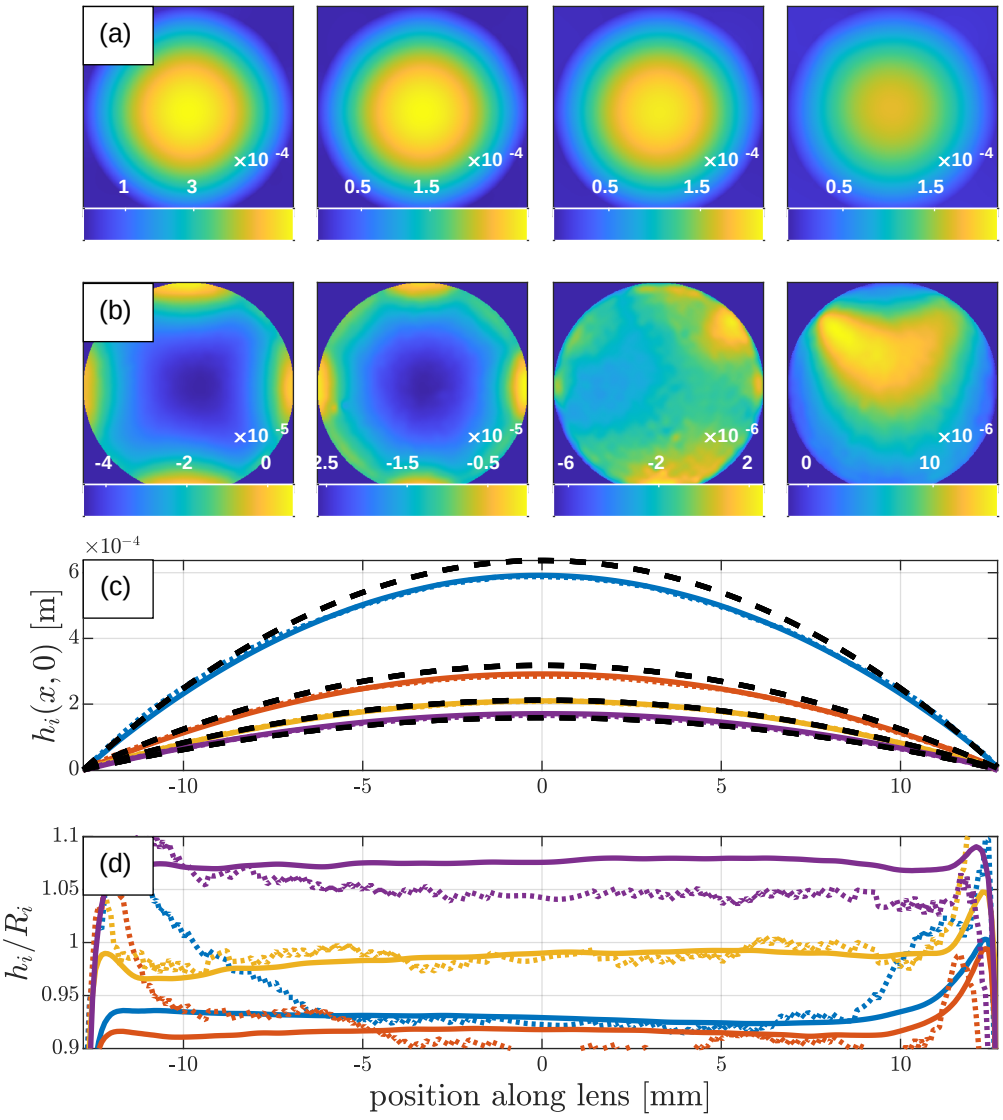

Figure 4.6: Panel (a) depicts the reconstructed height profile (in meters) for each of the four lenses, starting with the lens of highest curvature. Panel (b) shows the difference (in meters) between the reconstructions and the theoretical surfaces defined by equation (4.4). Panel (c) depicts the horizontal diameter of each lens, along with the theoretical value. Dotted lines show reconstructions using the mean of trapezoidal integrations in the x and y directions. Panel (d) shows the ratio of the reconstructions over the theoretical profiles.

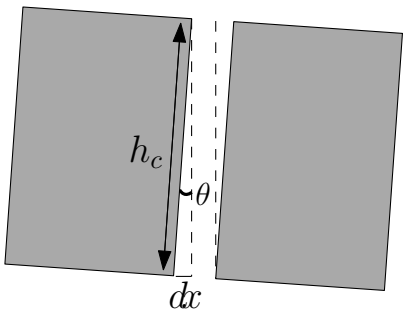

Figure 4.7: Alignment of the optical axis relative to the fluid cell. (The schematic is not to scale.)

the shaker setup including the equiptment built to accomodate the detection method. In order to eliminate relative motion between the components, everything is bolted to the optical table, labeled (0) in the figure. The camera [5] was mounted on translation stages (1) [6] so that the system could be easily centered in the camera's field of view, maximizing the number of pixels used in the detection method.

The system was imaged using a mirror mounted at 45°(2), with purpose-built adjustment screws to facilitate optical alignment. In order to align the optical axis of the system with the axis of the fluid cell, a 1.5mm diameter hole was drilled in the inner cylinder of the fluid cell (see figure 4.4, panel c). The height of the cylinder is $h_c = 30$mm, and the large aspect ratio provided a means of accurately estimating the camera's alignment. If θ is the angle between the optical axis and the axis of the cylinder, and $2\,\mathrm{d}x$ is the width of the obscurred portion of the 2mm aperture, then we have that $\theta = \mathrm{asin}\left(\frac{\mathrm{d}x}{h_c}\right)$ (see Figure 4.7.) By carefully adjusting the mirror, we were able to obtain $2\,\mathrm{d}x = 1\mathrm{px} = 0.04\mathrm{mm}$ (see Figure 4.4, panel (c)), corresponding to an angle of less than 0.1°.

The LED imaging array (3) was designed to provide nearly-uniform high-intensity lighting to be placed below the periodic pattern described above. [7] Each component was mounted in a custom-made printed circuit board (PCB), designed with the help of the electronics technical staff, and were driven using constant-current, low-noise [85] diodes designed specifically for

[5] Phantom VEO 640L, Ametek

[6] Thorlabs, part numbers DTS50/M and DTSA03/M.

[7] Wurth Elektronik, part number 151053RS03000

LED illumination. [8]

The PCB was designed as a tightly packed equilateral grid of 19x20 LEDS, capable of producing 1900cd of luminous intensity. The output is then passed through a number of ground glass optical diffusers [9] placed at 10mm intervals above the array. The diffusers ensure that the discrete grid of lamps appears as a uniform light source to the camera.

The additional illumination provided by the LED array allowed us to reduce the aperature of the camera lens to its minimum value. This served dual purposes in reducing optical noise, and increasing the depth of field.

4.3 Automation and synchronization

The experimental design, and detection procedure both ensure that the important experimental parameters (such as shaker acceleration amplitude, and detection sensitivity) are consistent from experimental run to experimental run. In this section, we will discuss the methodology behind the automation of the system, including a description of the automation script which runs the experiment.

4.3.1 Automation of the shaker using Matlab, and National Instruments card

Each piece of experimental hardware (excluding the camera) was controlled using a National Instruments multi-function data aquisition card, [10] capable of analog and digital input and output. The device was interfaced with Matlab using the (now legacy) `daq.createSession` interface of the Data Aquisition Toolbox [86].

One of the important parameters included in this set is the time $t = 0$ at which the shaker is switched on. In order to synchronize each of the data sets, an indicator LED was mounted on the outside edge of the fluid vessel. This LED was switched on in parallel with the shaker-driver, with a precision better than $\pm 1.25 \times 10^{-4}$s. This allowed us to synchronize each individual experiment to within one timestep (a single image in the video stream).

[8] Diodes Incorporated, part number AL5809.

[9] Thorlabs, part numbers DG100X100-20 and DG100X100-220

[10] National Instruments, PCIe-6363

Additional measurements were made in order to ensure that the experimental conditions from experiment to experiment were consistent. These measurements included the air pressure feeding the air bearings, the voltage output to the indicator LED, and three temperatures sensors were placed at strategic locations: Close to the fluid vessel, on the air supply manifold for the air bearings, and an additional measurement was possible due to a thermometer inside of the accelerometer.

The steps to run a single experiment are as follows:

1. Initialize, and switch on:

   1.A) Initialize the driver, the indicator LED, and the analog inputs for the accelerometer, temperature sensors and other inputs;

   1.B) Initialize the camera;

   1.C) Turn on the imaging LED array, and open the valve for the air bearings using a digital switch;

2. Begin data aquisition:

   2.A) Begin recording images;

   2.B) Pre-shaking pause (6 seconds);

   2.C) Begin recording analog inputs and begin shaking the system;

   2.D) Stop shaker, and synchronization LED;

   2.E) Post-shaking pause (8 seconds);

   2.F) Stop image aquisition, acceleration and temperature measurements;

3. Turn off, download, and save:

   3.A) Switch off the LED array, and switch off the air bearings valve;

   3.B) Download the images and save the accelerometer and temperature data;

In the above procedure, step 1. is performed before the data collection in order to ensure that the steps in 2. run as smoothly and quickly as possible. (In particular, initializing the camera can take a variable amount of time.) The LED array is switched off between experiments in order to prevent overheating of the array and the fluid cell, and to maintain a consistent

illumination profile from experiment to experiment. In step 2.B), we record several seconds of images of the stationary system in order to use their average as a reference (see section A.3 for details). The analog inputs in step 2.C) are started a few milliseconds before the shaker driver and the synchronization LED. After the shaker driver and the synchronization LED are stopped in step 2.D), the spring-mass aparatus, and the interface oscillations continue with exponentially decaying amplitude. The extended period of data aquisition enables the capture of this data.

Step 3. is fairly self-explainatory. Each data set contains thousands of images (roughly 4500 with a framerate of 100 frames per second), and the most stable way to download is as a proprietary `.cine` file, specific to the hardware used. The accelerometer and temperature data are saved as `.mat` files, native to Matlab. The time taken to download and save also provides additional time for the interface waves to return to their initial (unamplified) state. This settling time is necessary if we want the experimental runs to be uncorrelated.

The automation of the camera was facilitated using a proprietary software development kit (SDK) with a Matlab interface. This SDK is not in widespread use, and support from the developer was extremely limited.

4.4 Fluid cell designs, and fluid choices

As the experiment progressed, it became more and more apparent that in order to eliminate problems with the fluid cell and the procedure for filling it, we would need to test a large number of filling methods and this was made quite difficult when additional safety measures were required. In what follows, we will examine the different cell designs, as well as the problems encountered and solutions which lead to further iterations.

4.4.1 Fluid choices, and influence on cell design

The initial experiments were attempted in an open air–water system. This system was soon discared for two reasons. The first was due to the significant surface tension contribution, both to the dispersion relation, and in the form of a meniscus which formed at the vertical boundaries of the system.

Since the meniscus is dependent on the surface tension, as well as the accelleration due to gravity [10], a time-dependent $g(t)$ produces a time-

dependent mensicus, which manifests as travelling waves moving away from the vertical boundaries. In the air–water system, the effect of the meniscus was prominent enough that the meniscus waves completely dominated the system at early times. The effect of this contribution to the interface waves undergoing parametric resonance is not well understood.

The second reason was perhaps more simple. From the start, the goal was to automate this system, so that we could do statistics on a large number of experimental runs. It was quickly discovered that over the course of several hours, the water in the system would evaporate, reducing the fluid level and changing the experimental parameters. For these reasons, it was decided that a liquid–liquid system in a closed cell would be preferable.

4.4.2 Iterative design of the fluid cell

The fluids used in the experiment were chosen to minimize the effects of surface tension. This was done in order to bring the dispersion relation closer to the linear approximation described in [50], and thus make the analogy with cosmology more applicable.

One of the overarching problems encountered with systems comprising of two liquids was air bubbles trapped in the fluid cell. In particular, when the system was shaking, larger bubbles (modulated by the effective gravity) would oscillate with the oscillating pressure of the fluids. This caused unwanted forced oscillations from the upper window at the driving frequency. In addition, the presence of bubbles (even smaller bubbles) produced deviations and occlusions in the detection method.

Filling the fluid system in such a way that no air was trapped proved to be a difficult design challenge, and the final cell was designed to acomodate fluids that were safe enough to find in a well-stocked kitchen [87], and inexpensive enough to purchase large quantities of. The safety and availability of the final fluid system allowed for dozens of different methods to fill the fluid cell to be attempted. The final filling procedure made it possible to quickly, reliably and reproducibly fill the fluid cell and make adjustments ensuring the absense of bubbles, and an approximately equal volume of each fluid.

Iteration 0: all acrylic fluid cell, with n-butanol–water system.

The first liquid–liquid system that was used for the experiment consisted of n-butanol as the upper fluid, and purified water as the lower fluid. Pu-

rified water has a density of $\rho = 997\text{kgm}^{-3}$, and a dynamic viscosity of $\mu = 0.89\text{mPas}$, at 25°C, and the density and viscosity of n-butanol were taken to be $\rho = 815\text{kgm}^{-3}$, and $\mu = 2.54\text{mPas}$ at 25°C [88]. As explained in section 2, n-butanol was chosen primarily due to the low coefficient interfacial tension with water, $\tau = 1.8\text{mN/m}$ [67].

The main advantages of n-butanol were in the relatively low cost, (less than £40 for a 2.5L bottle [89]) and the fact that it did not chemically interact with transparent acrylic plastic (enabling precise machining of the fluid cell). The primary drawback to using n-butanol was due to safety and disposal concerns [90]. n-butanol is a flamable liquid which causes skin irritation, serious eye damage and the fumes cause respiratory irritation. In addition, n-butanol needs to be disposed of in a sealed container.

Due to the harmful nature of the vapors, the liquid can only be handled under a fume hood. This meant that leaks in the fluid cell were potentially dangerous, and in a short period of time it was seen that these leaks were inevitable with the fluid cell as it was designed. During the final attempt to fill the fluid cell, the base separated from the circular cylinder. The entire system was discarded, and new plans were drawn up.

This failed attempt at the n-butanol–water system provided two important conclusions. The first was that working with a chemical which required a fume-hood for safe handling was out of the question. Even if the fluid cell could be filled successfully, the chances of a leak in the system were far too high. The second was that a great deal more thought had to be put into the fluid vessel if it was going to be filled completely (without air bubbles) with two liquids.

Iteration 1 (nylon cylinders, glass windows, neoprene gaskets)

The next fluid system utilized purified water as the upper fluid, and propylene carbonate as the lower fluid. Propylene carbonate has a density of $\rho = 1205\text{kgm}^{-3}$, and a dynamic viscosity of $\mu = 4.2\text{mPas}$, at 25°C [88], and a surface-tension coefficient of $\tau = 2.8\text{mN/m}$ [67]. This combination was chosen so that we once again minimized the coefficient of surface tension between the two liquids, however we also wanted the fluid to be safer than n-butanol.

The vapor pressure of propylene carbonate is more than 200 times lower than the vapor presure of n-butanol [90, 91]. For this reason, no precautions regarding chemical fumes are necessary. Further, though propylene carbonate

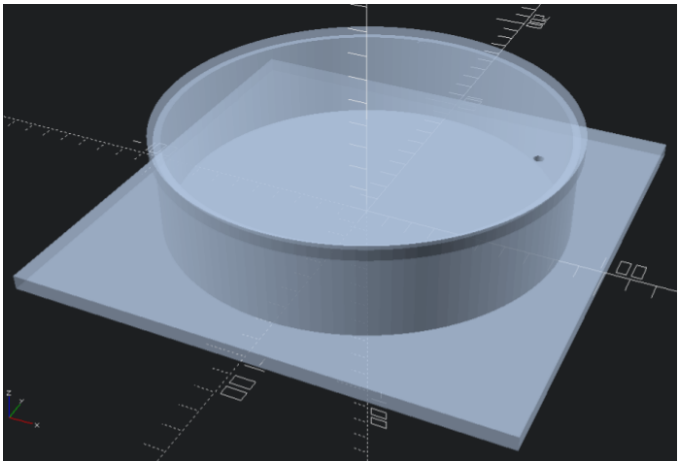

Figure 4.8: A rendered representation of the original acrylic tank. The actual tank was discarded after it broke apart.

may cause skin irritation, it is safe enough to be used in cosmetics at low concentrations [92].

Figure 4.9 is a schematic of the first fluid cell designed to eliminate bubbles. Glass windows were required since transparent plastics are soluble in propylene carbonate. The centeral cylinder was aligned to the axis of the outer cylinder by using an aluminium jig which protruded through the upper window.

The cell was designed to be filled under water in order to eliminate the presense of bubbles, and sealed with neoprene gaskets. Importantly, neoprene is one of the few elastic materials which does not chemically interact with propylene carbonate. The system was then held in an aluminium frame, tightened by six machine screws. After the system was sealed, propylene carbonate could be added, and water removed using hypodermic syringes and septa seals (small rubber seals which close after the needle is removed).

In practice, there were many problems with this design. Most noticably, the neoprene gaskets provided a very poor seal, and the glass windows tended to crack when tightening the aluminium frame. The problem with the gaskets was circumvented by using a great deal of silicone sealant, which proved to be unaffected when submersed in propylene carbonate. Finally, the septa seals tended to provide an excellent point of entry for air, and as time went on it became clear that these seals were not fit for purpose. The septa seals were eventually replaced with threaded luer-lock adapters. These were retro-fitted into place as a temporary solution.

While the first nylon tank was able to produce some preliminary results,

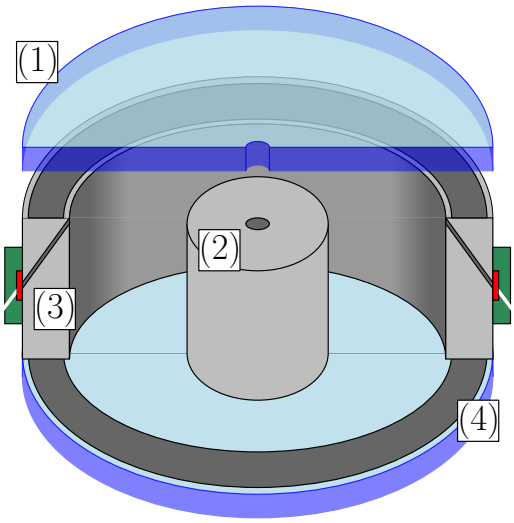

Figure 4.9: The fluid-cell designed for the propylene carbonate–water system. The windows (1) were made from glass, which limited the amount of machining possible. The central cylinder was aligned to the axis of the outer cylinder using an aluminium jig (not shown), through a hole drilled in the glass (2). The entire system was sealed using gaskets (4), and the fluid-levels were adusted using hypodermic syringes and septa-seals (3).

it was clear that the system was not able to produce a consistent experiment. Most of these issues stemed from the fact that propylene carbonate interacted so strongly with plastics. For example, the standard method of making a system of this size air-tight is to use o-rings, however o-rings for large-diameter fittings were not available in neoprene (one of the only plastics that did not dissolve in propylene carbonate). Likewise, the glass windows could not be machined. This reduced the precision of the windows, and necessitated the use of the aluminium jig (which provided another point of entry for air to contaminate the sample).

Iteration 2 (nylon cylinders, o-rings, and acrylic windows)

As many of the problems with the first nylon vessel were due to the use of propylene carbonate, an alternative fluid-fluid system had to be devised. An alternative, novel system was first devised after seeing a Youtube video [93] featuring a demonstration of a fluid-fluid system with "salted out" isopropenol. After much trial and error (mostly done by a labmate), a new system was devised.

The two-phase sytem is in dynamic equillibrium. It consists of an organic phase containing mostly water and ethanol, as well as an aqueous phase containing mostly water and aqueous potassium carbonate. [11] The two-phase

[11] In reality, the organic phase has a small percentage of potassium carbonate, and the

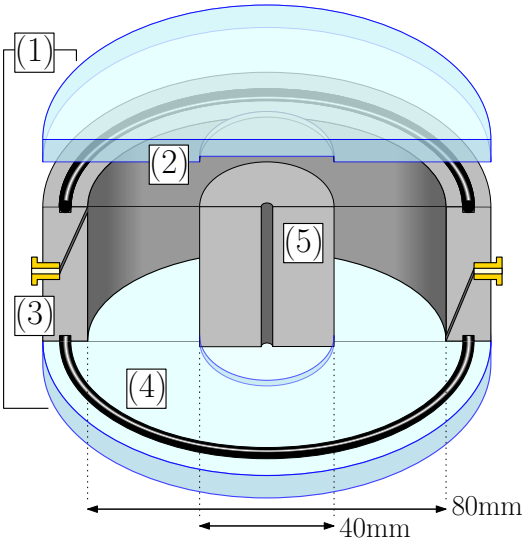

Figure 4.10: The fluid-cell designed for the two-phase system (not to scale). The windows (1) were made from machined acrylic, with a recess (2) cut into the window to hold the inner cylindar (made from nylon) in position. The system was sealed using o-rings(4), and fluid levels were adjusted using luer lock fittings (3). A narrow hole was drilled in the inner cylinder (5) to improve optical alignment.

system has a number of advantages over the water–propylene carbonate system. Perhaps most importantly, this system is far safer. The increased safety provided us with extra opportunities to experiment with different methods for filling the first nylon vessel. This, in turn allowed us to produce a new design better suited to our requirements.

The current fluid-cell is depicted in Figure 4.10. The inner and outer radii of the fluid cell are 20mm and 40mm respectively, and the total depth is 35mm. In this iteration, acrylic windows [12] are machined to accomodate a recess which holds the inner nylon cylinder in place. This provides a more precise alignment, and eliminates another potential path for bubbles to enter the system, as there is no need for an alignment hole.

Because we have fewer restrictions on materials, o-rings are used to seal the system. These are fit in a corresponding recess which provides an engineered seal between the windows and the outer cylinder. Luer locks provide an easy means to add and remove fluids, and to eliminate bubbles. The luer

aqueous phase has a small percentage of ethanol.

[12] It has been observed that acrylic windows are stable in the short-term. However, after long periods, the acrylic will absorb ethanol, swell and become crazed. When experiments are not being conducted, the fluid-cell is filled with water to prevent this.

adapters are threaded directly into the outer cylinder. [13]

The procedure for filling it is as follows:

1. After submerging all of the components and knocking to remove bubbles, the tank is assembled under water.

2. The assembled tank is drained, and rinsed with excess organic solution from the two-phase system. This is repeated.

3. The two phases are added in equal amounts using a syringe. After the syringe is locked in place, the system is pressurized as the fluid is added. When pressure is released, the excess air and bubbles re-fill the syringe.

4. Minute adjustments are made using the same procedure. Additional aqueous solution is added to the top, and the excess volume re-fills the syringe with organic solution. Similarly, additional organic solution is added to the bottom.

Perhaps a note is in order, regarding the final version of the fluid cell, as well as the two fluids. The importance of this final system, its repeatability, safety, and standardised filling procedure cannot be over emphasized. Without a repeatable fluid-fluid sample, free from bubbles and other contaminents, the experiment was not practical. The new tank was also stable, allowing us to run experiments over long periods, obtaining 1500 separate runs for the results shown in Chapter 6.

[13] It is almost not possible to overstate either how incredibly well-engineered the luer lock technology is, or how well it works. Even the end-caps, which produce an air-tight seal are designed to use surface tension to prevent bubbles from entering the system when tightened.
However, much to our dismay, we believe that air is still able to enter the system due to a fault in the threading of the nylon cylinder.

Chapter 5

Analytic Methods

In this chapter, we will outline the methods used to process the data from the experiments. The experimental results will be given in Chapter 6. In the first two sections, we will make the mapping between our real-valued data and the complex mode functions explicate before introducing a time-frequency analysis using wavelets which allows us to differentiate between the propagating and counter-propagating modes defined in Chapter 2.

A more comprehensive examination of mode squeezing in field theory will then be given, including a description of the statistical observations possible in our classical system. Finally, we will examine mode-squeezing in the presense of linear damping, and we will present a normalization method that makes observation of squeezing in damped systems possible.

5.1 Interface wave analysis

5.1.1 Mode functions and cylindrical coordinates

The system under consideration has axisymmetric boundaries, and the wave equation (see Chapter 3, equation (3.8)) is separable in cylindrical coordinates. In this section, we will detail the mapping between the height field measured in our system and the mode functions favored in relativistic field theory using the eigendecomposition of the height field. After this, we will explain the procedure for transforming the data (which is measured on a Cartessian grid using a camera) into cylindrical coordinates via a 2D interpolation. We will finish this section with a demonstration of the effect that

the interpolation method used has on the data.

The height field $\xi(\theta, r, t)$ is composed of Bessel functions in the radial direction, and sinusoids in the azimuthal and temporal directions. Expanding the height field, we have

$$\xi(\theta, r, t) = \sum_{\omega} \sum_{k} \sum_{m} a_{m,k}(t) R_m(rk) \cos\left(m\theta - \omega_{m,k} t + \vartheta_{m,\omega}\right), \tag{5.1}$$

where $R_m(kr) = J_m(kr) + b_{m,k} Y_m(kr)$, and $b_{m,k}$ and k are chosen to satisfy the radial boundary conditions. Similarly, the constant $\vartheta_{m,\omega}$ and the initial value $a_{m,k}(t=0)$ are chosen to satisfy the initial conditions of the system.

The periodic boundary conditions in the azimuthal direction imply that m is an integer, and the frequency is taken to be either a positive or negative real number, and when the product $m\omega_{m,k} < 0$, the mode functions represent waves propagating in the θ direction. Likewise, when $m\omega_{m,k} > 0$, the mode functions represent waves which propagate in the $-\theta$ direction. In what follows, we will often refer to these two cases as *propagating* and *counter-propagating* modes respectively. [1]

From the field theory perspective, quasi-particles are represented by complex exponentials called mode functions, with a well-defined instantaneous amplitude. Recall that the wave equation (represented in k-space) describing the height field $\xi_{m,k}(t)$ is given by

$$\ddot{\xi}_{m,k} + 2\gamma(k)\dot{\xi}_{m,k} + \left(\frac{\tau}{\rho_1 + \rho_2} k^2 + \frac{\rho_1 - \rho_2}{\rho_1 + \rho_2} g(t)\right) k \tanh(kh_0) \xi_{m,k} = 0, \tag{5.2}$$

where the fluid parameters are defined as before.

If $u_{m,k}$ and its complex conjugate $u^*_{m,k}$ form a basis for the solution space of this second order ODE, then we can write the full solution as

$$\xi(\theta, r, t) = \sum_{k} \sum_{m} \xi_{m,k}(t) R_m(kr)\, \mathrm{e}^{im\theta}, \tag{5.3}$$

with

$$\xi_{m,k}(t) = b_{m,k} u_{m,k}(t) + c_{m,k} u^*_{m,k}(t). \tag{5.4}$$

[1] In QFT, the convention is to define the modes with $-\omega_{m,k}t$ terms as positive frequency, and the modes with $\omega_{m,k}t$ terms as negative frequency. We will follow this convention here, however in what follows, propagating (counter-propagating) and positive (negative) frequency will be used interchangably.

Since we require the interface to be a real number, we have that $\xi_{-m,k} = \xi^*_{m,k}$. Further, since equation (5.2) does not depend on the sign of m, [2] we have that $u_{m,k} = u_{-m,k}$. Together, these two facts imply that $c_{m,k} = b^*_{-m,k}$.

Rewriting equation (5.3) as a sum over $m \geq 0$, and supressing the radial component for clarity, we have

$$\xi(\theta, r, t) = \sum_{m\geq 0} \xi_m(t)\, \mathrm{e}^{im\theta} + \xi_{-m}(t)\, \mathrm{e}^{-im\theta} \tag{5.5}$$

$$= \sum_{m\geq 0} \left[b_m u_m + b^*_{-m} u^*_m\right] \mathrm{e}^{im\theta} + \left[b_{-m} u_m + b^*_m u^*_m\right] \mathrm{e}^{-im\theta}\,. \tag{5.6}$$

Equation (5.6) represents the equation that will be used throughout most of the analysis in the sections below. However, for rapidly changing $b_{\pm m}$, it is not so easy to separate the positive and negative frequency signals and so this representation can be a bit misleading. A more natural representation of the modes in the system as real-valued amplitudes is obtained by converting back to real numbers.

If we assume that the mode function u_m has the form $a_m(t)\, \mathrm{e}^{-i\omega_{m,k}t}$, with $a_m \in \mathbb{R}$, and we write $b_m = \frac{1}{2} a_m(t)\, \mathrm{e}^{i\vartheta_{m,\omega}}$, we see that equation (5.6) and (5.1) are the same:

$$\xi(\theta, r, t) = \sum_{m\geq 0} \left(\left[b_m\, \mathrm{e}^{-i\omega_m t} + b^*_{-m}\, \mathrm{e}^{i\omega_m t}\right] \mathrm{e}^{im\theta} + \left[b_{-m}\, \mathrm{e}^{-i\omega_m t} + b^*_m\, \mathrm{e}^{i\omega_m t}\right] \mathrm{e}^{-im\theta} \right), \tag{5.7}$$

$$= \sum_{m\geq 0} \left[b_m\, \mathrm{e}^{im\theta - i\omega_m t} + b^*_m\, \mathrm{e}^{-im\theta + i\omega_m t}\right] + \left[b_{-m}\, \mathrm{e}^{-im\theta - i\omega_m t} + b^*_{-m}\, \mathrm{e}^{im\theta + i\omega_m t}\right]$$

$$= \sum_{\omega} \sum_{m} a_m(t) \cos\left(m\theta - \omega_m t + \vartheta_{m,\omega}\right) \tag{5.8}$$

where the sum over m in the last line includes negative integers once again, and we have continued to supress the radial component.

This seeminly trivial mapping contains a subtle importance within the context of the analogy. In a quantum system, the complex amplitudes b^*_m and b_m are akin to creation and annihilation operators, $\hat{b}^\dagger_m$ and $\hat{b}_m$.

[2] While the eigenvalues k depend on m, the transcendental equations which determine the values of k are invariant with respect to the sign of m, and the equation of motion is likewise invariant with respect to the sign of k.

In our classical system, the (real) amplitude $a_m(t)$ is continuously observable with non-destructive measurements, and it can be seen from equation (5.7) that the b_{+m} terms correspond to propagating modes, and the b_{-m} amplitudes correspond to counter-propagating modes. On the other hand, the representation in (5.8) which leads directly to the real representation of the field demonstrates that if the propagating and counter-propagating modes are to be measured separately, then they must first be resolved into positive and negative azimuthal components.

In the next section, we will outline the interpolation procedure used to transform the rectilinear height-field data (obtained from the digital camera) to the cylindrical coordinates corresponding to the symmetry of the fluid cell.

5.1.2 Coordinate transformation of data

In this section, we will explain the interpolation procedure used to transform the experimental data from Cartesian to cylindrical coordinates. We will then provide a comparison of the interpolation methods standard in Matlab, and we will finish by demonstrating the effect of white noise on this transformation.

Since the data is created in Cartesian coordinates, the interpolation must be defined in terms of Cartesian coordinates. For example, we set c, d to be integers ranging from 0 to $N-1$, and define

$$x = 2\left(\frac{c}{N} - \frac{1}{2}\right), \tag{5.9}$$

$$y = 2\left(\frac{d}{N} - \frac{1}{2}\right), \tag{5.10}$$

so that $x, y \in [-1, 1)$. An $N \times N$ image $I[c, d]$ can now be defined in terms of these coordiantes,

$$I[d, c] \equiv I\big(x[c], y[d]\big) \tag{5.11}$$

and we are careful to note that the indices change positions:

$$[\text{row}, \text{column}] \mapsto \big(x[\text{column}], y[\text{row}]\big). \tag{5.12}$$

We define our query points for the interpolation in polar coordinates first. For minimum and maximum radii r_1 and r_2, we set

$$r[a] = r_1 + \frac{a}{N_r - 1}\left(r_2 - r_1\right), \tag{5.13}$$

where a is an integer ranging from 0 to $N_r - 1$, and $N_r \simeq \frac{N}{2}(r_2 - r_1)$ is an integer chosen to correspond to the actual number of points being sampled.

Likewise, we can estimate the number of points in the azimuthal direction as an integer, $N_\theta \simeq 2\pi\frac{N}{2}r_1$, [3] allowing us to define the azimuthal coordinate

$$\theta[b] = 2\pi\left(\frac{b}{N_\theta} - \frac{1}{2}\right), \tag{5.14}$$

where b is once again an integer ranging from 0 to $N_\theta - 1$.

The query points for the interpolation are now defined using the polar coordinates:

$$x_q[a,b] = r[a]\cos\left(\theta[b]\right), \tag{5.15}$$
$$y_q[a,b] = r[a]\sin\left(\theta[b]\right). \tag{5.16}$$

Specifically, we use Matlab's `interp2` function, which interpolates using one of five methods:

- `nearest` (Nearest neighbor), simply sets the value of the query point to the value of the nearest sample; this method is the only discontinuous interpolation method available.
- `linear` sets the value using a bilinear interpolation formula (which is just a linear interpolation in each direction).
- `cubic` uses a bicubic interpolation (once again, cubic in each direction).
- `makima` (Modified Akima), uses piecewise Hermite polynomials.
- `spline` interpolation uses cubic splines.

Figure 5.1 depicts the resulting spurious signals due to the interpolation from Cartesian coordinates into cylindrical coordinates. The data is defined to be a perfect $m = 8$ sinusoid sampled along the x and y coordinates defined above. From the figure, we might assume that the cubic splines will always produce the best results, and in a noise-free situation this is true.

Figure 5.2 depicts the same analysis with the inclusion of noise. Here, we can see that all of the continuous methods have similar performance,

[3] In practice, we set N_r and N_θ to be a power of 2, enabling a small speed-up in the FFTs used in the analysis.

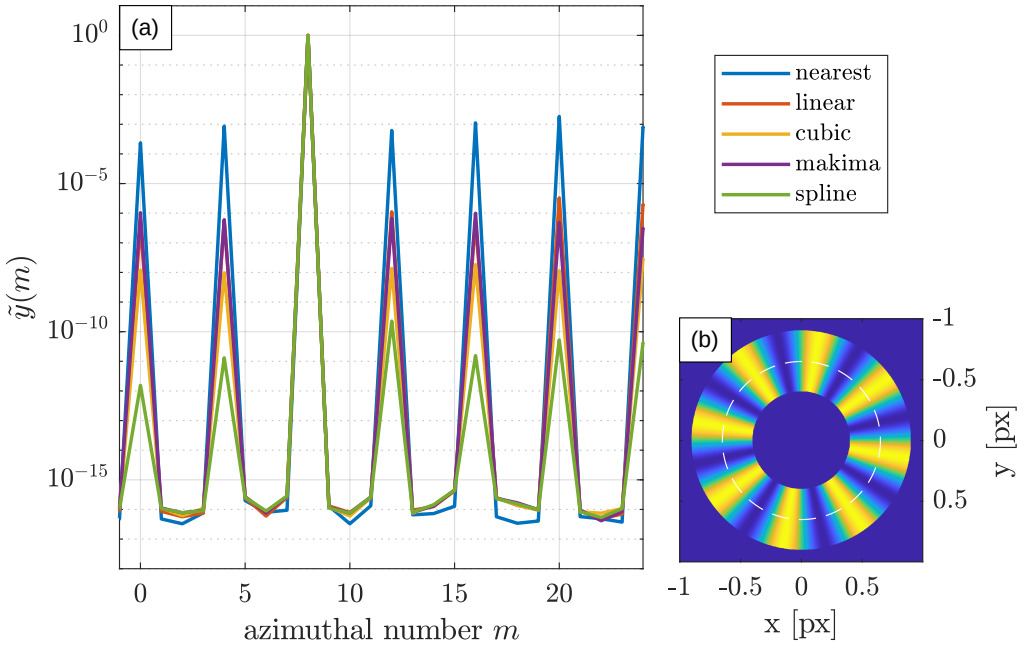

Figure 5.1: Panel (a) depicts the azimuthal Fourier transform of a perfect sinusoid sampled on Cartesian coordinates [Panel (b), sampled at the white dashed line]. The sinusoid has a wavenumber $m = 8$, and though each interpolation method produces the correct amplitude at this signal, spurious signals at varying wavenumbers are created by the coordinate transformation. It is clear that the nearest neighbor scheme produces the least accurate approximation, followed by the linear and modified Akima schemes, then the cubic scheme and finally the cubic splines. Note the scale on the vertical axis. The spurious signals for each of the continuous interpolation schemes is on the order of 10^{-6} times smaller than the actual signal.

though there is a huge discrepancy between the time required for the spline methods and the linear and cubic schemes. Interestingly, it seems that when noise is taken into account, linear interpolation is both the fastest continuous method, and produces the lowest spurious signal.

5.2 Relevant observables, and problems with real-valued data

In section 5.1.1 we briefly touched on the difficulties encountered when working with real-valued data. Within the analogy between QFT in cosmological backgrounds one works with complex mode functions which are described by theoretically well-defined occupation numbers (amplitudes) at all points in time. However in the experiment, the interface waves are measured as real-valued sinusoids. In this section, we will introduce two methods to extract the propagating and counter-propagating amplitudes described previously, namely the Hilbert transform and the wavelet transform. We will provide a motivating example for both, and produce simulated data explaining the benefits of each.

Consider, for example, the case of a solitary pair of propagating/counter-propagating waves, both with time-dependent amplitude $A(t)$. Ignoring the radial component, the observable height field at time t is given by

$$\xi(\theta, t) = A(t)\cos\left(m\theta - \omega_m t + \vartheta_{m,\omega}\right) + A(t)\cos\left(m\theta + \omega_m t + \vartheta_{m,-\omega}\right). \quad (5.17)$$

Two waves moving in opposite directions with the same amplitude sum to a standing wave. To see this, we first redefine the time coordinate, $t \mapsto t + t_0$, so that

$$-\omega_m t_0 + \vartheta_{m,\omega} = \frac{\vartheta}{2}, \qquad \text{and} \quad (5.18)$$

$$\omega_m t_0 + \vartheta_{m,-\omega} = \frac{\vartheta}{2}. \quad (5.19)$$

Further, we redefine the azimuthal coordinate, $\theta \mapsto \theta + \theta_0$, so that $m\theta_0 = -\frac{\vartheta}{2}$.

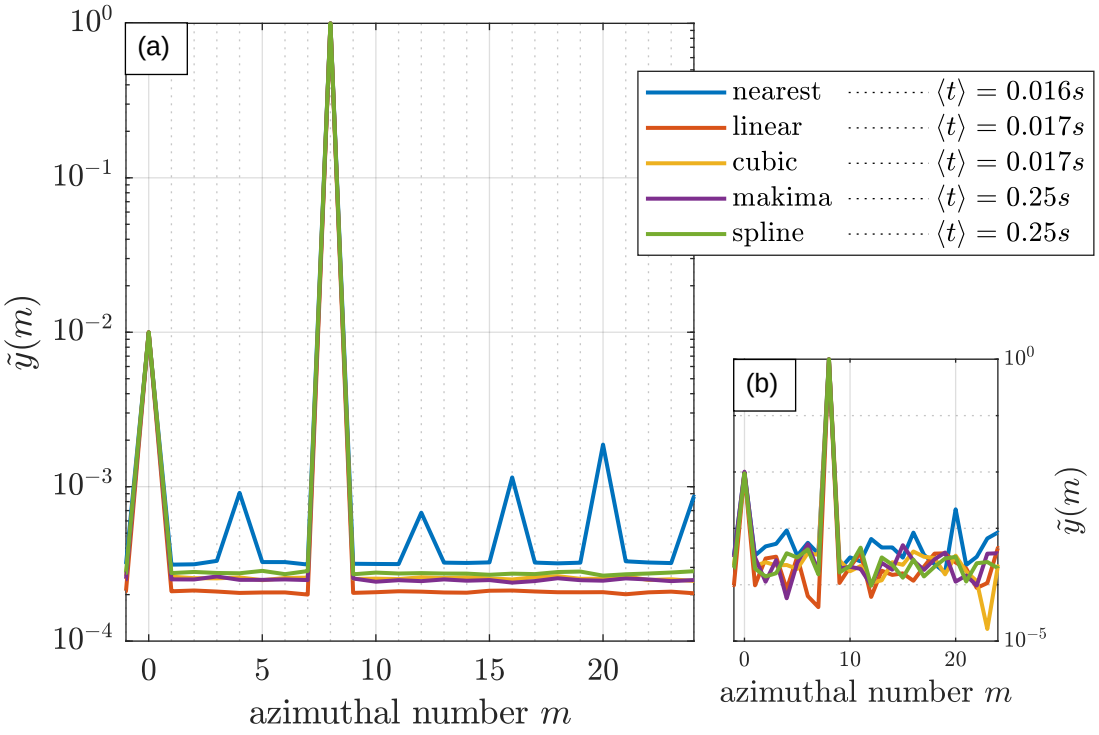

Figure 5.2: Panel (a) depicts the mean spectrum of 1000 interpolated sinusoids with 1% white noise added. The procedure is the same as that used to produce Figure 5.1. Note that the mean spectral amplitude falls below 1% for all of the continuous interpolation methods for all $m > 0$. Interestingly, the $m = 0$ signal seems to be close to 1% for each interpolation scheme. The average time taken to interpolate the data using each method, is listed in the legend.
Panel (b) shows the spectrum for a single data-point, for comparison.

Equation (5.17) simplifies to

$$\begin{aligned}\xi(\theta,t) =& A(t)\cos\left(m\theta-\omega_m t\right)+A(t)\cos\left(m\theta+\omega_m t\right)\\ =& A(t)\big[\cos(m\theta)\cos(\omega_m t)+\sin(m\theta)\sin(\omega_m t)\\ &\qquad +\cos(m\theta)\cos(\omega_m t)-\sin(m\theta)\sin(\omega_m t)\big]\\ =& 2A(t)\cos(m\theta)\cos(\omega_m t).\end{aligned} \tag{5.20}$$

Now, we can start to see the problem with our real observables. If we wish to describe these waves in our system as mode functions, then we will need to know the amplitude $A(t)$ at all times t. However, we have no way to estimate $A(t)$ when $\cos(\omega_m t)$ is not close to the extremal values ± 1. [4]

In order to recover the instantaneous amplitude, the standard practice when working with real signals $s(t)$ is to perform a Hilbert transform, defined as the Cauchy principal value of the integral [94]

$$H[s](t)=\int_{-\infty}^{\infty}\frac{s(t-\tau)}{\pi\tau}\,\mathrm{d}\tau. \tag{5.21}$$

In the simpliest case of $s(t)=a\cos(\omega t)$ (with constant a), it can be shown that $H[s](t)=a\sin(\omega t)$. This allows us to define the analytic extension of $s(t)$ as

$$\begin{aligned}\tilde{s}(t) &= s(t)+iH[s](t)\\ &= a\cos(\omega t)+ia\sin(\omega t)\\ &= a\,\mathrm{e}^{i\omega t}.\end{aligned} \tag{5.22}$$

While for the standing wave described above, Bedrosian's theorem [94] proves that if $A(t)$ varies more slowly than $\cos(\omega_m t)$, and the spectra of $A(t)$ and $\cos(\omega t)$ do not overlap, then

$$H[A(t)\cos(\omega t)]=A(t)\sin(\omega t). \tag{5.23}$$

Thus, we can recover the amplitude $A(t)$ at all times using the analytic extension of ξ:

$$\begin{aligned}\tilde{\xi}(\theta,t) =& \xi(\theta,t)+iH[\xi(\theta,t)]\\ =& 2\cos(m\theta)A(t)\Big[\cos(\omega_m t)+i\sin(\omega_m t)\Big]\\ =& 2A(t)\cos(m\theta)\,\mathrm{e}^{i\omega_m t},\end{aligned} \tag{5.24}$$

[4] One approach in dealing with this issue is to locate the local extrema and then to interpolate between these points to find $A(t)$. However, this approach fails to distinguish between propagating and counter-propagating modes.

since $|\tilde{\xi}(\theta,t)| = 2A(t)\cos(m\theta)$, and the amplitude can be recoverd with an azimuthal FFT.

In the case of time-dependent analogs however, one is often interested in observing rapid changes in the analog metric. For example, if $A(t)$ is an exponentially increasing function (as is the case in parametric resonance) then the spectrum of $A(t)$ drops off as $\frac{1}{f}$ and Bedrosian's theorem does not apply. In the next section, we will examine the efficacy of wavelet analysis when considering this problem.

5.2.1 The Continuous Wavelet Transform

The investigation performs a time-frequency analysis using a Continuous Wavelet Transform (CWT). [5] The CWT used is commonly referred to as the Morlet wavelet, and the implementation used preserves the amplitude of a signal [55]. This type of analysis looks at small time-segments of the data ('windowed' by a normalized Gaussian distribution) and finds the spectral content of these windows of data by comparing them to a complex exponential (see [55] Section 3.1 for a concise motivation of the CWT). This is accomplished by convoluting the signal with a wavelet function $\psi(t)$, here given by

$$\psi_{f_c}(t) = \frac{1}{\sqrt{\pi\sigma}}\, \mathrm{e}^{\frac{-t^2}{\sigma^2}}\, \mathrm{e}^{-i2\pi f_c t}, \tag{5.25}$$

where σ is the standard deviation of the Gaussian envelope, chosen to compliment the central frequency f_c. In practice, choosing $\sigma = \frac{1}{f_c}$ is practical, since this ensures that the envelope allows six full oscillations of the exponential within 99% of its total area.

This type of wavelet transform is particularly suited to the analysis of parametrically amplified waves obeying the linear field theory. We know from the analysis given in section 3.2 that for parametric oscillations with frequency $2\pi f_d \equiv \omega_d$, the growing modes have a fixed frequency equal to πf_d, and that the amplitude is exponential. Thus, an amplified mode in our system will have the form

$$\xi_m(t) = \tilde{b}_m\, \mathrm{e}^{\lambda_m t}\, \mathrm{e}^{-i\pi f_d t} + \tilde{b}^*_{-m}\, \mathrm{e}^{\lambda_m t}\, \mathrm{e}^{i\pi f_d t}\,. \tag{5.26}$$

We can therefore select the central frequency of the wavelet to match the frequency of the growing mode. The resulting convolution is then between

[5] Actually, it is a discrete approximation of a CWT.

a normalized Gaussian and an exponential. The solution of this integral is well known [95]:

$$\int_{\infty}^{\infty} \psi_{\pm\frac{f_d}{2}}(t-\tau)\, \mathrm{e}^{\lambda_m \tau}\, \mathrm{e}^{\pm\pi f_d \tau}\, \mathrm{d}\tau = \mathrm{e}^{\frac{2\lambda_m^2}{f_d^2}}\, \mathrm{e}^{\lambda_m t}\, \mathrm{e}^{\pm i\pi f_d t}, \tag{5.27}$$

where we select either the posive frequency mode, or the negative frequency mode depending on the sign attached to the central frequency of the wavelet. Keeping in line with the notation used above, we can define our time-dependent amplitude functions,

$$d_m(t) = b_m\, \mathrm{e}^{\frac{2\lambda_m^2}{f_d^2}}\, \mathrm{e}^{\lambda_m t}, \tag{5.28}$$

$$d^*_{-m}(t) = b^*_{-m}\, \mathrm{e}^{\frac{2\lambda_m^2}{f_d^2}}\, \mathrm{e}^{\lambda_m t}\,. \tag{5.29}$$

This approximation is valid away from sharp transitions in amplitude behavior. In particular, due to our choice of $\sigma = \frac{1}{f_c}$ with our wavelet, we have a 99% confidence in our results after three oscillations of our growing mode (in Chapter 6, we will see that this corresponds to roughly 1s).

We can thus approximate the instantaneous amplitude for an exponentially changing amplitude to within a multiplicative factor, $\exp\left(\frac{2\lambda_m^2}{f_d^2}\right)$, which is of order 1 when λ_m is much smaller than the driving frequency f_d. Further, by taking the logarithm of the amplitude, we can separate this known factor from the exponential amplification rate,

$$\log|d_m(t)| = \lambda_m t + \frac{2\lambda_m^2}{f_d^2} + |b_m| \simeq \lambda_m t + |\tilde{b}_m|. \tag{5.30}$$

Likewise, when the shaker is switched off, we expect to have exponentially decaying waves according to equation (3.29). Writing the exponential decay rate as γ_m, [6] we have

$$\log|d_m(t > t_{\mathrm{stop}})| = \gamma_m t + \frac{2\gamma_m^2}{f_d^2} + |b_{\mathrm{stop}}|, \tag{5.31}$$

where in this case, the constant b_{stop} represents the amplitude of the mode function after shaking has ceased.

[6] This slight abuse of notation also serves to differentiate between the experimental dissipation rate and the theoretical dissipation rate γ_k.

We can therefore see that during a period of exponential growth, we are able to extract the exponential growth rate, as well as an estimation of the initial amplitude $|b_m|$. Likewise, during a period of exponential decay we are able to extract the decay rate γ_m, and further, the exponential rates will not be subject to approximation errors from the continuous wavelet analysis.

Using equation (5.7) as a starting point for our analysis, we see that for a given height field $\xi(\theta, t)$, the azimuthal FFT amplitude for the $+m$ mode gives

$$\xi_m = d_m(t)\, \mathrm{e}^{-i\omega_m t} + d^*_{-m}(t)\, \mathrm{e}^{i\omega_m t}, \tag{5.32}$$

and the output of the positive and negative frequency wavelet analysis will therefore be

$$d_m \simeq b_m\, \mathrm{e}^{\lambda_m t}\, \mathrm{e}^{-i\omega_m t}, \qquad \text{and} \tag{5.33}$$

$$d^*_{-m} \simeq b^*_{-m}\, \mathrm{e}^{\lambda_m t}\, \mathrm{e}^{i\omega_m t}, \tag{5.34}$$

enabling us to proceed with the analysis presented in Chapter 2.

5.3 Free Field Theory Analysis

In this section, we will introduce the Bogolyubov transformation for our analog mode functions. Following this, we will develop the idea of classical mode squeezing and we will demonstrate that this phenomenon is observable even in the presense of dissipation.

5.3.1 Mode statistics: Classical squeezing in the non-dissipative theory

We will define classical squeezing in an analogous way to quantum squeezing. In quantum squeezing the variance of an observable (position for example) is 'squeezed' below its vacuum expectation value, at the expense of the variance of its conjugate momentum. The increase in one variance is necessary due to the Heisenburg uncertainty limit, such that the product of the variances remains constant.

While a full description of quantum squeezing is outside the scope of this thesis, the author recommends [96] for additional information. In our system, we will define squeezing to be such that the variance of an observable will drop below the variance in the initial state [50].

In this section, we will provide some motivation and formalism regarding the Wronskian of the field ξ_m. This will be followed by a presentation of the Bogolyubov transformation for the system, and a field theoretic description of the amplification and creation of counter-propagating modes.

In Chapter 2, we introduced an auxilliary field, defined in order to eliminate the first derivative term (corresponding to damping in this case) from the equation of motion in question. Beginning with the equation of motion for our field ξ_m,

$$\ddot{\xi}_m + 2\gamma_m \dot{\xi}_m + \omega_m^2 \xi_m = 0, \tag{5.35}$$

where we have rewritten equation (3.29) to use the subscript m. We make the following coordinate change:

$$\chi_m = \mathrm{e}^{\gamma_m t}\, \xi_m. \tag{5.36}$$

We can rewrite the equation of motion as

$$\chi_m'' + \Omega_m(t)\chi_m = 0, \tag{5.37}$$

where the frequency Ω_m is given by

$$\Omega_m = \omega_k^2(t) - \gamma_m^2. \tag{5.38}$$

Since equation (5.37) is a second order differential equation, we can span the space of solutions with two linearly independent functions. In the most general case, if x_m and y_m are two linearly independent solutions to (5.37), then $u_m = x_m + iy_m$ is a complex solution, and $\{u_m, u_m^*\}$ form a basis for all complex solutions [56].

Keeping equation (5.7) in mind, we see that the mode functions u_m and u_m^* can be viewed as waves moving with opposite momenta, allowing us to write χ_m as a superposition of counter-propagating waves:

$$\chi_m = b_m u_m + b_{-m}^* u_m^*. \tag{5.39}$$

These functions are generally normalized using the Wronskian, [7] defined as

$$\mathrm{Wr}(u_m, u_m^*) = \dot{u}_m u_m^* - u_m \dot{u}_m^*. \tag{5.40}$$

[7] If we wish to quantize our theory, we may do so at this point by mapping $b_{\pm m} \mapsto \hat{b}_{\pm m}$, and requiring the operators to satisfy the usual bosonic commutation relations,

$$\left[\hat{b}_{\pm m}, \hat{b}_{\pm k'}^\dagger\right] = \delta(k - k')$$
$$\left[\hat{b}_{\pm m}, \hat{b}_{\pm k'}\right] = \left[\hat{b}_{\pm m}^\dagger, \hat{b}_{\pm k'}^\dagger\right] = 0,$$

and normalizing the mode function as above [56].

Taking the derivative of Wr, we have

$$\dot{\mathrm{Wr}} = \ddot{u}_m u_m^* + \dot{u}_m \dot{u}_m^* - \dot{u}_m \dot{u}_m^* - u_m \ddot{u}_m^*. \tag{5.41}$$

Cancelling terms, and adding $\Omega_m^2 u_m u_m^* - \Omega_m^2 u_m u_m^*$, we have

$$\dot{\mathrm{Wr}} = \left(\ddot{u}_m + \Omega_m^2 u_m\right) u_m^* - \left(\ddot{u}_m^* + \Omega_m^2 u_m^*\right) u_m, \tag{5.42}$$

which is zero by equation (5.37), implying that the Wronskian is conserved.

Normalizing the functions χ_m so that $\mathrm{Wr}(u_m, u_m^*) = 2i$ allows for the definition of the usual ladder operators and commutation relations associated with $b_{\pm m}$ in a quantum field theory [56].

Translational symmetry of the equations of motion imply that momentum is conserved in this system. However, changing the frequency Ω_m changes the energy of the field χ_m. As energy is added or removed from the system, the momentum of the field is compensated via the creation of counter-propagating waves. This can be seen from the following example.

Consider a monochromatic propagating wave, initially in flat space, that is completely described by a single plane wave $\chi_m = b_m u_m \, \mathrm{e}^{ik\cdot\vec{x}}$, where $u_m = \mathrm{e}^{-i\Omega_m^{(i)} t}$ for all time $t < 0$ (region 1). At $t = 0$, the spacetime undergoes some expansion (region 2), before once again becoming static for all $t > t_f$ (region 3). Since the equation of motion is second order and the solutions in region 3 are plane waves ($\{v_m, v_m^*\}$ say), we know that after the expansion the mode u_m is some superposition of v_m and v_m^*:

$$u_m = \alpha_m v_m + \beta_m v_m^*. \tag{5.43}$$

It is easy to show using equations (5.40) and (5.43) that so long as the mode functions are normalized in the same way, we will have

$$\left(|\alpha_m|^2 - |\beta_m|^2\right) \mathrm{Wr}(v_m, v_m^*) = \mathrm{Wr}(u_m, u_m *), \tag{5.44}$$

$$\implies |\alpha_m|^2 - |\beta_m|^2 = 1. \tag{5.45}$$

Thus we see that equation (5.43) describes a Bogolyubov transformation [97, 40], familiar from quantum field theory in curved spacetimes.

In particular, if the system in question is undergoing parametric amplification, we can rewrite the Bogolyubov coefficients in terms of the amplification rates predicted by the Floquet theory (equation (3.39)):

$$\alpha_m = \cosh(\eta_m t), \tag{5.46}$$

$$\beta_m = \sinh(\eta_m t). \tag{5.47}$$

This satisfies equation (5.45) trivially, and helps with intuitive understanding of the system.

If our solitary propagating wave χ_m is undergoing parametric amplification, then initially $\alpha_m = 1$ and $\beta_m = 0$. As amplification progresses, counter-propagating waves (corresponding to $\beta_m v_m^*$) will be produced as the propagating waves are amplified (this must occur since momentum is conserved).

After several cycles, the difference between the propagating and counter-propagating amplitudes is $\mathrm{e}^{-\eta_m t}$. On the other hand, equation (5.44) implies that the energy of the propagating mode grows along with the energy of the counter-propagating mode. Observationally this means that even if the system starts out with a solitary propagating wave χ_m, the creation of counter-propagating modes implies that the system will tend towards a standing wave. However in what follows, we will show that it is equation (5.44) which gives meaning to the interpretation provided by classical squeezing.

5.3.2 Classical squeezing for the auxilliary field

In general, the Bogolyubov transformation can be considered a change of basis from $\{u_m, u_m^*\}$ to $\{v_m, v_m^*\}$, and for any arbitrary expansion [57], we have

$$\begin{aligned} \chi_m &= b_m u_m + b_{-m}^* u_m^* && (5.48)\\ &\mapsto b_m \left(\alpha_m v_m + \beta_m v_m^*\right) + b_{-m}^* \left(\alpha_m^* v_m^* + \beta_m^* v_m\right) && (5.49)\\ &= d_m v_m + d_{-m}^* v_m^*. && (5.50) \end{aligned}$$

Collecting terms, we see that the mode function amplitudes after expansion are given by [8]

$$d_m = \alpha_m b_m + \beta_m^* b_{-m}^*. \tag{5.51}$$

This quantity is often investigated as the two-point auto-correlation over a large number of measurements:

$$\left\langle d_m d_m^* \right\rangle = \left\langle |d_m|^2 \right\rangle = \left(|\alpha_m|^2 + |\beta_m|^2\right) \left\langle |b_m|^2 \right\rangle, \tag{5.52}$$

where we have used the fact that $\alpha_m = \alpha_{-m}$, $\beta_m = \beta_{-m}$, and $\langle |b_m|^2 \rangle = \langle |b_{-m}|^2 \rangle$ due to symmetry in the equation of motion, and the fact that the

[8] Note that the observables $d_m v_m$ and $d_{-m}^* v_m^*$ correspond to the output of the wavelet transform for the positive and negative frequency wavelets respectively.

uniformly distributed azimuthal phase ensures that $\langle b_{\pm m}^2 \rangle = \langle b_m b_{-m} \rangle = \langle b_m b_{-m}^* \rangle = 0$. Similarly, we find that modes propagating in opposite direction are now cross-correlated:

$$\langle d_m d_{-m} \rangle = 2\alpha_m \beta_m^* \left\langle |b_m|^2 \right\rangle . \tag{5.53}$$

Note that by construction (under the assumptions of axisymmetry and linearity), all other $m - m'$ correlations are zero.

The amplification and cross-correlation manifest themselves in the system as 2-mode squeezing. If we define the real observable $X_m = d_m v_m + d_m^* v_m^*$, then we can examine the quadrature variables $(X_m + X_{-m})$ and $(X_m - X_{-m})$. We compute the variance of both quantities:

$$\begin{aligned} \mathrm{Var}\left(X_m \pm X_{-m}\right) &= \langle (X_m \pm X_{-m})^2 \rangle \\ &= 4 \left\langle |b_m|^2 \right\rangle \left\{ \left(|\alpha_m|^2 + |\beta_m|^2 \right) |v_m|^2 \pm 2\mathrm{Re}\left(\alpha_m \beta_m^* v_m^2 \right) \right\} . \end{aligned} \tag{5.54}$$

If the mode functions v_m are normalized to 1, [9] and we choose t such that $\mathrm{Re}\left(\alpha_m \beta_m^* v_m^2\right)$ is maximized, then we find that $\mathrm{Var}\left(X_m - X_{-m}\right)$ is squeezed below its initial state, while $\mathrm{Var}\left(X_m + X_{-m}\right)$ is increased. However, it is easy to show algebraically that the product $\mathrm{Var}\left(X_m - X_{-m}\right) \mathrm{Var}\left(X_m + X_{-m}\right)$ remains constant when $\mathrm{Re}(\alpha_m \beta_m^* v_m^2) = |\alpha_m \beta_m^* v_m^2|$:

$$\begin{aligned} &\frac{1}{16 \left\langle |b_m|^2 \right\rangle^2} \mathrm{Var}\left(X_m + X_{-m}\right) \mathrm{Var}\left(X_m - X_{-m}\right) \\ &\quad = \left\{ \left(|\alpha_m|^2 + |\beta_m|^2 \right) + 2|\alpha_m||\beta_m| \right\} \left\{ \left(|\alpha_m|^2 + |\beta_m|^2 \right) - 2|\alpha_m||\beta_m| \right\} \\ &\qquad = \left(|\alpha_m|^2 + |\beta_m|^2 \right) - 4|\alpha_m|^2 |\beta_m|^2 \\ &\qquad\qquad = \left(|\alpha_m|^2 - |\beta_m|^2 \right)^2 = 1. \end{aligned} \tag{5.55}$$

This is the classical analog of quantum squeezing. In the quantum picture, one observable is squeezed below the quantum uncertainty limit while its conjugate variable increases accordingly in order to preserve the uncertainty principle [96]. In our classical analog, we find from equation (5.54) that as $2|\alpha_m||\beta_m| \longrightarrow |\alpha_m|^2 + |\beta_m|^2$, the oscillating cross-correlation term will cause $X_m + X_{-m}$ to alternate between 0 and $2\left(|\alpha_m|^2 + |\beta_m|^2\right)$. Intuitively,

[9] Since we are not quantizing our fields, we need not follow the convention of normalizing the mode functions using the Wronskian.

this corresponds to different moments in time for a standing wave. When $X_m + X_{-m}$ is maximized, the standing wave is at its zenith, and all of the energy of the mode is stored as potential. When $X_m + X_{-m}$ is zero, the free-surface is flat, and all of the energy is kinetic.

Mathematically, we can use the forms for α_m and β_m predicted by the Floquet theory. We define

$$\begin{aligned} N_m &\equiv 4\left\langle |b_m|^2 \right\rangle \left(\alpha_m^2 + \beta_m^2\right) \\ &= 4\left\langle |b_m|^2 \right\rangle \left(\cosh(\eta_m t)^2 + \sinh(\eta_m t)^2\right) \\ &= 4\left\langle |b_m|^2 \right\rangle \cosh(2\eta_m t), \end{aligned} \tag{5.56}$$

and

$$\begin{aligned} c_m &\equiv 4\left\langle |b_m|^2 \right\rangle 2\alpha_m\beta_m v_m^2 \\ &= 4\left\langle |b_m|^2 \right\rangle 2\cosh(\eta_m t)\sinh(\eta_m t) v_m^2 \\ &= 4\left\langle |b_m|^2 \right\rangle \sinh(2\eta_m t) v_m^2 \end{aligned} \tag{5.57}$$

from equation (5.55). This allows us to predict the shape of the distributions for $X_m + X_{-m}$ and $X_m - X_{-m}$ when $\mathrm{Re}(c_m) = |c_m|$:

$$N_m + |c_m| = 4\left\langle |b_m|^2 \right\rangle \mathrm{e}^{2\eta_m t}, \tag{5.58}$$

and

$$N_m - |c_m| = 4\left\langle |b_m|^2 \right\rangle \mathrm{e}^{-2\eta_m t}\,. \tag{5.59}$$

Additionally, we shall see in section 5.3.3 that these variables also provide a useful measure of the degree of decoherence in the system.

5.3.3 The Wronskian for the field ξ_m

In the above calculations, the constant value of $\mathrm{Wr}(u_m, u_m^*)$ is a result of equation (5.37). When considering the Wronskian and the field ξ_m, we must use instead equation (5.35). In this case, we find that equation (5.42) becomes

$$\partial_t \,\mathrm{Wr} = \left(\ddot{u}_m + \omega_m^2 u_m\right) u_m^* - \left(\ddot{u}_m^* + \omega_m^2 u_m^*\right) u_m \tag{5.60}$$

$$= -2\gamma_m \left(\dot{u}_m u_m^* - u_m \dot{u}_m^*\right) \tag{5.61}$$

$$= -2\gamma_m \,\mathrm{Wr}\,. \tag{5.62}$$

Thus, we find that the Wronskian is no longer conserved, and for a damped field described by equation (5.35), we have

$$\mathrm{Wr}(u_m, u_m^*) = \mathrm{Wr}_i \, \mathrm{e}^{-2\gamma_m t}, \tag{5.63}$$

where Wr_i is some initial value, defined by equation (5.40) and the initial mode functions $\{u_m, u_m^*\}$.

If we assume an initial (static) spacetime with a constant Wronskian for the mode functions $\{u_m, u_m^*\}$, and we define the Bogolyubov coefficients for the instantaneous mode functions $\{v_m, v_m^*\}$, then we will find that

$$|\alpha_m|^2 - |\beta_m|^2 = \mathrm{e}^{-2\gamma_m t} \, . \tag{5.64}$$

This, together with the definition of the auxilliary field suggests that

$$\alpha_m = \mathrm{e}^{-\gamma_m t} \cosh(\eta_m t), \tag{5.65}$$
$$\beta_m = \mathrm{e}^{-\gamma_m t} \sinh(\eta_m t). \tag{5.66}$$

Repeating the same calculations for the quadratures X_m and X_{-m}, we find the product in equation (5.55) is no longer constant. With linear damping, the same calculation gives

$$\mathrm{Var}\,(X_m + X_{-m}) \, \mathrm{Var}\,(X_m - X_{-m}) \tag{5.67}$$
$$= 16 \left\langle |b_m|^2 \right\rangle^2 \left(|\alpha_m|^2 - |\beta_m|^2 \right)^2 \tag{5.68}$$
$$= \mathrm{e}^{-4\gamma_m t} \, 16 \left\langle |b_m|^2 \right\rangle^2, \tag{5.69}$$

and we can see that the interpretation given for the auxilliary field is no longer valid.

Keeping the definition of the auxilliary field in mind, it would be convenient to simply redefine the quadratures in the same manner as equation (5.36). Unfortunately, in practice this leads to very large amplitudes, and fails to produce the predicted results. Trying another tactic, we define:

$$\Delta_m^4 = \mathrm{Var}\,(X_m + X_{-m}) \, \mathrm{Var}\,(X_m - X_{-m}) \tag{5.70}$$
$$= \mathrm{e}^{-4\gamma_m t} \, 16 \left\langle |b_m|^2 \right\rangle^2, \tag{5.71}$$

as well as the new quadratures

$$Y_m = \frac{1}{\Delta_m} X_m \tag{5.72}$$

$$= \frac{\mathrm{e}^{\gamma_m t}}{2\sqrt{\langle |b_m|^2 \rangle}} \left(d_m v_m + d_m^* v_m^* \right), \tag{5.73}$$

$$\equiv \left(\tilde{d}_m v_m + \tilde{d}_m^* v_m^* \right). \tag{5.74}$$

Where the new amplitudes $\tilde{d}_{\pm m}$ are theoretically consistent with the auxilliary amplitudes defined in equation (5.51).

The advantages of defining the normalization in this manner are two-fold. First, the product of the variances

$$\mathrm{Var}\left(Y_m + Y_{-m}\right) \mathrm{Var}\left(Y_m - Y_{-m}\right) = 1 \tag{5.75}$$

is trivially conserved. Second, Δ_m provides a statistically accessible and consistent way of eliminating the exponential factor from the quadratures $X_{\pm m}$, ensuring that the normalized Bogolyubov coefficients match the theoretical coefficients for the auxilliary field which obey equation (5.45). This further implies that the squeezing should be characterized by equations (5.58) and (5.59).

A note regarding the observed product of variances

It should be mentioned that in data *as well as in linear ODE simulations*, we have not observed an exponential decay in equation (5.67). It is currently believed that this is due to imperfect statistics. Taking the unnormalized values N_m and c_m defined in (5.56) and (5.57) respectively, the theory produces the following result:

$$\lim_{t\to\infty} \frac{|c_m|}{N_m} = 1. \tag{5.76}$$

In practice, the time-dependent v_m^2 term in the definition of c_m produces inconsistencies due to the precision of finite timesteps in real-world measurements and synchronization between experimental runs. For N_{runs} experiments (or simulations), we will have that

$$\lim_{t\to\infty} 1 - \frac{|c_m|}{N_m} \equiv \epsilon_m \propto \frac{1}{N_{\text{runs}}}. \tag{5.77}$$

Using the Floquet predictions for the Bogolyubov coefficients as defined in (5.65), and redefining the observable c_m so that

$$c_m \equiv 4\left\langle |b_m|^2 \right\rangle (1-\epsilon_m)\sinh(2\eta_m t)v_m^2, \tag{5.78}$$

we see that the product of variances is likewise modified:

$$\begin{aligned}\frac{1}{4\left\langle |b_m|^2\right\rangle}\left(N_m^2 - |c_m|^2\right) & \\ = \mathrm{e}^{-4\gamma_m t} + \mathrm{e}^{-4\gamma_m t}\left(2\epsilon_m - \epsilon_m^2\right)\sinh^2(2\eta_m t) & \\ \simeq \mathrm{e}^{-4\gamma_m t} + 2\epsilon_m \mathrm{e}^{(4\eta_m - 4\gamma_m)t}\,. & \end{aligned} \tag{5.79}$$

The above suggests that for *any* finite number of experiments, the product of variances given in equation (5.55) will be observed to increase exponentially (even when $\gamma_m = 0$) when t is large enough that

$$2\epsilon_m \mathrm{e}^{4\eta_m t} > 1. \tag{5.80}$$

These results coincide and expand upon statements regarding quantum squeezing [98]. Specifically, "Pure Platonic Squeezing" is an idealized concept (arising from the Platonic ideal for a given experiment), and some form of decoherence is always present. The parameter ϵ_m is equivalent to the parametrization of the level of decoherence, δ_k defined in [99]. In this study, the authors consider temporal decoherence due to weak nonlinearities in an interacting quantum system. To this author's knowledge, decoherence arising from imperfect synchronization of continuous measurements (not possible in quantum experiments) and statistics in a perfectly linear system has not yet been considered.

Chapter 6

Results

In this chapter, we will present the results of the experiments detailed in Chapter 4. The first section will demonstrate the methodology used to extract the amplification and damping rates, as well as the extrapolated initial amplitude for a single experimental run. We will then present the results for the full set of experiments.

In the second section, we will present the field theoretic results for the squeezing that was presented in section 5.3.3. These will be compared with data simulated using a linear ODE as discussed in section 3.5.

6.1 Fluid Physics Results

In this section, the measured parametric amplification rates, extrapolated initial amplitudes, and exponential damping rates will be shown. We will first outline some experimental parameters for the data set. We will then present a step-by-step analysis of the quantities listed above for a single experimental run. Finally, we will present the full results of the experiment, and discuss the accuracy that has been acheived.

6.1.1 Experimental Parameters

In this section, the repeatability and consistency of experimental parameters across the full data set will be demonstrated. The results that follow pertain to 1500 experimental runs. The first data point was taken at approximately 17:00 on July 23$^{\text{rd}}$ 2021, and the full dataset took approximately 50 hours

to complete. The approximate 2 minute duration of each experimental run included roughly 25s of shaking, and 75s of downloading and data storage. As can be seen in what follows, the damping rate measured in each experiment is more than double the amplification rate. By this estimation, there was more than sufficient time to allow the system to return to its initial state between experimental runs (ensuring that consecutive experiments are uncorrelated). The full experiment was conducted over the weekend in a dark-room in order to minimize both mechanical and optical noise in the measurements.

In Figure 6.1, panel a) we see accelerometer and temperature data for all 1500 experiments. The acceleration of the shaker is defined as the Fourier amplitude $\tilde{a}_z \equiv \tilde{a}_z(f_d)$, where f_d is the frequency of the shaker's oscillations. [1] From the figure, we can see that the amplitude of the shaker's oscillations drifts slightly as time passes. In particular, we see a significant change beginning at roughly 11:00 on the 24th of July, and another at roughly the same time on the 25th. From the temperature data, we can postulate that these changes result from sharp increases in ambient temperature starting in mid-morning on a summer day. Presented as $\mu \pm \sigma$ (the mean plus or minus the standard deviation), we have the shaker amplitude (corresponding to $\tilde{\epsilon}$ defined in equation (3.38)):

$$\tilde{a}_z(f_d) = 3.458 \pm 0.025 \text{ms}^{-2}. \tag{6.1}$$

It is currently believed that the observed anti-correlation between the shaker amplitude and temperature is due to shifts in the natural frequency of the spring-mass system. The origin of this believe stems from the trial-and-error method by which we set the shaker frequency (see section 4.1): On a particularly hot day in the summer, this procedure was conducted as we entered the laboratory, and *before* the air-conditioner had been started. In the afternoon of that day, it was discovered that the shaker amplitude had dropped with the ambient temperature, and the above procedure was conducted again resulting in a new peak amplitude.

Panel b) shows information detailing how well the experiment matches the theoretical assumptions about the shaker's oscillations. The left-hand axis depicts the ratio of the magnitude of the radial accelleration and the vertical acceleration at the driving frequencies (see Appendix B, equation (B.5) for more details). The right-hand axis displays the total harmonic distortion

[1] Specifically, we use twice the Fourier amplitude at f_d, since half of the energy in the signal is at $-f_d$.

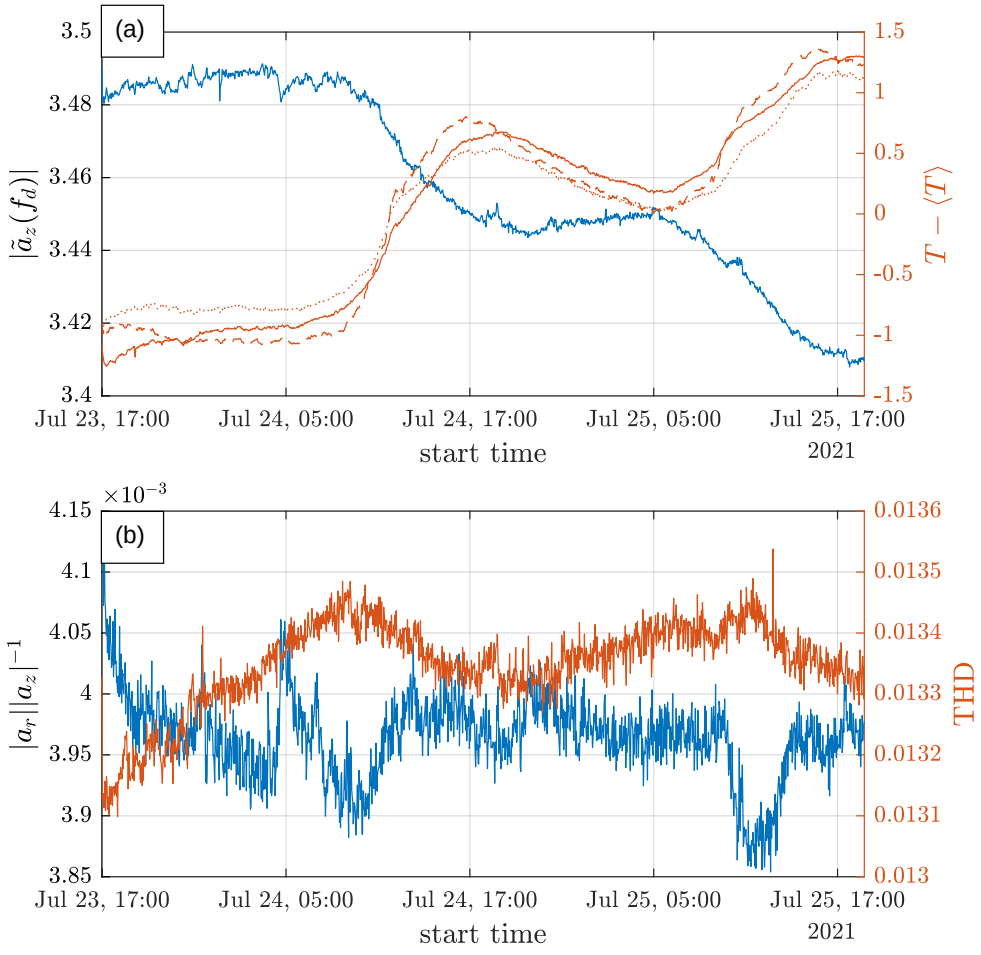

Figure 6.1: In panel a), the left-hand vertical axis depicts the Fourier amplitude from the accelerometer for each experimental number. The right-hand axis shows the change in temperature for the three separate thermometers used. It can be seen that during periods of stable temperature, the shaker amplitude is quite constant. The non-uniformity in the accelerometer data suggests that the sharp increase in the temperature during the summer morning and early afternoon was most influential.
In panel b), the left-hand axis shows the relative horizontal acceleration at the driving frequency. It should be noted that for each experiment, the horizontal acceleration is less than 0.5%. The right-hand axis depicts the total harmonic distortion (THD). This value is maintained below 1.5% for each experiment.

(THD), which is a measure of how much the shaker deviates from a pure sinusoid in its oscillations. The THD quantity in the figure is calculated as:

$$\text{THD} = \frac{\sqrt{\sum_{n=2}^{20} \tilde{a}_z(nf_d)}}{\tilde{a}_z(f_d)}, \tag{6.2}$$

where $\tilde{a}_z(nf_d)$ indicates the nth harmonic of the driving frequency f_d.

If more precision in the shaker is required, there are two suggested fixes regarding the previous conjectures: First, the experiment could be thermally buffered from the surrounding room. Attempts were made to control the temperature using an air-conditioner, however the air-conditioner installed operated on a 10 minute duty cycle, and this cycle was very noticable in the data collected. A buffer, consisting of an inner and outer box may smooth these variations. The second suggestion is perhaps more robust. Transient signal analysis (available in many introductory textbooks, see [69] for example) informs us that a driven damped harmonic oscillator will have a broader resonance peak if the damping and driving force are both increased. This implies that if the natural frequency of the system shifts slightly due to environmental conditions, there will not be such a sharp decrease in the steady-state amplitude of the spring-mass system.

In Figure 6.2, we see the same accelerometer data presented as a relative deviation from the mean amplitude,

$$Q = \frac{\tilde{a}_z - \langle \tilde{a}_z \rangle}{\langle \tilde{a}_z \rangle}. \tag{6.3}$$

This is presented for the full data set in panel a), and for subsets S_1 (containing 561 experimental runs), and S_2 (containing 532 experimental runs) in panel b). In order to obtain the subsets, the Matlab function `findchangepts` was used to separate the shaker amplitude into contiguous samples with a similar root mean square in the relative deviation. Written as above, with a superscript indicating the set number, we have

$$\tilde{a}_z^{(1)}(f_d) = 3.486 \pm 0.003\text{m}, \tag{6.4}$$

and

$$\tilde{a}_z^{(2)}(f_d) = 3.448 \pm 0.003\text{m}. \tag{6.5}$$

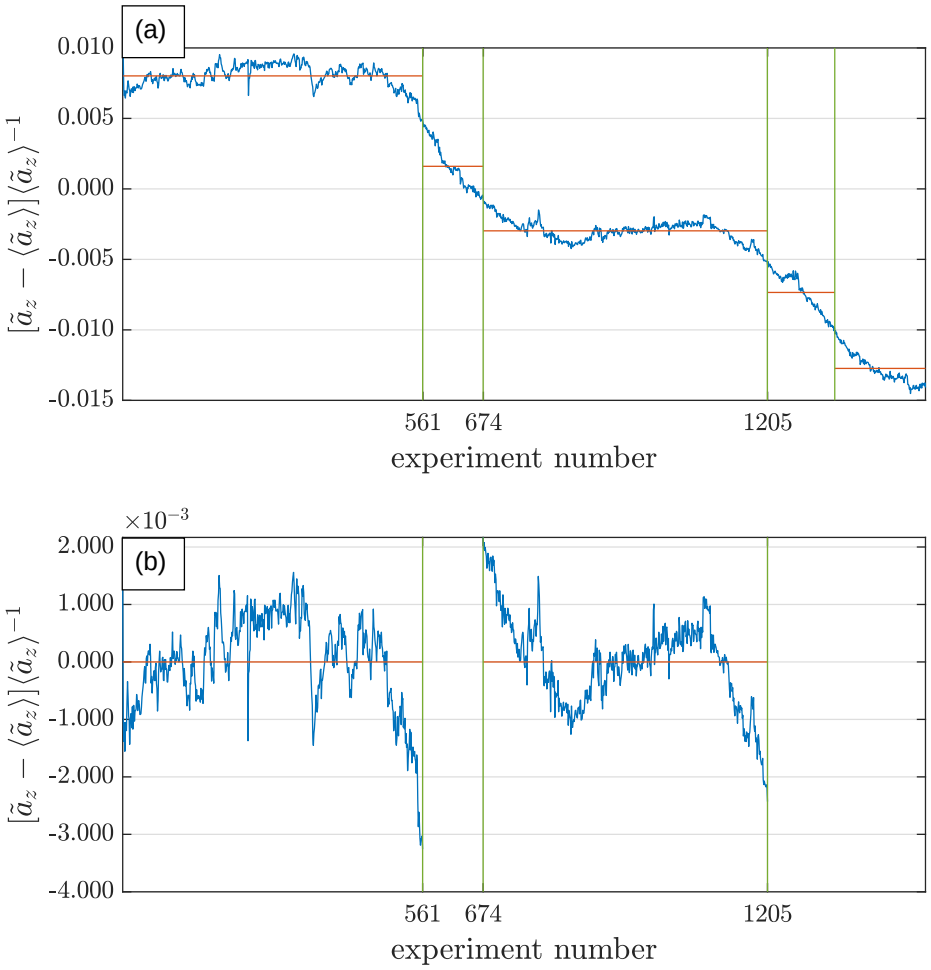

Figure 6.2: Panel a) depicts the relative deviation of the shaker amplitude and the mean versus experiment number, with regions of stability bounded by the vertical lines. We can see that for all 1500 experiments, we are within $+1\%$ and -1.5% of the mean amplitude, $\langle 2|\tilde{a}_z|\rangle = 3.46\text{ms}^{-2}$.
In panel b) we see that for the subsets S_1 and S_2, this deviation is considerably reduced, and we are within $+0.2\%$ and -0.4% of the mean for each subset. Letting the subscript denote the set number, we have $\langle 2|\tilde{a}_z|\rangle_1 = 3.49\text{ms}^{-2}$, and $\langle 2|\tilde{a}_z|\rangle_2 = 3.45\text{ms}^{-2}$.

6.1.2 Interface wave results

In this section, we will first present the results of the interface wave analysis regarding the exponential growth and decay rates, and the approximation of the initial amplitude for the interface waves. This will be followed by a presentation of a subset of data points which does not display the behavior expected from the linear theory.

In Figure 6.3, we see the progression from reconstructed height field to the time-evolution of a single azimuthal mode. The (2+1)-dimensional data is reduced to (1+1) dimensions by considering a single radius in isolation. In panel a), we see a time-slice corresponding to t_{stop} (the moment that the shaker-driver is switched off) for experiment number 36. Note that we seem to be examining an $m = 4$ mode with one radial zero crossing (see section 5.1.1). The isolated radius is emphasized by the horizontal dashed lines, and corresponds to 22.4mm (chosen to maximise the signal to noise-ratio). In what follows, we will consider the $m = 4$ mode at the radius pictured for each of the experimental runs.

Panel b) displays the time-evolution of all of the azimuthal modes at the selected radius. It is clear from this figure that for all time-steps, the $m = 4$ mode carries the strongest signal. In panel c), we see the time-evolution of the $m = 4$ mode. In this figure, we can clearly see a period of exponentially increasing amplitude prior to t_{stop} followed by a damping period after the shaker-driver is switched off.

Figure 6.4, panel a) demonstrates the Morlet wavelet analysis presented in section 5.2.1. In it, we see that at $\frac{f_d}{2} = 3.035$Hz, a signal becomes aparent at roughly 12s, and grows to dominate the signals at all frequencies. In section 5.2.1 we saw that the output of the wavelet transform was the complex amplitude,

$$d_m \simeq b_m \, \mathrm{e}^{\lambda_m t} \, \mathrm{e}^{-i\omega_m t} \, . \tag{6.6}$$

Since this quantity is complex, we have access to the instantaneous amplitude of the mode, which is plotted in panel b). Panel b) also demonstrates how the initial amplitude can be approximated, and how the exponential amplification rate for the mode, as well as the exponential damping rate are extracted from the log amplitudes. This same analysis was automated, and the quantities above were extracted for all 1500 experimental runs.

In Figure 6.5, we see the resulting analysis for the entire (time-synchronized) experimental set. In panel a), we see that there are actually four distinct regions in the data. In region 1, we do not have enough resolution in the

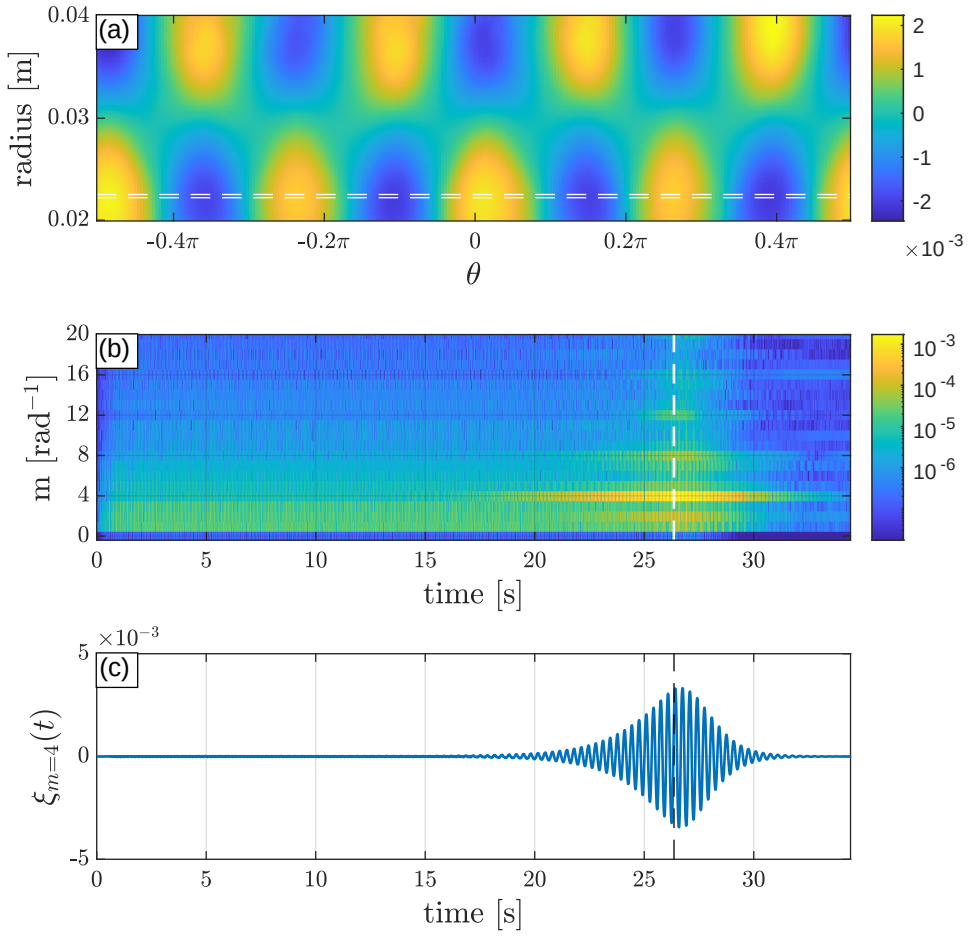

Figure 6.3: In panel a), we see a single timeframe of the reconstructed height field. The data is from experiment number 36, at the timestep closest to the stop-time of the shaker, $t_{\text{stop}} = 26.36$s. The horizontal white lines outline the selected radius, $I_r = 16$, for the data analysis.
Panel b) depicts the azimuthal Fourier decomposition for the selected radius for all time-steps. From this plot, we can see that the $m = 4$ mode presents the strongest signal. The vertical white line indicates t_{stop}.
Panel c) depicts the $m = 4$ mode versus time. The black vertical dashed line indicates t_{stop}. Note the exponential increase in amplitude starting at roughly 15s, followed by the exponential damping after t_{stop}.

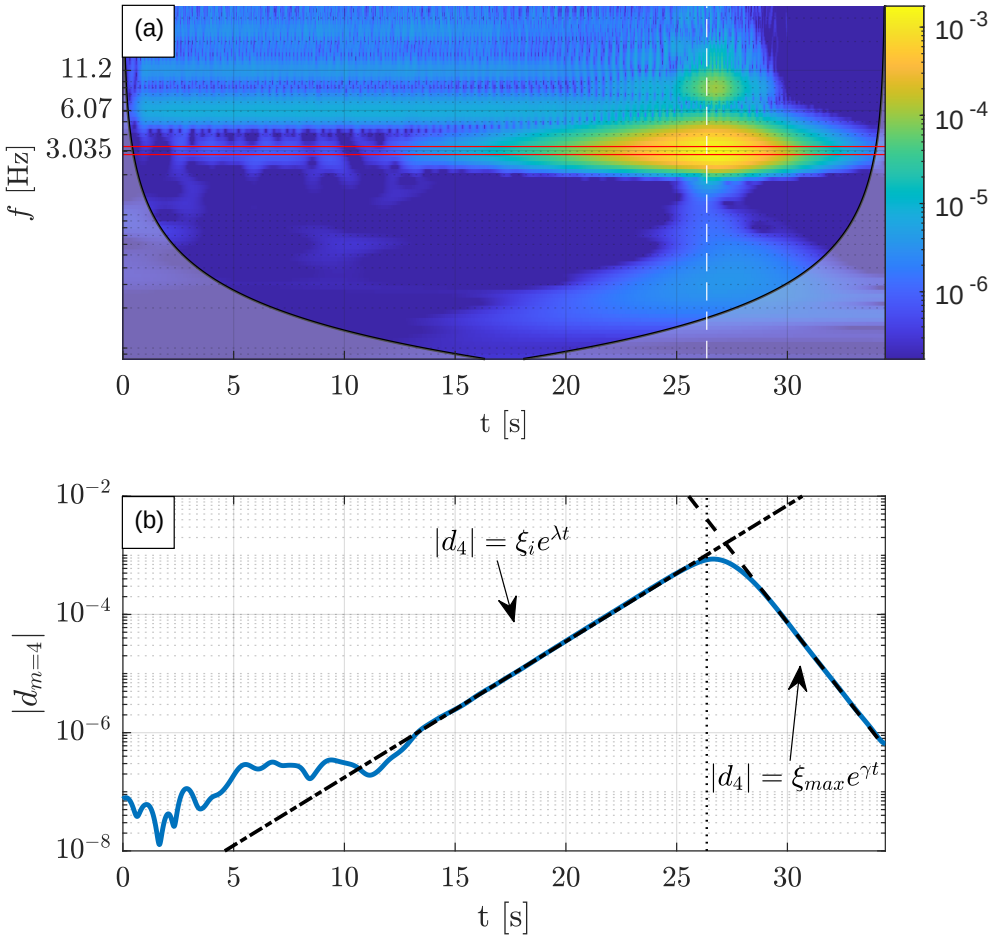

Figure 6.4: In panel a), we see the frequency-time decomposition for ξ_4. The greyed out areas on the left and right-hand edges of the plot indicate regions for which the boundary effects of the wavelet are too large to neglect. The vertical line represents t_{stop}, and the red box indicates $\frac{f_d}{2}$.
Panel b) depicts the instantaneous amplitude for the mode as a function of time. The exponential amplification rate is extracted as the slope of $\log(|\tilde{\xi}_m|)$, and the initial amplitude is approximated as the linear offset. The exponential damping rate is extracted as the slope of $\log(|\tilde{\xi}_m|)$ for $t > t_{\text{stop}}$.

detection method to distinguish the signal from the noise. Roughly, region 1 extends from 0s to 12.5s. In region 2, we can see that the majority of experiments exhibit the exponential amplification that is predicted by the linear theories presented in Chapter 3. Interestingly, this region extends all the way to t_{stop} for the majority of experiments, but not for all of them.

We can define region 3 as a 'plateau' region to accomodate this observation. As stated, the duration of region 3 is close to zero for the majority of the experiments, however it is clear that the expected exponential amplification predicted by the linear theories fails once modes reach a certain amplitude. [2] Finally, we define region 4 to begin at t_{stop} for all experiments, and to continue until the end of the data aquisition. As expected, this region is characterized by exponential decay of the modes.

Though the detection method is not capable of resolving the initial amplitudes of the interface waves, we are still able to obtain an approximation of

$$|\xi_{m=4}(0)| = 10^{-9.2\pm0.4}\text{m}. \tag{6.7}$$

The values presented in panel b) must be taken with a grain of salt; these values are extrapolated all the way to $t = 0$, despite the shaker's amplitude of oscillation being too small to produce parametric amplification. Likewise, more work must be done to understand the nature of this log-normal distribution.

In panel c), we see that the distribution for the exponential amplification rate parameter λ_m resembles a flattened Gaussian, with

$$\lambda_m = 0.535 \pm 0.007\text{s}^{-1}. \tag{6.8}$$

In panel d), we can clearly see that the distribution of the measured damping rates is bimodal, with

$$\gamma_m = 1.08 \pm 0.01\text{s}^{-1}. \tag{6.9}$$

In order to explain the bimodal distribution of γ_m, we return our attention to Figure 6.1. In panel a), we can see that there is a clear increase in temperature of roughly 1.5°C between set S_1 and S_2 (denoted in Figure 6.2). It is conjectured that the bimodal distribution in γ_m is due to a shift in ambient temperature for the experiments (where an increase in temperature is expected to correspond to a decrease in fluid viscosity).

[2] The consistency of this plateau amplitude across experimental runs is quite interesting, however there was not enough time to investigate this properly

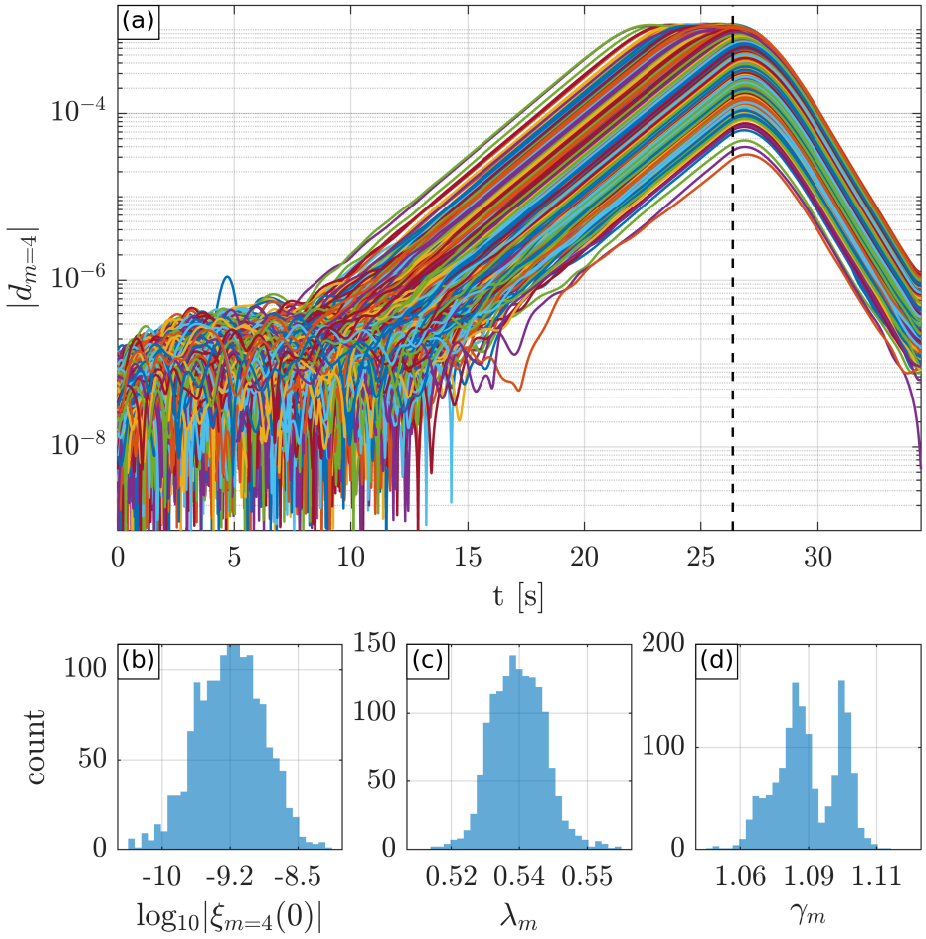

Figure 6.5: Panel a) depicts the log-scale amplitude versus time for each of the 1500 experimental runs. As demonstrated in Figure 6.4, an approximation of the initial amplitude, the exponential amplification rate and the exponential damping rate are extracted. Panel b) shows a histogram of the order of magnitude for the approximate initial amplitudes (in $\log_{10}$ meters). Panel c) shows a histogram of the exponential amplification rate, and panel d) depicts the distribution of the exponential decay rate (with units s^{-1}). Note the twin peaks in the exponential decay rates, which are believed to correspond to different temperatures.

Figure 6.6 displays the distributions for $|\xi_{m=4}(0)|$, λ_m and γ_m within the subsets S_1 and S_2. In panel a), we can see that the approximated initial amplitude distributions are quite similar. We have:

$$|\xi_{m=4}(0)|^{(S_1)} = 10^{-9.2\pm0.4}\text{m}, \qquad \text{and} \tag{6.10}$$

$$|\xi_{m=4}(0)|^{(S_2)} = 10^{-9.2\pm0.4}\text{m}. \tag{6.11}$$

In panel b), we see that S_2 has a slightly lower mean amplification rate when compared to S_1. This is likely due to an interplay between the shift in shaker amplitude and the shifted damping rates. The growth rates for the subsets are:

$$\lambda_m^{(S_1)} = 0.537 \pm 0.008\text{s}^{-1}, \qquad \text{and} \tag{6.12}$$

$$\lambda_m^{(S_2)} = 0.535 \pm 0.007\text{s}^{-1}. \tag{6.13}$$

Panel c) is perhaps the most interesting. The subsets were initially defined to correspond to regions of consistent shaker amplitude, and it can be clearly seen in figures 6.1 and 6.2 that the ambient temperature in S_2 is roughly 1.5°C warmer than it is in S_1. We can therefore conjecture that the shift in the γ_m distributions is due to a change in temperature. This is in line with the fact that fluid viscosities are expected to decrease with increasing temperature [100].

To the best of this author's knowledge, the difference in damping is believed to represent the most precise measurement of the damping rates for interface waves ever reported. [3] We have

$$\gamma_m^{(S_1)} = 1.100 \pm 0.008\text{s}^{-1}, \qquad \text{and} \tag{6.14}$$

$$\gamma_m^{(S_2)} = 1.080 \pm 0.005\text{s}^{-1}. \tag{6.15}$$

Finally, we investigate the so-called plateau region described above. In Figure 6.5, we note that once a mode reaches a certain amplitude, the exponential growth stops, and the amplitude plateaus at a somewhat steady level.

With this in mind, we can approximate the time that an individual mode stops growing using the log amplitude, as

$$t_{\text{grow}} \simeq \frac{\log(|d_4|_{\max}) - |\xi_4(0)|}{\lambda_m}. \tag{6.16}$$

[3] See [101] for comparable results, however in this paper, the authors do not state the number of repetions for each experiment.

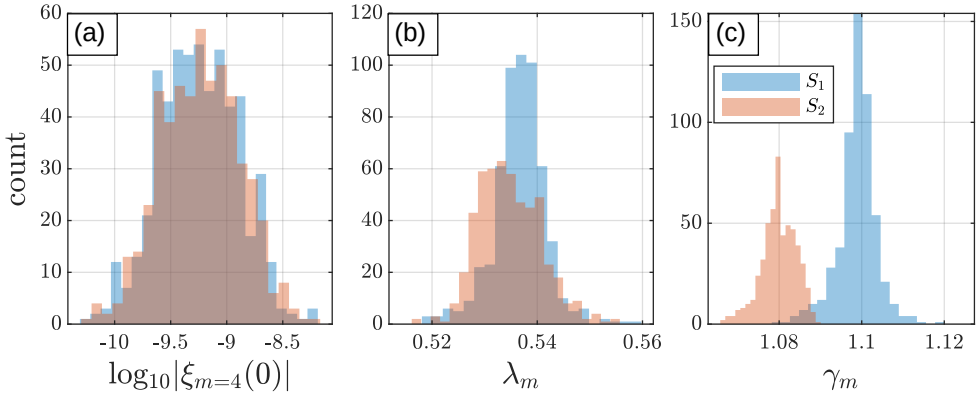

Figure 6.6: The distributions for the subsets S_1 and S_2. In panel a), we see that the approximated initial amplitudes have the same distribution for each subset. In panel b), we see that the center of the distribution for set S_1 is somewhat shifted compared to S_2, though the shift doesn't seem to be significant. Panel c) depicts the distributions for the exponential decay rates for each subset. It is conjectured that the damping rate for S_1 is larger due to the decreased temperature (see Figure 6.2). To this author's knowledge, the difference in the damping rates between S_1 and S_2 represents the most precise measurement of interface wave decay that has ever been reported.

Likewise, we can approximate the time that an individual mode starts decaying as

$$t_{\text{decay}} \simeq \frac{\log(|d_4|_{\max}) - |b_{\text{stop}}|}{\gamma_m}, \tag{6.17}$$

where $|b_{\text{stop}}|$ is the offset in equation (5.31). We then define a plateau time as

$$\Delta t_{\text{plat}} = t_{\text{decay}} - t_{\text{grow}}. \tag{6.18}$$

We then attempt to create a subset of 'plateau-runs' as follows:

$$S_P := \{U \therefore \Delta t_{\text{plat}} \geq \langle \Delta t_{\text{plat}} \rangle + n\sigma\}, \tag{6.19}$$

where U represents the full data set, and σ is the standard deviation of Δt_{plat}.

The results are presented in Figure 6.7, and are remarkably consistent with expectations when the number of standard deviations n, in equation (6.19) is set to 1. In panel c), we see that the modes that appear to reach a plateau begin with a larger amplitude in general. Since the amplification rate for each of the experiments is similar, this implies that once a threshold amplitude is reached, the modes dissipate energy into the other eigenmodes in the system, and exponential growth stops. In particular, we see in panel d) that since the plateau runs tend to have a similar amplitude, the standard deviation of S_P becomes smaller, and levels off before t_{stop}. In addition, the subset of non-plateau runs, $S_A = U \backslash S_P$ (where the A is for apparently-linear) peaks at t_{stop}, as we would expect. The plateau runs are scattered throughout the 50 hours of the experiment with no apparent clustering, suggesting that this plateau behavior is caused by random fluctuations in the initial state. The direct observation of a transition from linear to nonlinear behavior will be the topic of future investigations.

6.2 Field Theory Results

In this section, we will outline the results from the field theory predictions in section 5.3. We will begin by introducing some simulated experiments, and show that the relevant parameters (namely, η_m and λ_m) are in agreement with the data. We will then present the results for classical squeezing in the system, and compare the experiment to the simulations. Finally, we will provide some preliminary results regarding higher-order correlations, which suggest that the system is linear throughout most of its evolution.

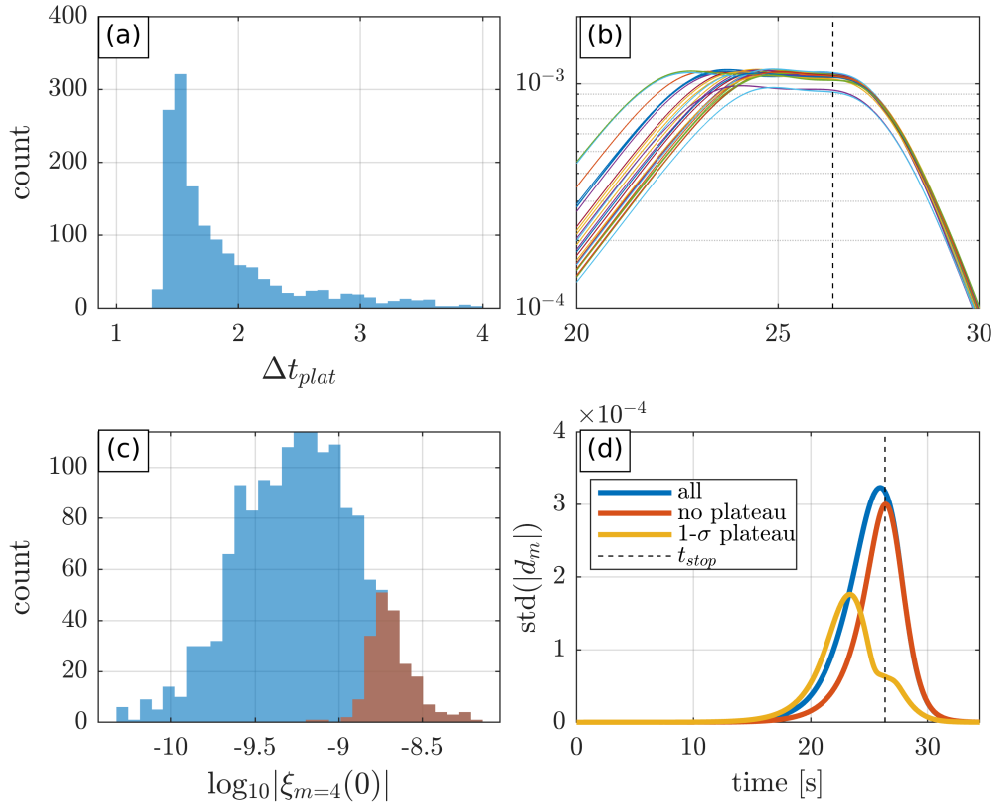

Figure 6.7: Deviations from expected linear behavior. Panel a) depicts the distribution of the plateau times Δt_{plat}. Experiments that show a 1σ deviation from the mean are considered plateau runs.
Panel b) demonstrates the plateau effect for the set of runs with a 3σ deviation (chosen for emphasis). Note that most runs in this set share a similar amplitude in the plateau region. The vertical dashed line represents t_{stop}.
Panel c) shows the overlap between the 1σ plateau set and the full data set for the distributions of the ($\log_{10}$) approximated initial amplitude.
In panel d), we show a heuristic check regarding the efficacy of the Δt_{plat} sorting method. Here, we see that the deviation in the non-plateau runs peaks at t_{stop} as expected. In contrast, since each run plateaus at a similar amplitude, the deviation between the 1σ runs decreases sharply before t_{stop}.

6.2.1 Classical squeezing results

Even though the majority of experimental runs appears to follow the predictions of the linear theory, the fluid physics equations leading to the equation of motion for the interface waves are known to be quite complex. This being the case, a comparison between a completely linear theory (provided by the ODE in equation (5.6), see section 3.5) and the data provides useful test to verify if deviations from predictions are the result of nonlinearities. The simulations were conducted to mimic the experiments as closely as possible. The damping rate for each simulation was chosen to match the damping measured for the same experiment. Likewise, the gravitational acceleration $g(t)$ was taken directly from accelerometer data (see equation (3.31) and Figure 4.2). Using the accelerometer data in the simulations allows us to incorporate any nuances in the time-evolution of the shaker's oscillations which might not be included otherwise. The largest potential deviation from the experimental parameters is likely the choice of initial state. For the simulations presented, the initial amplitude for each mode was sampled from a complex normal distribution, and scaled to have a similar order of magnitude as found in the experiment.

The resulting data is then treated exactly as experimental data, in the form of azimuthal Fourier amplitudes, as depicted in panel c) of Figure 6.3. Since the accelerometer data is not synchronized, individual simulations are synchronized in the same manner as the experiments, using a voltage signal from the indicator LED (read directly into the National Instruments card in this case), and then treated with the same wavelet analysis. The results for the exponential amplification rates λ_m are shown in Figure 6.8, and as can be seen, are in agreement with the experimental value. Since the primary parameters of interest in section 5.3 are γ_m and $\lambda_m = \eta_m - \gamma_m$, it is expected that the field theory predictions applied to the experiments and the simulations should coincide.

In Figure 6.9, we see the product of variances, predicted to be exponentially decaying for idealized statistics in equation (5.67), and increasing as $\mathrm{e}^{4\lambda_m t}$ when a finite number of experiments is considered.

In panel a), we see the decoherence parameter ϵ_m plotted versus time for both the simulation and the experiments. There are two interesting comparisons to make here. First, the simulation decreases to a constant value at a much faster rate than the experiment. If we accept the Floquet predictions for α_m and β_m, then the ratio $|c_m|N_m^{-1}$ should evolve as $(1-\epsilon_m)\tanh(\eta_m t)$,

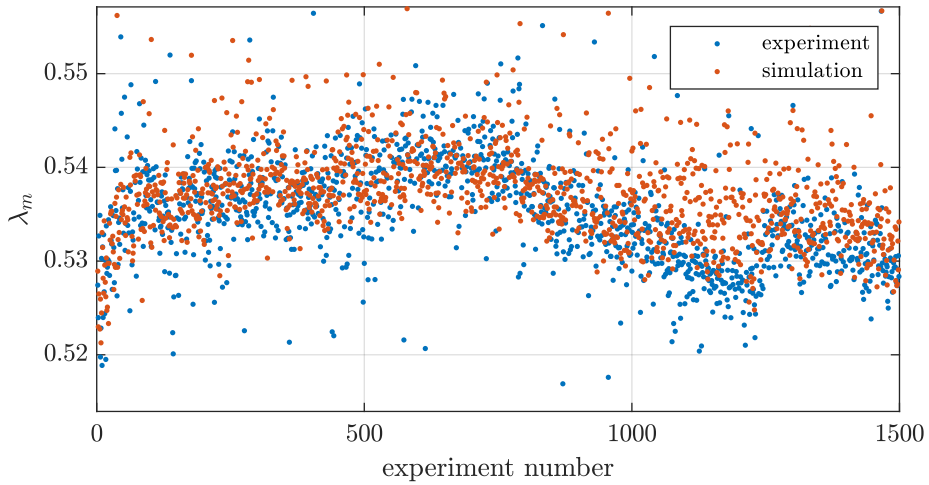

Figure 6.8: Simulated versus experimental amplification rates. By simulating the system using accelerometer data and the experimental damping rates (see equation (5.6)), we are able to obtain a close approximation to the experimental amplification rates. This close correspondence allows us to compare various field theory predictions for the experiment with a fully linear model.

so the rapid transition is expected. What is far less understood is the comparatively gentle slope for the experimental curve. As well, the experiment demonstrates a much larger value of ϵ_m than the simulations. Since the experiment and the simulations are synchronized in exactly the same manner, timing alone should not account for the discrepancy. In panel b) of Figure 6.9, we see that the product of variances does indeed follow equation (5.79), which adjusts for a nonzero ϵ_m.

Finally, we get to the classical squeezing. As described in section 5.3.3, the quadratures must be normalized in order for the concept of squeezing to have real meaning. According to equation (5.79), and the results in panel d) of Figure 6.9, it is not likely that product of variances will be constant as defined for the auxilliary field (equation (5.55)) if a system is dissipative and the experiment is conducted over reasonable timescales. Indeed, even for modest amplification rates, and a reasonable number of experiments, we will still find that the quantity on the left-hand side of the inequality in (5.80) is greater than 1.

With this in mind, the definition of (unnormalized) classical squeezing makes little sense in the presense of strong dissipation, and some form of normalization will be necessary. Figure 6.10 shows the squeezing results for the quadratures $Y_{\pm m}$. As we can see, the state does exhibit squeezing, in the sense that as time progresses, the probability of measuring $Y_m = Y_{-m}$ increases.

The timesteps for the squeezing plots have been chosen to correspond as closely as possible to the condition $2\mathrm{Re}(d_m d_{-m}^* v_m^2) = 2|d_m||d_{-m}|$, and for clarity one cycle of this oscillation is skipped between images. The interval was chosen to ensure that the signal was above the noise-level for the detection method, and we did not include redundant plots in which the degree of squeezing remains constant.

So, while further investigation is required in order to provide a full interpretation of the squeezing results, we have still demonstrated that it is possible to measure this effect in a dissipative system. This should perhaps be compared to the unnormalized squeezing results presented in Figure 6.11. This figure is only provided for comparison, to show that without normalization, one simply sees the probable amplitudes in the system increase.

It is somewhat surprising that the overall state is unsqueezed even at $t = 11.4$s, and as demonstrated in Figure 6.12, this behavior is not found in simulations. The initial timestep in Figure 6.12 is chosen so that we avoid boundary effects with the wavelet, and the final timestep is chosen well after

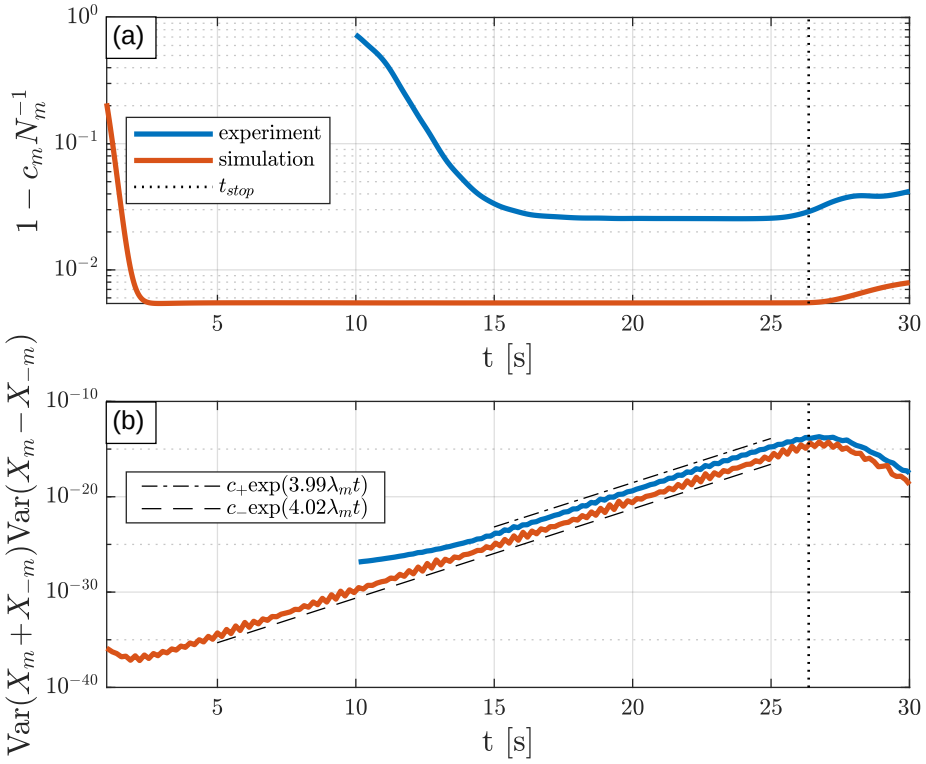

Figure 6.9: Panel a) depicts the decoherence parameter ϵ_m for simulations and experiments. Note how quickly the simulation value of ϵ_m stabilizes compared to the experiments.
In panel b), we see the simulated and experimental product of variances. As predicted in section 5.3.3, we see that the observed value is close to $4\lambda_m$.

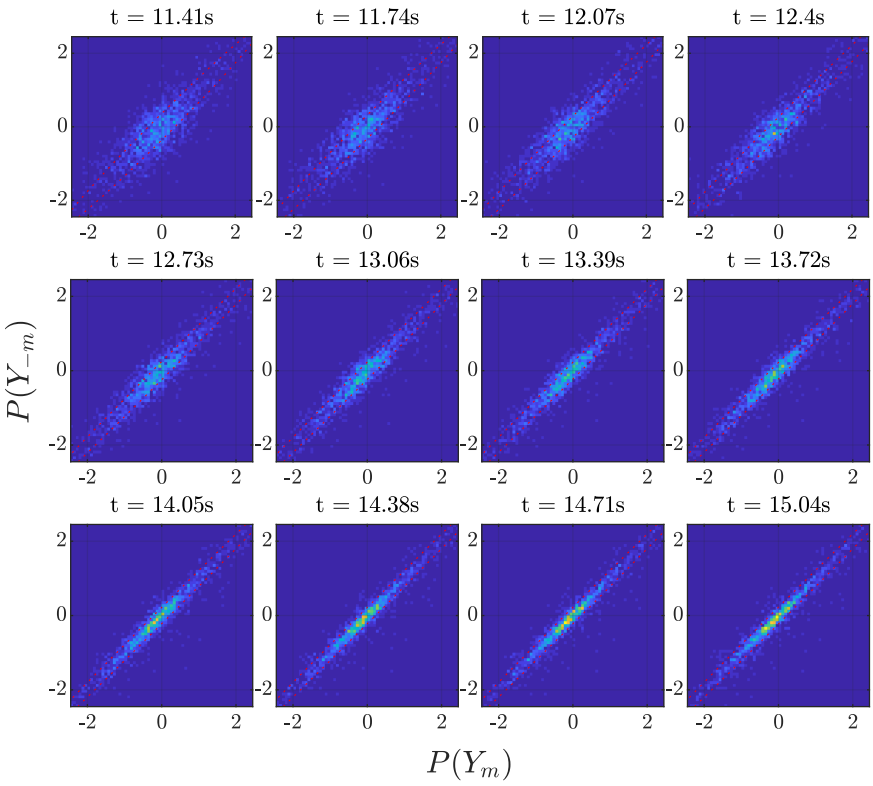

Figure 6.10: Classical squeezing of normalized mode functions. Each plot represents the probability distribution of the modes Y_m and Y_{-m} at the timestep indicated. The red ellipse has major and minor axes equal to $\mathrm{Var}(Y_m + Y_{-m})$ and $\mathrm{Var}(Y_m - Y_{-m})$ respectively, and area equal to π. As time progresses, the probability of measuring $Y_m = Y_{-m}$ increases until roughly 14s, after which the degree of squeezing remains constant. The constant nature of squeezing at late times reflects the decoherence parameter ϵ_m.

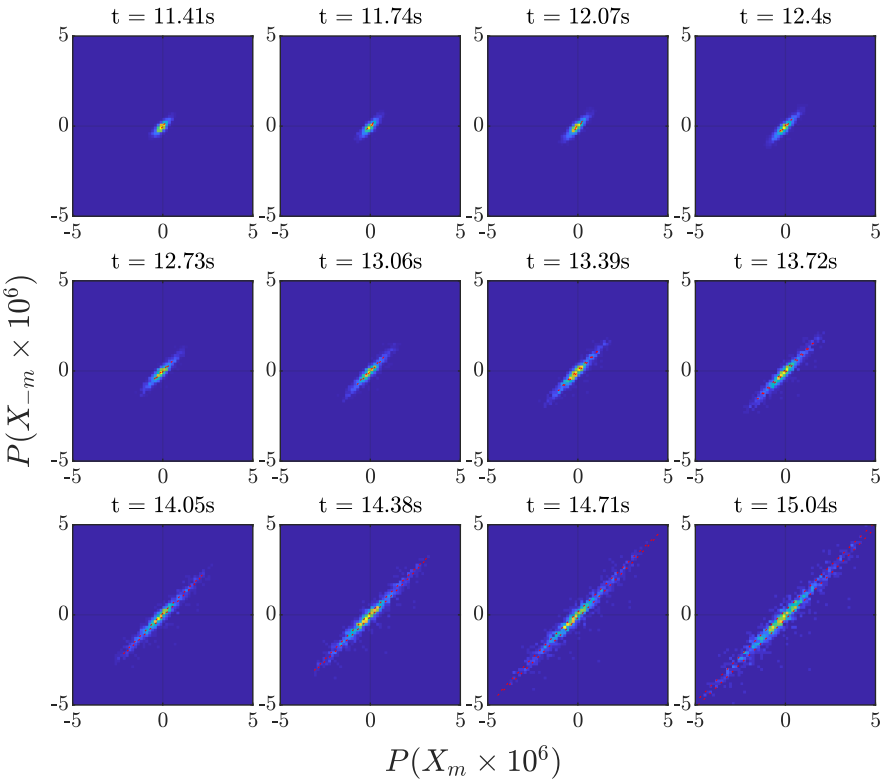

Figure 6.11: Classical squeezing of unnormalized mode functions. This figure is only for comparison to Figure 6.10. As can be seen, the minor axis of the ellipses are roughly constant, and the major axes grow with time.

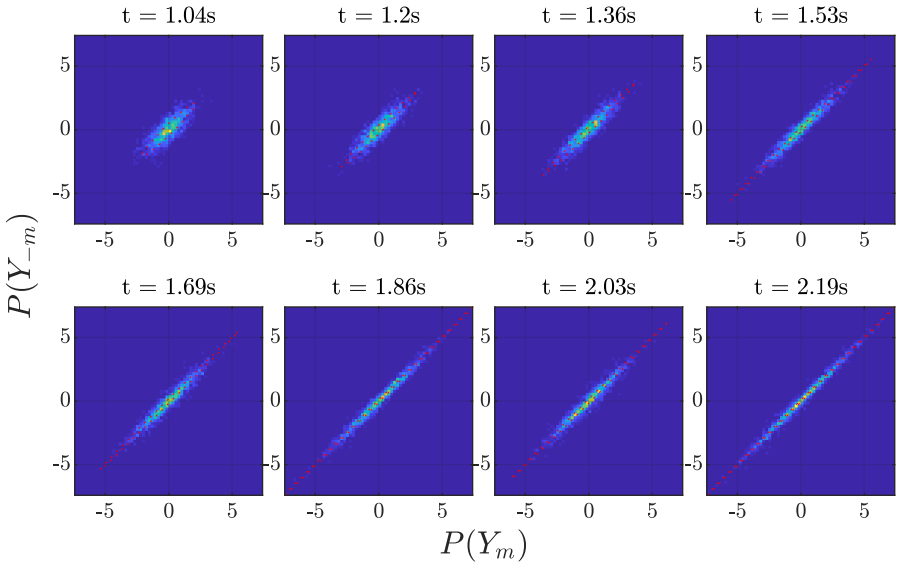

Figure 6.12: Classical squeezing for normalized, simulated data. The squeezing happens much more quickly with the simulated data for reasons that are not fully understood. As expected from Figure 6.9, panel a), the degree of squeezing becomes constant after a short time.

the degree of squeezing has become constant.

While this discrepancy is not completely understood, preliminary results for stochastic simulations suggest that this may be due to the viscous dissipation acting as a decoherent source in the system. Consider a modification to the equation of motion (5.35), to include a forcing term [102]:

$$\ddot{\xi}_m + 2\gamma_m \dot{\xi}_m + \omega_m^2 \xi_m = \Gamma_m(t), \tag{6.20}$$

where Γ_m satisfies a fluctuation-dissipation relation, for example

$$\langle \Gamma_m(t)\Gamma_m(t')\rangle_t \sim 4\gamma_m \frac{k_B T}{m}\delta(t-t'). \tag{6.21}$$

In the above, k_B is the Boltzmann constant, T is the ambient temperature, and m is some effective mass.

Figure 6.13 compares the quantity $1 - c_m N_m^{-1}$ for the simulations already presented, the experiment, and a (very preliminary) stochastic simulation

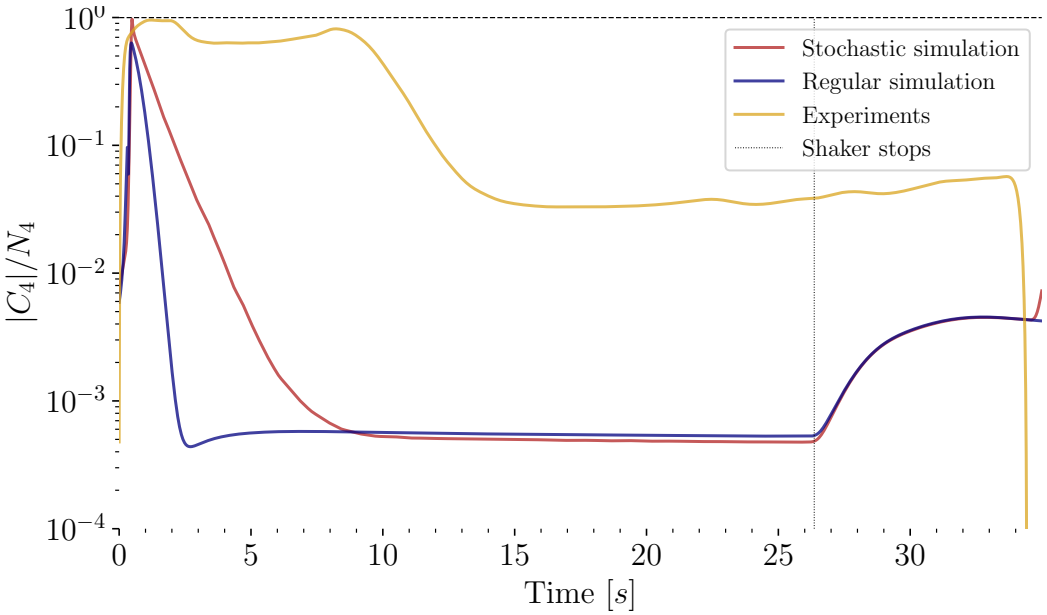

Figure 6.13: $(1 - c_m N_m^{-1})$ for preliminary stochastic simulations results. We can see that even perfectly synchronized stochastic simulations produce a nonzero decoherence parameter ϵ_m. As well, the initial slope of the curve for the stochastic simulations is much more similar to the slope of the experimental curve during the experimental intervale of interest, $t \simeq 11.5$s to $t \simeq 15$s.

(the details of which go beyond the scope of this report). The simulations are based off of an averaged accelerometer curve for $g(t)$, and so are perfectly synchronized. We can see from the resulting plot that the stochastic source, on its own produces some decoherence. As well, we see that the rate of change is midway between the regular simulations and the experiments.

Of course, much more work must be done in order to make concrete statements regarding these results, however it seems like a very interesting avenue of investigation. In particular, if this conjecture is correct, then the experiments may have demonstrated a new way in which to investigate the noise corresponding to the fluctuation dissipation theorem's predictions at large amplitudes.

6.2.2 Preliminary Results regarding higher-order correlations

In this section, we will present additional preliminary results which attempt to characterize the degree of nonlinearity in the system. As mentioned in Chapters 2 and 3, the underlying assumption beneath the analogy with cosmology is that the system is linear. While we demonstrated in figure 6.7 that a subset of the experiments stops obeying the predictions of the linear theory at large amplitudes, this on its own does not imply that the system is linear at small amplitudes.

The analysis that follows is motivated by Wick's theorem in quantum field theory, which has a classical counterpart in Isserlis's theorem [103, 104]. The results are included for the sake of completeness, however this investigation is being spearheaded by other members of the research group, and the theory and interpretation of what follows is beyond the scope of this thesis.

For central random variables, i.e. $\langle X_a \rangle = 0$, we can write a general four-point correlation function as

$$\begin{aligned}\langle X_1 X_2 X_3 X_4 \rangle =& \kappa\left(\{X_1, X_2, X_3, X_4\}\right) + \langle X_1 X_2 \rangle \langle X_3 X_4 \rangle \\ &+ \langle X_1 X_3 \rangle \langle X_2 X_4 \rangle + \langle X_1 X_4 \rangle \langle X_2 X_3 \rangle. \end{aligned} \tag{6.22}$$

Here κ denotes the joint cumulant, which reduces to $\kappa(\{X_a\}) = \langle X_a \rangle$ for singletons and $\kappa(\{X_a, X_b\}) = \langle X_a X_b \rangle$ for pairs. The joint cumulant $\kappa(A)$ for $|A| \geq 3$ is zero if, and only if, every $X_a \in A$ is Gaussian [105]. Therefore, the joint-cumulant $\kappa_4 \equiv \kappa\left(\{X_1, X_2, X_3, X_4\}\right)$ can only take non-zero values when it is non-Gaussian [105, 106]. Notice that in the Gaussian case, i.e. $\kappa_4 = 0$, Eq. (6.22) is the classical statistics analogue of Wick's theorem in quantum systems [103, 104].

Based on these observations, we consider equal-time four-point correlation functions of the form

$$G_m^{(4)} \equiv \langle \xi_m(t) \xi_m(t) \xi_m^*(t) \xi_m^*(t) \rangle = \langle |\xi_m(t)|^4 \rangle, \tag{6.23}$$

with a measure of Gaussianity defined by

$$\Gamma_m(t) \equiv \left\langle |\tilde{\xi}_m|^4 \right\rangle - 2 \left\langle |\tilde{\xi}_m|^2 \right\rangle^2 - \langle \tilde{\xi}_m^2 \rangle \langle (\tilde{\xi}_m^*)^2 \rangle \tag{6.24}$$

where $\tilde{\xi}_m(t) \equiv \xi_m(t) - \langle \xi_m(t) \rangle$.

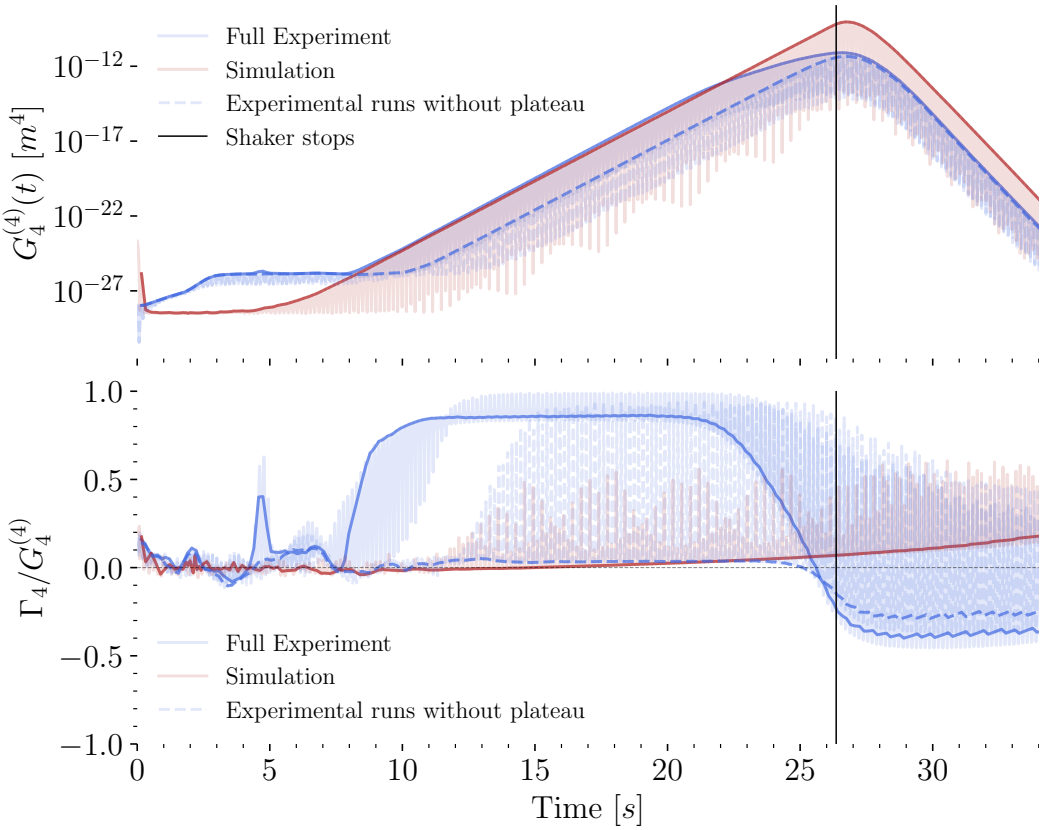

Figure 6.14: In the upper panel, the $G_m^{(4)}$ function is plotted for the full experiment, the simulation and the full experiment without plateau runs. The semi-transparent curves represent the functions as defined in equations (6.23) and (6.24), while the solid lines represent non-oscillating approximations computed using the complex amplitudes $d_{\pm m}$. In the lower panel, the measure of Gaussianity is plotted for the same. Note that for normally distributed random variables, the parameter $\Gamma_m(t)$ should be zero, as well as the large difference between each curve.
In particular, the sharp transition for the experiments is believed to be indicative of a change in the distribution of amplitudes. If this is true, the change in the Γ_m parameter implies the onset of nonlinear behavior, even for the (apparently linear) non-plateau subset. .

Figure 6.14 depicts the $G_m^{(4)}$ and the $\Gamma_m(t)$ functions for the full experiment, the non-plateau subset (which contains experiments that appear to follow the linear theory), and the simulations from introduced in the previous section. The semi-transparent curves represent the functions as defined in equations (6.23) and (6.24), while the solid lines represent non-oscillating approximations computed using the complex amplitudes $d_{\pm m}$ [107]. It is interesting to note that the non-plateau data set seems to deviate substantially from the full data set regarding this parameter. In particular, it appears that once the plateau runs are subtracted from the full set, the remaining data seems to be significantly more Gaussian according to this measure. In addition, it should be noted that even for the non-plateau set (which appears to behave linearly when each experiment is examined individually), there is a sharp change in the Gaussianity parameter *before* t_{stop}. This change in the distribution seemingly implies an onset of nonlinear behavior which is only visible statistically. For comparison, the simulated data set demonstrates no sharp transition (the gradual increase is suspected to be due to non-Gaussian damping and amplification rate distributions [107]).

While the data presented above is in very preliminary stages, it seems to suggest that the linear approximations assumed in the fluid theories of Chapter 3 can be quantifiably tested. If this interpretation is valid, then the statistical methods presented here further demonstrate that the analysis motivated by the cosmological analogy can inform the fluid physics community.

Chapter 7

Conclusion

The original motivation for the experiment outlined in this thesis was an analog system simulating exponential inflation in a superconducting magnet. Of course, the investigation that followed demonstrated that there was a great deal more to learn if we intended to make the statistical observations outlined in Chapter 2. In the end we designed and built a shaker, more precise than the state of the art aparatus described in [108]. We analysed and improved the detection method, automated the measurements, and after three iterations designed a fluid cell for a novel fluid-fluid system enabling us to repeat experiments with confidence. We developed the time-frequency analysis which allowed us to separate the positive and negative frequency waves in our system with minimal error, and we have demonstrated that it is possible to learn from a classical analog of two-mode squeezing, even when the system is subject to significant dissipation. In this section, we will summarize the main results of each chapter, and conclude this thesis by outlining some prospects for future investigations. We will close with a statement regarding the outlook for the original magnet experiment.

7.1 Summary of chapters

The analog proposed in Chapter 2 was the first to examine the potential of utilizing a strong-gradient magenetic field to change the analog metric in an interface wave system. In this chapter, we investigated the possibility of simulating an exponentially expanding universe by subjecting the system to a 200-fold decrease in the effective gravitational acceleration over a period of

less than two seconds. The first half of the chapter focused on the velocity potential, with the assumption that dissipation could be neglected. The second half of the chapter introduced new simulations which include dissipation in the equation of motion from the onset, and focused on the height field in the system (which is directly observable). The chapter concluded with a discussion of mode-freezing in the presense of damping.

In Chapter 3, we delved deeper into the underlying theory leading to the equation of motion for the height field presented in Chapter 2. From here, we examined the case of parametric resonance, looking in particular at the exponential amplification rate predicted by the simple dispersion relation. We then examined a more comprehensive theory, including boundary layers at the top and bottom of the vessel as well as at the fluid-fluid interface. Expanding on this, we attempted to include the boundary layers at the vertical sidewalls as well. Finally, we discussed the limitations of these predictions regarding the real fluid behavior, and propounded a phenomenological approach instead.

Chapter 4 detailed the experimental setup. The experiment was designed specifically to adhere as closely to the theoretical framework as possible. The resulting system was automized and provided an unprecidented degree of control over experimental parameters, allowing us to use the statistical analysis first investigated in Chapter 2. This included a description of the shaker itself, the detection method, the automation process, and the fluid-fluid system.

The analysis presented in Chapter 5 first attempted to reconcile the fluid theory described in Chapter 3 and the field theory in Chapter 2. This started with a mapping between the measured height field and the mode function representation favored in quantum field theories. From there, we explained the difficulty encountered with real-valued data, especially regarding oscillations with rapidly-varying amplitude. We then detailed some results from time-frequency analysis using wavelets, demonstrating that the wavelet methods would enable us to extract the instantaneous amplitudes of the mode functions. The rest of this chapter focused on the classical analog of two-mode squeezing, and showed that the theory could be extended to enable the observation of squeezing in the presense of dissipation.

Finally, in the results chapter we began by demonstrating the repeatability of the experiment. We then presented the results pertinent to the fluid theories presented in Chapter 3, including the parametric amplification rates, the damping rates, and an approximation of the initial amplitude in

the system. Within these results, we believe that we have produced the most precise measurement of the damping of interface waves ever published. We closed the chapter by presenting the results pertinent to analog cosmology. This section was mainly focused on classical squeezing, as detailed in Chapter 5, however preliminary investigations regarding statistical signatures of stochastic decoherence and nonlinearities in the system were also presented.

7.2 Future prospects and outlook

There are many different avenues of investigation that were left unexplored in this thesis. Starting with the fluid theories described in Chapter 3, the way forward is somewhat clear: The different theories have each made different predictions, and each of these must be tested. Regarding the analysis and the results, further work is necessary in order to understand what can be learned from the classical squeezing results. Likewise, the decoherence produced from the stochastic source term presented at the end of Chapter 6 is quite interesting, and it seems as though there is a lot of information to glean from the theory as well as the simulation and experimental data. The same can be said regarding the higher order correlation results; there is a great deal more that is unknown than there is understood, though this is perhaps not terribly surprising considering the complexity of the system we are studying.

Experimentally, there is always more to do. The precision of the system could be pushed further. A stronger driver could be installed alongside electromagnetic damping in order to give the spring-mass system a broader resonance spectrum. This would hopefully provide an even more precise amplitude response over the course of thousands of experiments. The pattern used in the detection method could be replaced (along with the lens, the camera, and the light source) in order to obtain better contrast, and better precision. The fluid vessel could be redesigned to enable the meniscus to be pinned in order to fix the radial boundary conditions more accurately. The modifications and enhancements to the setup depend on the direction in which the research leads. Currently, there are several planned extensions to this project: [1]

[1] A note should be made regarding the long list that follows, and the interruptions to the research presented in this thesis due to the pandemic. After the first lockdown ended, it was not possible to simply pick up where we had left off as we would have hoped. For various technical, bureaucratic, logistical, and social reasons we found that things did not

1. The experiment will be repeated at different frequencies and amplitudes in order to test the predictions of Chapter 3.

2. An investigation will be conducted regarding the nonlinear regime, both at the onset and in the late stages.

3. A novel interferometric detection method, based on the FTP algorithm will be implemented in order to resolve the initial state and explore the information content of correlation functions with order ≥ 4.

4. The experimental techniques and procedures developed with be translated to superfluid helium interfaces.

5. The classical setup will be translated to the superconducting magnet facility at the University of Nottingham in order to test the predictions made in Chapter 2.

6. Following the project at the University of Nottingham, the system will be moved to one of the Bitter magnet facilities outside of the country (for example, see [60]).

In short, a new line of research has started on interface wave metrology applied to fluid and superfluid systems.

progress as quickly as they had in previous years. In the list below, items 1 and 2 would have been included in this thesis, and much work was put into item 3 before the pandemic started and plans were subsequently changed as a result of it.

Appendix A: Detection Method, precision and noise

In this section we will outline the overall process used in the detection method for the parametric resonance experiment. An explaination of how the method works will be given, followed by a simple treatment of the discretization of pixel intensities. Next, the algorithm used will be explained, along with a framework allowing us to investigate the accuracy and precision of a given measurement using a discretized (digital) camera with noise. Finally, we will describe the specific procedure used in the shaker experiment, and provide results about the noise in the shaker experiment measurements.

Takeda first published a description of Fourier transform profilometry in 1983 [82], wherein a 1D sinusoidal pattern was projected onto the surface of a 3D object exhibiting diffuse reflection. Figure A.1 depicts the optical arrangement first described by Takeda.

If we define the distances $L = \overline{PC}$, $H = \overline{DA_s} + \overline{A_sB}$, $\mathrm{d}x = \overline{A_0A_a}$, and $h(x,y) = \overline{BA_s}$, then we have (due to the similarity of triangles $\triangle A_sSC$ and $\triangle A_sA_0A_a$) a relation between the height of the point A_s, and the apparent shift in position on the imaging plane $\mathrm{d}x$ (hereafter referred to as an optical displacement):

$$h(x,y) = \frac{\mathrm{d}xH}{L + \mathrm{d}x}. \tag{A.1}$$

This simple relation allows one to measure height field perturbations by equating them to optical displacements in the imaging plane, however the question remains: How can we convert light intensity measurements from a sensor array to a displacement?

A.1 Optical displacements with discretized intensity

In this section we will introduce a simple example system, and demonstrate how the discretization of pixel values limits the sensitivity of measurements. We will then introduce a simple improvement, and extend the arguements to

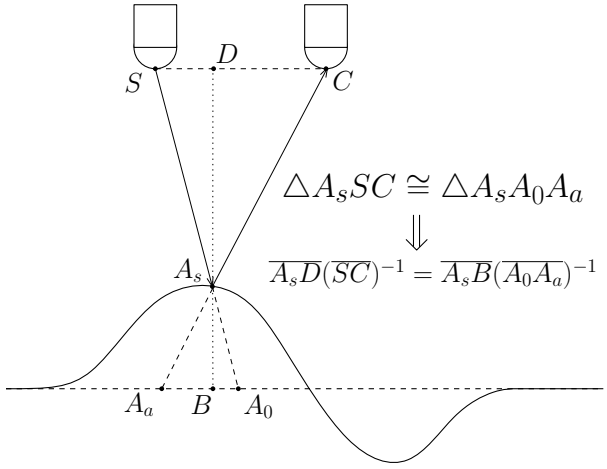

Figure A.1: Points S and C describe the positions of the light-source and camera respectively. If the surface profile is flat, a projected ray will strike the surface at point A_0, and this is the position of the ray that will be observed by the camera. However, when the height profile changes the surface intercepts the ray, which strikes at the point A_s. The apparent position, A_a of the point in the imaging plane will appear to shift when compared to the flat surface. Note that in the limit of a flat surface, we have $A_s = A_a = A_0$.

this example.

Consider a system in which all illumination on the surface is created by a projecter producing a perfectly linear intensity gradient along one dimension (as depicted in Figure A.2). The line containing points S and C is assumed to be parallel with the imaging plane. As well, the distance between the camera and the surface is assumed to be large when compared to any surface deformations considered (in particular, the figures above and below are not drawn to scale). In what follows, we will use the coordinates x, t and $P_t(x)$ to denote the (continuous) horizontal position, time and luminous intensity of points in the pattern (object) plane of the optical system.

If we choose image 0 such that the surface is flat, $P_0(x)$ gives the measured intensity as a linear gradient in x, and the value of $P_0(x_1)$ corresponds to the intensity created by the projector for that point. However, for a deformed surface, the camera measures the intensity at point A_s and assigns this value to the apparent location x_1. The actual value measured is the same as would be measured at point x_2 if the surface were flat. We can obtain the shift $\mathrm{d}x = (x_2 - x_1)$ by comparing the values of $P_1(x_1)$ and $P_0(x_1)$ since the linear gradient ensures that

$$P_1(x_1) = P_0(x_2) = P_0(x_1) + \kappa\,\mathrm{d}x, \tag{A.2}$$

for some easily measured value of κ. This would allow us to obtain the height profile using (for example) equation (A.1).

A.1.1 Estimations for minimum measurable displacement, based on discretized intensity

Since digital cameras are discrete by definition, we will need to take the discrete nature of these values into account. We will define a pixel to be a single photoelectric element within a digital camera's sensor array, indexed in the array by a pixel number n, which ranges between $[0, N-1]$ (and N is the total number of pixels in the direction under consideration). When an image is taken, some discrete number of photons from the pattern $P_t(x)$ strikes the pixel array. In what follows, we will use n, j and $I_j[n]$ to denote the sampled values of the above, where n and j represent some spacially averaged area and temporally averaged inverval respectively, and $I_j[n]$ represents the pixel intensity value (PIV) of a given pixel in the image plane of the digital camera's sensor array.

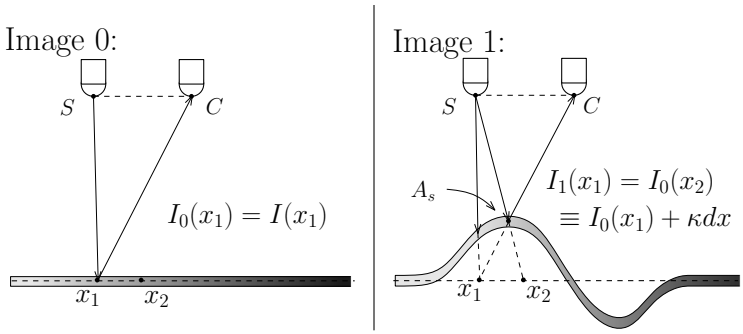

Figure A.2: Points S and C describe the positions of the light-source and camera respectively. The projector illuminates the surface with a linear gradient of light. When the surface is flat, the camera detects the light at point x_1, however when the surface is deformed, the camera detects an apparent shift in illumination, ΔI. In the case of a linear gradient, the apparent shift in illumination is linearly related to the apparent shift in position, dx.

We will likewise assume that the discrete values of $I_j[n]$ increase after a threshold number of photons is absorbed. This implies that the PIV $I_j[n]$ is a floored spacial and temporal average, where the index n represents the area of the pixel centered on x_n, and the index j represents the interval starting at t_j. In other words, when a threshold number of photons fall on the area indexed by n during the interval indexed by j, the PIV of $I_j[n]$ increases by one increment, which ranges from $[0, 2^B - 1]$. Here, B represents the bit-depth of the sensor, and it is a value limited by the camera's hardware.

As a familiar example of bit-depth in images, we can consider the 24-bit RGB standard that is ubiquitous in computer displays. Since the human eye can only percieve roughly 10 million different colors, computer displays are built to provide 8-bits for each of Red, Green, and Blue [109]. This allows display hardware to produce $2^8 \times 2^8 \times 2^8 = 2^{24} = 16,777,216$ different distinct colors, (and is the reasoning behind the 24-bit RGB standard). Because of this, grayscale images are typically limited to $B = 8$, so $I_j[n]$ is limited to the range of $[0, 255]$. To illustrate how this effects the limits of the detection method, let us consider the precision of the method described above. For this simple example, we will also assume that (by adjusting the intensity of the projector and the exposure time of the image) we are able to completely occupy the full range of the camera's bit-depth. For example, the brightest points on the surface are mapped to pixel values of exactly $I_j[n] = 2^B - 1$,

and the darkest points are mapped to exactly $I_j[n] = 0$.

In the above case, when $B = 8$, and $N = 1024$, one finds that for the flat surface,

$$I_0[n] = \left\lfloor \frac{2^B - 1}{N} \cdot n \right\rfloor \simeq \left\lfloor \frac{2^B}{N} \cdot n \right\rfloor = \left\lfloor \frac{1}{4} \cdot n \right\rfloor . \tag{A.3}$$

When comparing images of a deformed surface to this reference, we want to know what is the minimum $\mathrm{d}x$ that can be measured using this setup. To find the minimum possible apparent displacement $\mathrm{d}x[n] \equiv \delta n$ (in px), we apply the floor function and equation (A.3) to equation (A.2):

$$I_j[n] \simeq \left\lfloor \frac{1}{4} \cdot (n + \delta_j[n]) \right\rfloor .$$

If $I_j[n] = I_0[n]$, then we measure a zero shift, so we require that $|I_j[n] - I_0[n]| \geq 1$. This means that the minimum possible apparent displacement measurable with this setup is approximated by

$$\left\lfloor \frac{2^B}{N} \cdot (n + \delta_j[n]) \right\rfloor - \left\lfloor \frac{2^B}{N} \cdot n \right\rfloor \simeq \left\lfloor \frac{2^B}{N} \cdot \delta_j[n] \right\rfloor \geq 1$$

$$\implies \delta_j[n] \geq \frac{N}{2^B} = \frac{1024}{256} = 4. \tag{A.4}$$

In other words, using an 8-bit image with 1024 pixels in the direction of measurement, we are only able to measure a displacement of 4 pixels or more. (Not very good!) Comparing this to the same setup, using a camera with a bit-depth of 12,

$$\delta_j[n] \geq \frac{1024}{4096} = \frac{1}{4}, \tag{A.5}$$

we find that we can measure a displacement of 1/4 [px].

If one is limited by camera hardware, then a change in the projected pattern is necessary. Instead of a linear gradient, consider the same pattern mirrored about the center. The intensity of the flat surface can be modeled as a discretely sampled triangle wave, with wavenumber $k_0 = 1$:

$$I_0[n] = \left\lfloor A \cdot \mathrm{tri}\left(\frac{2\pi k_0}{N} n \right) \right\rfloor , \tag{A.6}$$

where $A \in [0, (2^{B-1} - 1)]$ is the amplitude, and is restricted by the bit-depth of the camera, and we have defined our triange wave to have unit amplitude:

$$\mathrm{tri}\left(\frac{2\pi k_0}{N} n \right) = \frac{8}{\pi^2} \sum_{a=1,3,5,\ldots}^{\infty} \frac{(-1)^{(a-1)/2}}{a^2} \sin\left(a \frac{2\pi k_0}{N} n + a\varphi_0 \right) . \tag{A.7}$$

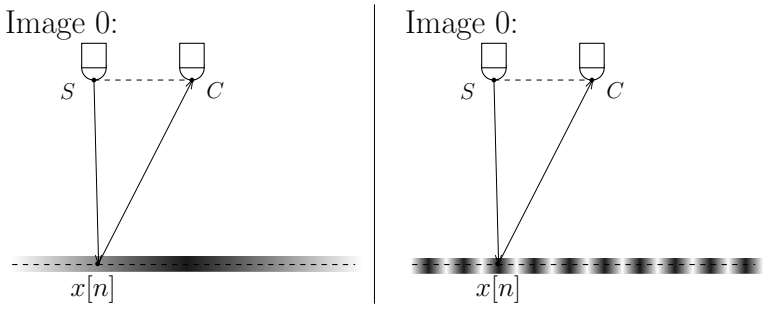

Figure A.3: The projector illuminates the surface with a repeating linear gradient of light. For the same (small) apparent shift in pixel position, $\delta[n]$, the change in the measured intensity is increased.

Using the same approximations as we did previously, and noting that the derivative of the triangle wave in equation (A.7) is (except at isolated points) equal to $\pm\frac{4Ak_0}{N}$, we have

$$I_j[n] = \left\lfloor A \cdot \text{tri}\left(\frac{2\pi k_0}{N}(n + \delta_j[n])\right)\right\rfloor \tag{A.8}$$

$$I_j[n] \simeq I_0[n] \pm \left\lfloor \frac{4Ak_0}{N}\delta_j[n]\right\rfloor, \tag{A.9}$$

which once again leads to an approximation for the minimum measurable pixel displacement, δ_0:

$$I_j[n] - I_0[n] \simeq \left\lfloor \frac{4Ak_0}{N} \cdot \delta_j[n]\right\rfloor \geq 1$$

$$\implies \delta_j[n] \geq \frac{N}{4Ak_0} \equiv \delta_0. \tag{A.10}$$

In the above example, with $B = 8$, we can estimate that $A \simeq 2^{(B-1)}$, so for $k_0 = 1$ we have that $\delta_j[n] \geq \frac{1024}{512} = 2$ as expected. Of course, one can simply increase the value of k_0 in order to increase sensitivity. For example when $k_0 = 10$, the resolution increases by a factor of 10, and we find that $\delta_j[n] \geq 0.2$ pixels. Figure A.3 illustrates this, and also demonstrates a trade-off: The larger the k_0 value, the more care must be taken for larger values of $\delta_j[n]$, since it becomes increasingly likely that a displacement will shift a full period of the triangle wave.

Due to the fact that $\left\lfloor A \cdot \mathrm{tri}\left(\frac{2\pi k_0}{N}(n+\delta_j[n])\right)\right\rfloor \neq I_0[n] \pm \left\lfloor \frac{4Ak_0}{N}\delta_j[n]\right\rfloor$ in general, equation (A.10) is a useful estimate, but it is not exact. In fact, since the pixel intensity values in $I_j[n]$ are rounded, there will always be so called 'lucky' pixels, for which even small fractions of δ_0 produce integer differences between $I_j[n]$ and $I_0[n]$. If we denote the apparent pixel shift by $\delta_j[n] = q\delta_0$, and abuse notation a bit by writing $I_j[n] \equiv I_j[n + q\delta_0]$, we find that

$$I_j[n + q\delta_0] - I_0[n] \leq \lceil q \rceil, \tag{A.11}$$

where $\lceil \cdot \rceil$ denotes the ceiling function, which rounds any input up towards the next largest integer.

We can see from the above that q corresponds to a measurable difference between the PIV of image j, and the PIV of the reference. When working with large numbers of pixels and large numbers of images, it is useful to estimate the expected change in PIV measured for a given constant shift, which can be calculated as the mean change in PIV across all pixels:

$$\langle q \rangle = \frac{1}{N}\sum_n I_j[n + q\delta_0] - I_0[n] \tag{A.12}$$

$$= \frac{1}{N}\sum_n \left(\left\lfloor A \cdot \mathrm{tri}\left(\frac{2\pi k_0}{N}(n+q\delta_0)\right)\right\rfloor - \left\lfloor A \cdot \mathrm{tri}\left(\frac{2\pi k_0}{N}n\right)\right\rfloor \right). \tag{A.13}$$

Figure A.4 depicts the expected value of $\langle q \rangle$ for various simulated pixel displacements for a triangle wave pattern as described above, and for a sinusoidal pattern, which is free of the higher-harmonics seen in equation (A.7).

Note that the estimation for minimum pixel displacement δ_0 relies on the gradient of the pattern, and that the irregularity of the gradient in the sinusoidal pattern corresponds to a lower probability of measuring a given displacement. However, when we use the slope of the triangle wave pattern to estimate the minimum displacement for both patterns, we once again measure (on average) the value of the input. This happy coincidence allows us to use equation (A.10) in both cases. Note however, that for *e.g.* $q = 1$ in this case, we will measure a PIV difference of 2 for some pixels when using the sinusoidal pattern. [1]

[1] It should be mentioned that in simulations, the systematic errors when using the triangle-wave pattern are much larger than the errors produced when using a sinusoidal pattern. This is likely due to the fact that the infinite higher harmonics of the triangle wave will appear in the pattern's FFT due to aliasing, (see equation (A.7)).

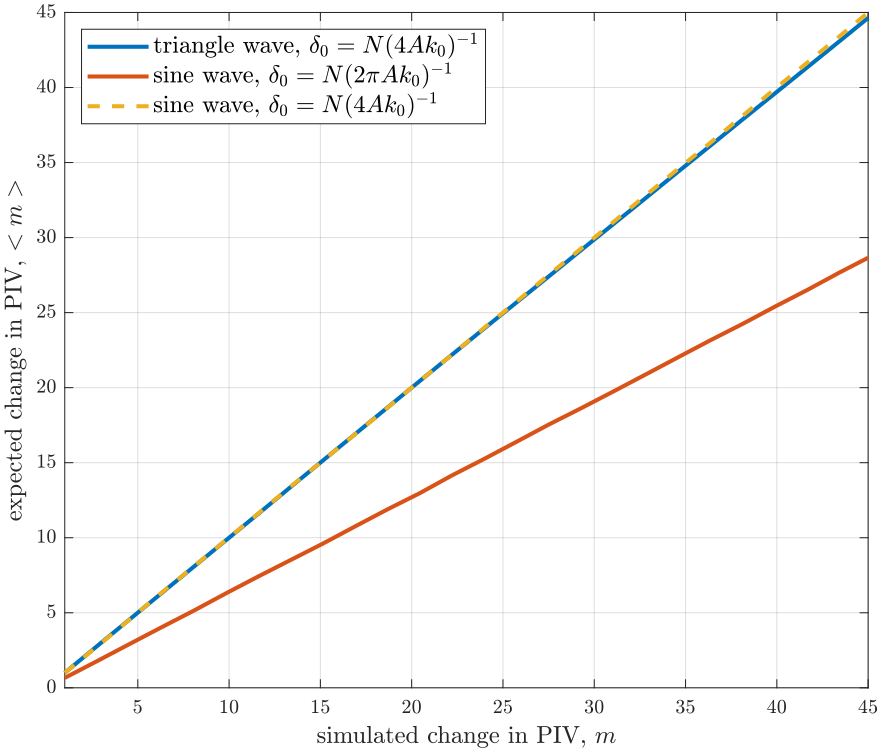

Figure A.4: The expected PIV difference between the ideal reference $I_0[n]$ and a simulated displacement $I_j[n]$, calculated using equation (A.12). The blue curve gives the expected pixel shift measurement for a triangle wave, where the nearly constant slope produces quite regular results. The red curve gives the expected pixel shift for a sine wave, however the irregular gradient of the reference reduces the probability of measuring the expected shift. The yellow curve demonstrates that a sinusoidal pattern produces the same results as a triangle wave pattern so long as we raise the estimation for the minimum displacement measurable.

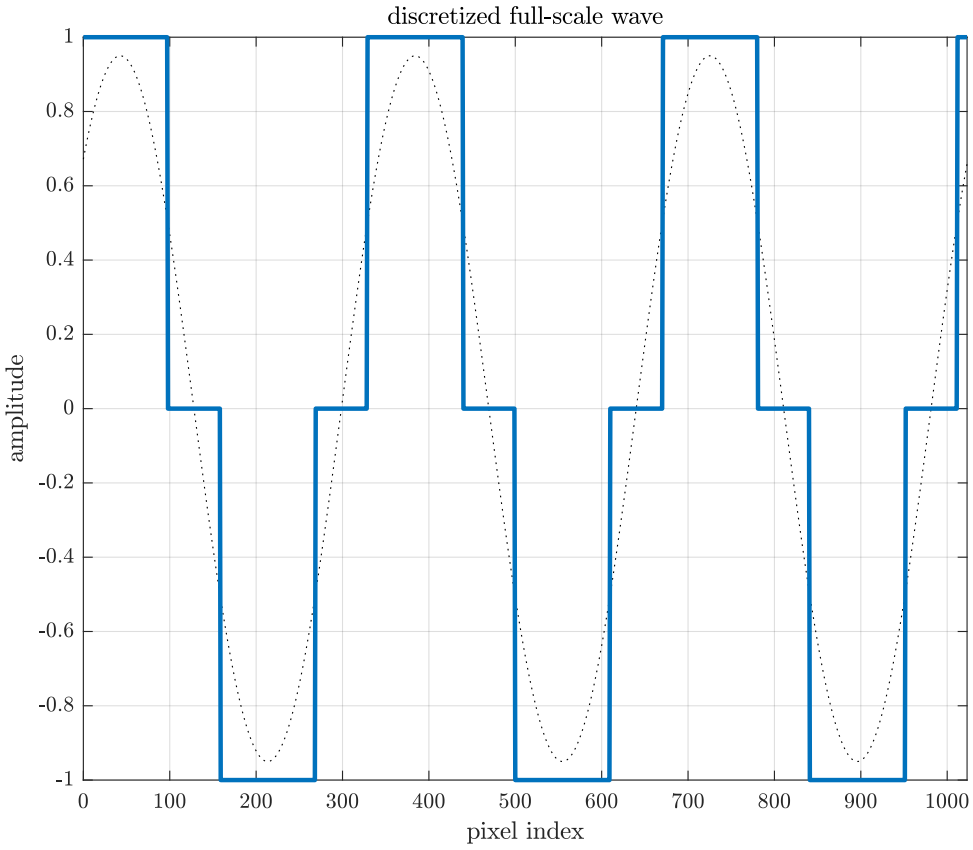

Figure A.5: A sine wave restricted to three intensity values.

A.1.2 Quantization noise and SNR

Before moving forward and developing the FTP algorithm, a note should be made on how the minimum displacement value δ_0, and the expected change in PIV $\langle q \rangle$ defined above relate to measurable signals. Figure A.5 depicts a sine wave discretized with three separate amplitude levels, corresponding to $\{-1, 0, 1\}$. The sine wave is clearly correlated with the blue curve, however this is obviously not an ideal signal. In electronics, this type of error is regularly encountered in analog to digital converters (ADCs), and it referred

to as quantization noise [2]. Quantization noise is well-studied, and useful approximations are readily available when the number of amplitude levels is large (this is typically measured in bits, and typical ADC devices have at least 8 bits, or 256 amplitude levels to work with). When the number of discrete amplitudes is lower, the approximations can break down [110, 111], so we will instead estimate the quantization noise in our system numerically.

In keeping with the convention of calling the quantization errors noise, we define the quantization signal to noise ratio (qSNR) as the ratio of the root mean square (RMS) of the signal to the RMS of the error. For a theoretical signal $y[n]$, and a discretized approximation $y_d[n]$, we have

$$\text{qSNR} = \sum_n \sqrt{\frac{y_d[n]^2}{(y_d[n] - y[n])^2}}. \tag{A.14}$$

Figure A.6 depicts the qSNR for signals of the form $y[n] = q \sin\left(2\pi k \frac{n}{N} + \varphi\right)$, quantized to the nearest integer. The range of k values covers different colored markers, as indicated by the colorbar on the right-hand side of the plot, and a range of values of φ is tested for completeness. One can see that as the value of q increases the qSNR does as well, however so does the spread of occupied qSNR values. It appears that increasing the value of k increases the spread in qSNR as well.

A.2 The FTP algorithm with discretized intensity values

At its core, the FTP method is simply an efficient method of extracting optical displacements from periodic patterns. We will work with a generic periodic pattern defined as $P_j(x) = P_0(x + \delta_j(x))$, describing a continuous function of a continuous variable, and an exact displacement $\delta_j(x)$. We will assume a bit-depth of $B = 12$, as can be found in many experimental digital cameras. The amplitude $A[n]$ defined below is simulated as a constant, defined relative to the bit-depth (and rounded to the nearest integer) as $A \simeq \frac{2^B}{3} = 1365$. The frequency of the pattern is chosen to be the same as the value obtained for experiments, $k_0 = 108.3\text{px}^{-1}$, and the number of

[2] Personally, I would be more inclined to call this quantization error as opposed to noise, but we will follow the convention used in the electronics literature.

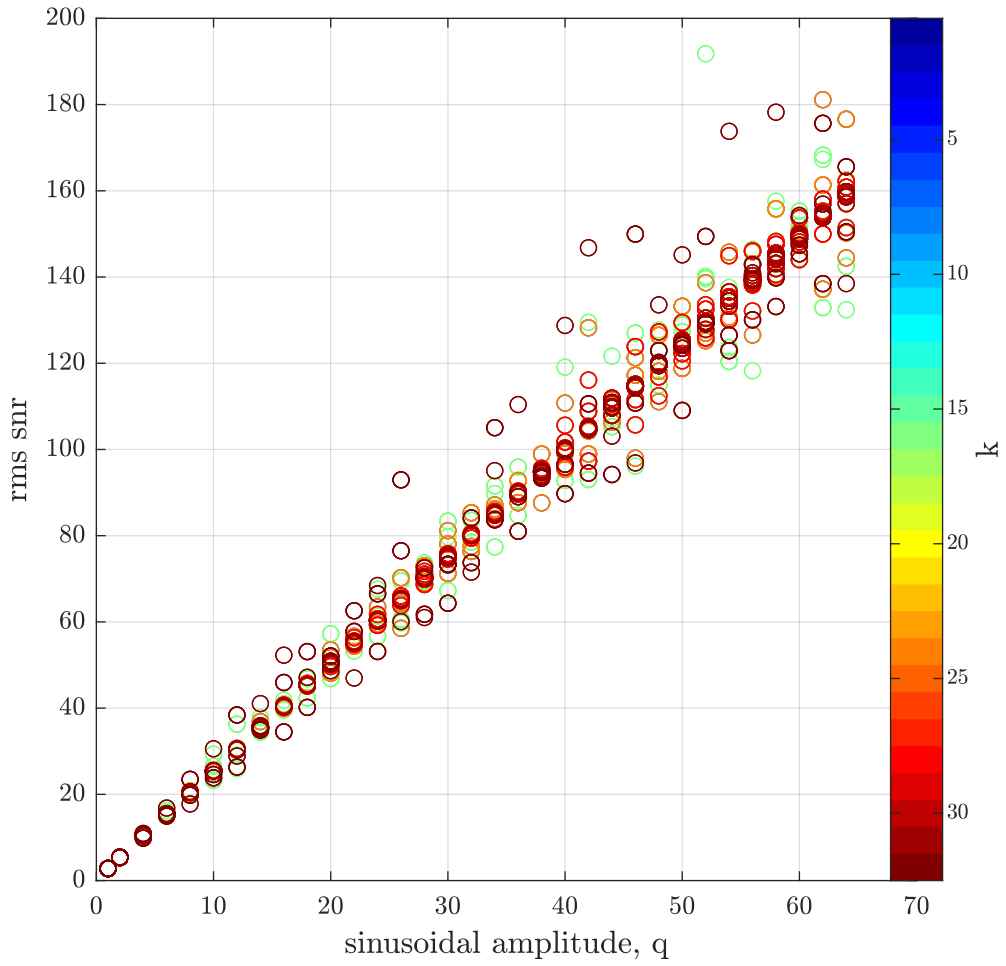

Figure A.6: qSNR as calculated from rounding $y[n] = q \sin\left(2\pi k \frac{n}{N} + \varphi\right)$ to the nearest integer. The signal is simulated across a range of amplitudes q and frequencies k. Increasing q and k both seem to increase the spread of qSNR values. Variations in φ also produce small variations in the qSNR.

pixels N is taken to be 1024. Together, these parameters define the estimated minimum measurable displacement as

$$\delta_0 = \frac{N}{4Ak_0} \simeq 1.7{\times}10^{-3}\text{px}. \tag{A.15}$$

In general, there are three steps in any FTP algorithm:

1. Convert the (real) image of the periodic pattern into a complex exponential of a single frequency:

$$P_j(x) \mapsto I_j[n] = B[n] + A[n]\cos\left(\frac{2\pi k_0}{N}[n + \delta_j[n]]\right) \tag{A.16}$$

$$\mapsto \tilde{I}_j[n] = A[n]\exp\left(\frac{i2\pi k_0}{N}[n + \delta_j[n]]\right) \tag{A.17}$$

2. Extract the local phase shifts by multiplying $\tilde{I}_j[n]$ by the complex conjugate of a reference image, $\tilde{I}_0[n]^*$ and calculating the argument of the result:

$$\tilde{I}_j[n] \cdot \tilde{I}_0[n]^* = A[n]^2 \exp\left(i2\pi k_0[n + \delta_j[n]]\right)\exp\left(-i2\pi k_0 n\right) \tag{A.18}$$

$$\mapsto 2\pi k\delta_j[n] = \delta\phi_j[n] \tag{A.19}$$

3. The phase $\delta\phi_j$ is a real number between $-\pi$ and π, with units of radians. For phase-displacements larger than 2π, artificial discontinuities will need to be removed using a phase-unwrapping algorithm before the optical displacement, $\delta x = \frac{\delta\phi}{2\pi k_0}$, is calculated.

The analysis in this section will focus on step 1, which can also be seen as a type of Hilbert transform (commonly used in signal processing). For signals of finite length, the Hilbert transform is approximated using a digital filter and can be understood as an operation which filters out Fourier contributions with negative k values:

$$\cos(2\pi kx + \varphi) = \tfrac{1}{2}\left(\mathrm{e}^{i2\pi kx + i\varphi} + \mathrm{e}^{-i2\pi kx - i\varphi}\right) \tag{A.20}$$

$$\mapsto \mathrm{e}^{i2\pi kx + i\varphi}\,. \tag{A.21}$$

In the above and in what follows, we will focus on small displacements $\delta_j[n] \equiv q_j[n]\delta_0$, where $q_j[n]$ corresponds to the jth image's expected PIV shift defined above, and δ_0 is estimated using equation (A.10).

If $\delta_j(x)$ is a sinusoid with amplitude $\delta_{\ell,j}$, a Taylor expansion about $\delta_{\ell,j} = 0$ produces

$$\begin{aligned} P_t(x) =& \sin\left(2\pi k_0 \left(x + \delta_{\ell,j} \sin(2\pi \ell x + \varphi)\right) + \theta_0\right) && \text{(A.22)} \\ =& \sin\left(2\pi k_0 x + \theta_0\right) + \delta_{\ell,j} \cos\left(2\pi k_0 x + \theta_0\right) \sin(2\pi \ell x + \varphi) && \text{(A.23)} \\ =& P_0(x) + \frac{\delta_{\ell,j}}{2}\big(\sin\left(2\pi \ell_+ x + \varphi_+\right) + \sin\left(2\pi \ell_- x + \varphi_-\right)\big), && \text{(A.24)} \end{aligned}$$

where $\ell_\pm = \ell \pm k_0$, and similarly, $\varphi_\pm = \varphi \pm \theta_0$. For more general $\delta_j(x)$, it will be useful to decompose $\delta_j[n]$ into its Fourier components,

$$\begin{aligned} &P_t(x) - P_0(x) \\ &\qquad = \sum_{\ell \in B} \frac{\delta_{\ell,j}}{2}\big(\sin\left(2\pi \ell_+ x + \varphi_+\right) + \sin\left(2\pi \ell_- x + \varphi_-\right)\big), \quad \text{(A.25)} \end{aligned}$$

where L is the bandwidth of the displacement, and the index n is re-defined so that $n \in \left[-\frac{N}{2}, \frac{N}{2} - 1\right]$.

In order for step 1 to be successful, some conditions on the periodic pattern must be met. It is assumed that the varying amplitude $A[n]$ varies slowly when compared to the sinusoid $\cos(\frac{2\pi k_0}{N}[n + \delta_j[n]])$. [3] Further, we assumed that $B[n]$ (which may contain low-frequency information, or higher harmonics of the periodic pattern) is well-separated from $A[n]\cos(\frac{2\pi k_0}{N}[n + \delta_j[n]])$ in Fourier space. In practice, it is relatively easy to set up an experiment in which both of these assumptions are met.

A.2.1 The three filters

We will introduce three separate types of filters and examine the effect that each has on the measurement of $\delta_j(x)$. They are the top-hat (or sinc) filter, the Gaussian, and the flat-response filter. Each of the filters are normalized so that a real sinusoidal input at k_0 will produce a complex exponential output of the same amplitude (as in equation (A.20)).

In Takeda's original paper, step 1 was accomplished by performing an FFT on $I_j[n]$, and then multiplying the signal by a tophat function (also known as a brickwall filter, also known as an ideal filter) in Fourier space,

[3] In signal processing terms, the amplitude must satisfy the conditions of Bedrosian's theorem [112].

which we will denote by $S_W[k]$:

$$S_W[k] = \begin{cases} 2, & \text{for} \quad k_0 - W < k < k_0 + W \\ 0, & \text{otherwise,} \end{cases} \tag{A.26}$$

where the bandwidth, W is chosen so that $B[n]$ is eliminated from the resulting signal. This is equivalent to convoluting the signal $I_j[n]$ with a sinc function $s_W[n]$ in position space:

$$s_{\Delta k}[n] = 4\Delta k \,\mathrm{sinc}(2\Delta k n) \exp\left(\frac{i2\pi k_0 n}{N}\right) = \frac{\sin(2\pi\Delta k n)}{2\pi\Delta k n} \exp\left(\frac{i2\pi k_0 n}{N}\right), \tag{A.27}$$

which is highly non-local. As we will see, this filtering process produces excellent results when the image of the pattern $I_j[n]$ has no discontinuities (including at the boundaries of the image, which the FFT assumes are adjacent). Due to the global support of $s_{\Delta k}$, any sharp transitions in $I_j[n]$ will produce ripples which decay slowly as $\frac{1}{n}$.

The second filter considered has a Gaussian profile, which famously minimizes the product of the standard deviation in position space with the standard deviation in Fourier space:

$$\Psi[n] = \frac{2k_0}{\sqrt{2\pi}} \exp\left(-\frac{1}{2}\left[\frac{k_0 n}{N}\right]^2\right) \mathrm{e}^{\frac{i2\pi k_0 n}{N}}, \tag{A.28}$$

Since this profile minimizes the 'uncertainty' in position and frequency, it has been a popular choice in so-called wavelet transform profilometry studies [113, 114], however as we will see this filter produces systematic errors in the output. The filter presented is designed to have standard deviation of one full pattern oscillation in position space.

The third filter presented is a generic flat-response FIR filter, designed to have a steep dropoff in Fourier space, with as few non-zero terms as possible. The particular case presented is designed using Matlab's constrained equiripple FIR filter design function, `firceqrip`, however any FIR filter with an approximately flat passband would work similarly. The FIR filter $w[n]$ is designed to be low-pass and is used as a window function. The result is multiplied by a complex exponential with the pattern frequency in order to shift the filter in frequency space:

$$f[n] = 2w[n] \,\mathrm{e}^{\frac{i2\pi k_0 n}{N}} \,. \tag{A.29}$$

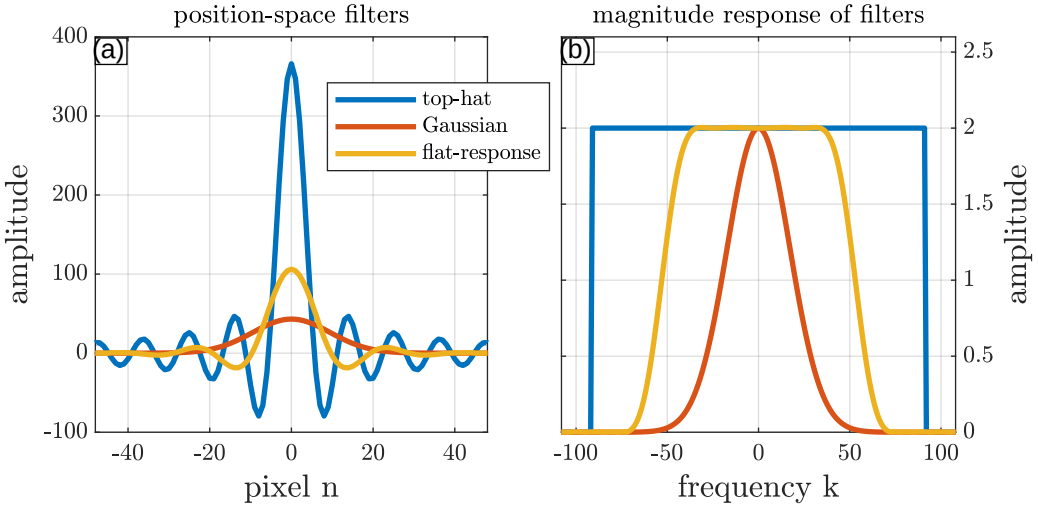

Figure A.7: Panel (a) depicts the filters used in the FTP procedure in position space. Note that the traditionally-used top-hat filter has very slow decay, and can be expected to have poor performance near boundaries.
Panel (b) depicts the mangitude-response of the three filters. The Gaussian filter drops off sharply from $k = 0$, causing a reduction in the measured amplitude of sinusoidal displacements which increases with the displacement wavenumber.

The window function presented is designed so that the maximum error in the pass-band and the stop-band will be 0.1%. The number of terms in the window (also specified as the order) is chosen so that the pass-band is as broad as possible in Fourier space, while the width of the filter in position space is as narrow as possible. In this case, roughly 99% of the filters influence is within three oscillations of the carrier signal.

Figure A.7 depicts the filters in both position space, and in Fourier space. The horizontal axis is shifted in Fourier space so that each filter is centered at $k = 0$. Comparison of panel (b) in Figure A.7 with equation (A.25) explains in short-order why the Gaussian filter is problematic. For $\ell > 0$, the ratio of the measured amplitude of a sinusoid $\delta_{j,\ell}[n]$ versus the actual amplitude (call it $\delta_{j,\ell}(x)$) will decrease proportionally to $\mathrm{e}^{-\ell^2}$.

Figure A.8 depicts simulation of the qSNR for various values of ℓ and the PIV shift q. The simulation produces a known sinusoidal shift $\delta_{1,\ell}$ and compares the results to the measured shift using the qSNR equation (A.14). Another interesting feature of the qSNR estimages in Figure A.8 is that for large ℓ, the qSNR seems to decrease rapidly even as we approach $\delta_{j,\ell} = 1$[px]. When the amplitudes of sinusoidal displacements are large, and the small-amplitude expansion (A.25) is no longer valid. For large amplitude displacements, the composition of sinusoids decomposes into an infinite sum of Bessel functions. As an example, for general t and x we have [79]:

$$\cos\left(t\sin(x)\right) = J_0(t) + 2\sum_{a=1}^{\infty} J_{2a}(t)cos(2kx), \tag{A.30}$$

where J_{2a} is a Bessel function of the first kind, of order $2a$.

Instead of working with infinite series, a useful estimate for the allowable amplitude of a given displacement can be calculated as follows [115, 68]. For a general signal, $y = \mathrm{e}^{iqx}$, we always have that $q = \frac{-i\partial_x y}{y}$. So, the phase of our Hilbert-transformed pattern $\tilde{I}_j[n] = \exp\left(\frac{i2\pi k_0}{N}\left[n + \delta_{j,\ell}\sin(\frac{2\pi\ell n}{N} + \varphi)\right] + i\theta_0\right)$ can be calculated as

$$\left(\frac{i2\pi k_0}{N}\left[n + \delta_{j,\ell}\sin\left(\frac{2\pi\ell n}{N} + \varphi\right)\right] + i\theta_0\right) = \frac{-i\partial_n \tilde{I}_j[n]}{\tilde{I}_j[n]}. \tag{A.31}$$

Ignoring the constant phase shift, we see that the phase of the shifted signal is roughly given by $\frac{2\pi k_0}{N} + \frac{4\pi^2}{N^2}k_0\ell\delta_{j,\ell}$. If the filter used in the method has a

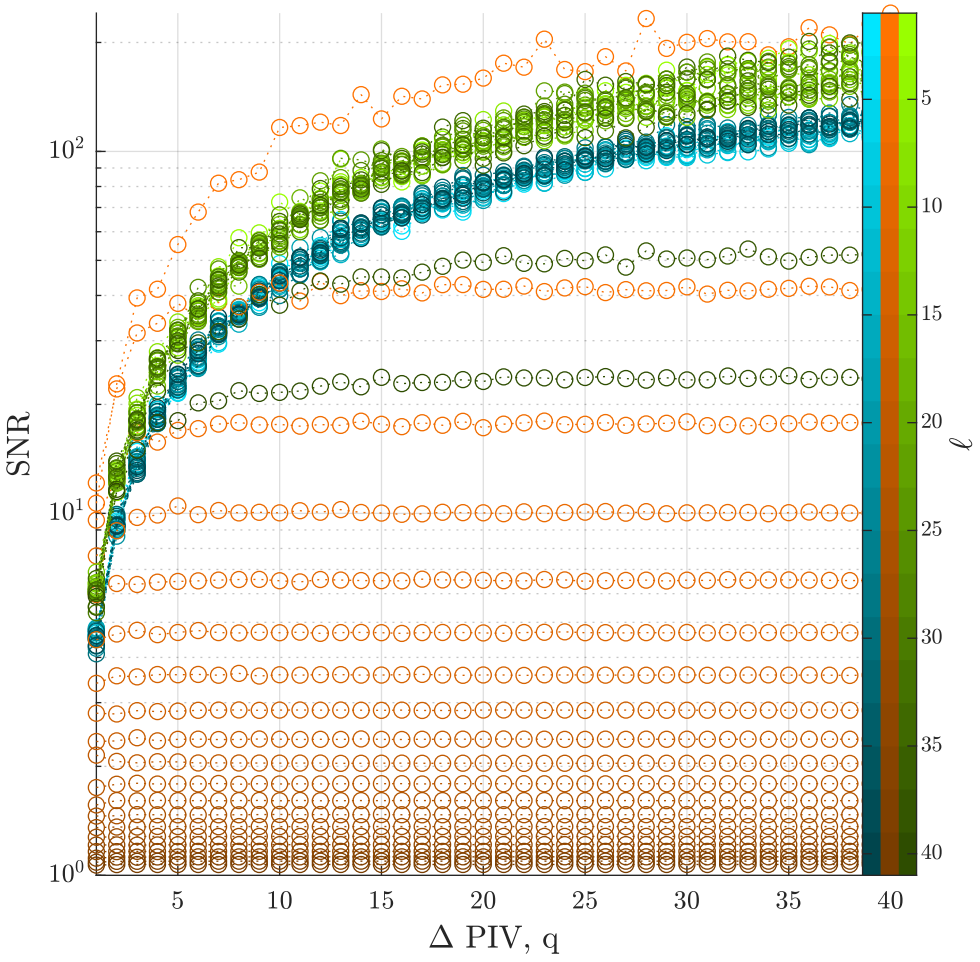

Figure A.8: The qSNR versus pixel displacement for the three filters. The horizontal axis labels the PIV shift on the bottom, and the pixel shift on the top. The simulated pattern is sinusoidal, and occupies the entire range from 0 to $N-1$. The blue, orange and green-tone points represent the qSNR for the top-hat, the Gaussian, and the flat-response filters respectively. The brightness of each color decreases with increasing ℓ.
The top-hat and the flat-response filters perform well for a range of ℓ values, while the error of the Gaussian filter increases with the wavenumber of the optical displacement.

spectral width of $2\Delta k$, then a faithful reconstruction requires that

$$\frac{4\pi^2}{N^2} k_0 \delta_{j,\ell} \ell < \frac{2\pi}{N} \Delta k, \tag{A.32}$$

which must be satisfied for each ℓ when $\delta_t(x) = \sum_\ell \delta_{t,\ell} \sin(2\pi\ell x + \varphi)$. This can be simplified further by noting that $\Delta k = \gamma k_0$ for some positive number $\gamma < 1$:

$$\delta_{j,\ell} \ell < \gamma \frac{N}{2\pi}. \tag{A.33}$$

If we denote γ_s as the spectral width of the top-hat filter, and γ_w as the width of the flat-response filter, we have, in general

$$\gamma_w < \gamma_s < 1. \tag{A.34}$$

One should note that equation (A.33) indicates that the most important parameter for measuring large displacements is the number of pixels sampled, N. Increasing the pattern frequency k_0 will help only in that this allows one to choose a slightly larger value of γ (this is because the spectrum of the $B[n]$ signal is likely to remain fixed). Figure A.9 depicts the qSNR versus PIV shift q for larger displacements. We see that when the product $\ell\delta_{j,\ell}$ is large, the flat-response filter does poorly compared to the top-hat filter. Examining Figure A.7, we can see that this is due to the comparatively large drop-off of the flat-response filter in Fourier space.

When the bandwidth L of the displacement field is large, the ideal cutoff of the top-hat filter enables one to set a larger value of γ while still excluding the unwanted image artifacts $B[n]$. However in the experiments conducted, nearly half of each image is obscurred by the fluid vessel. Figure A.10 depicts a simulated reconstruction for which the pattern is occluded at the edges and in the center. The simulated PIV shift is $q = 40$, and the other parameters are the same as in figures A.8 and A.9. Figure A.11 shows the qSNR results of a simulated displacement with an obscurred reference pattern. As can be seen, the errors are significantly reduced for the relatively local flat-response filter.

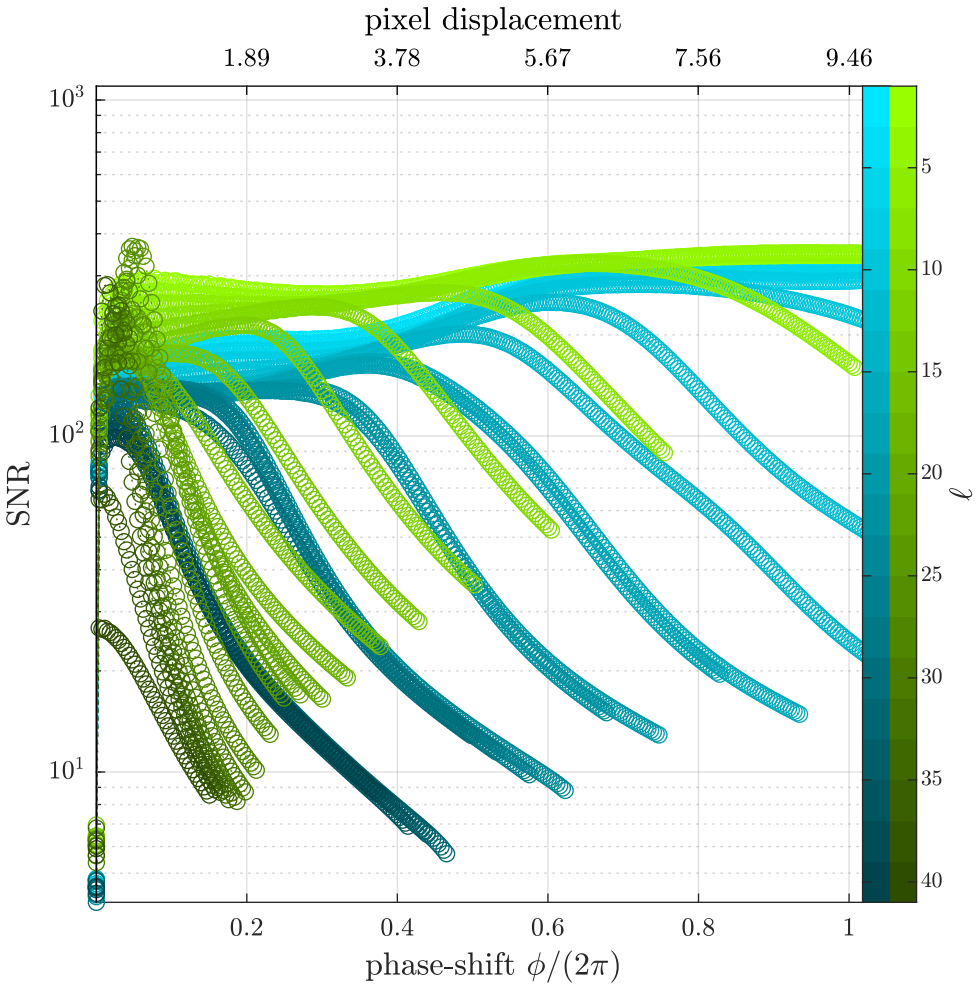

Figure A.9: The qSNR versus pixel displacement for large displacements. The simulated pattern is sinusoidal with $k_0 = 108.3$, and occupies the entire range from 0 to $N-1$. The blue and green-tone points represent the qSNR for the top-hat, and the flat-response filters respectively, and the brightness of each color decreases with increasing ℓ.
The horizontal axis denotes the apparent shift $\delta_{j,\ell}$ in pixels at the top of the plot, and as a fraction of the period of the pattern on the bottom. Equation (A.33) is used to define a cutoff. Simulated displacements not meeting the condition are not shown.

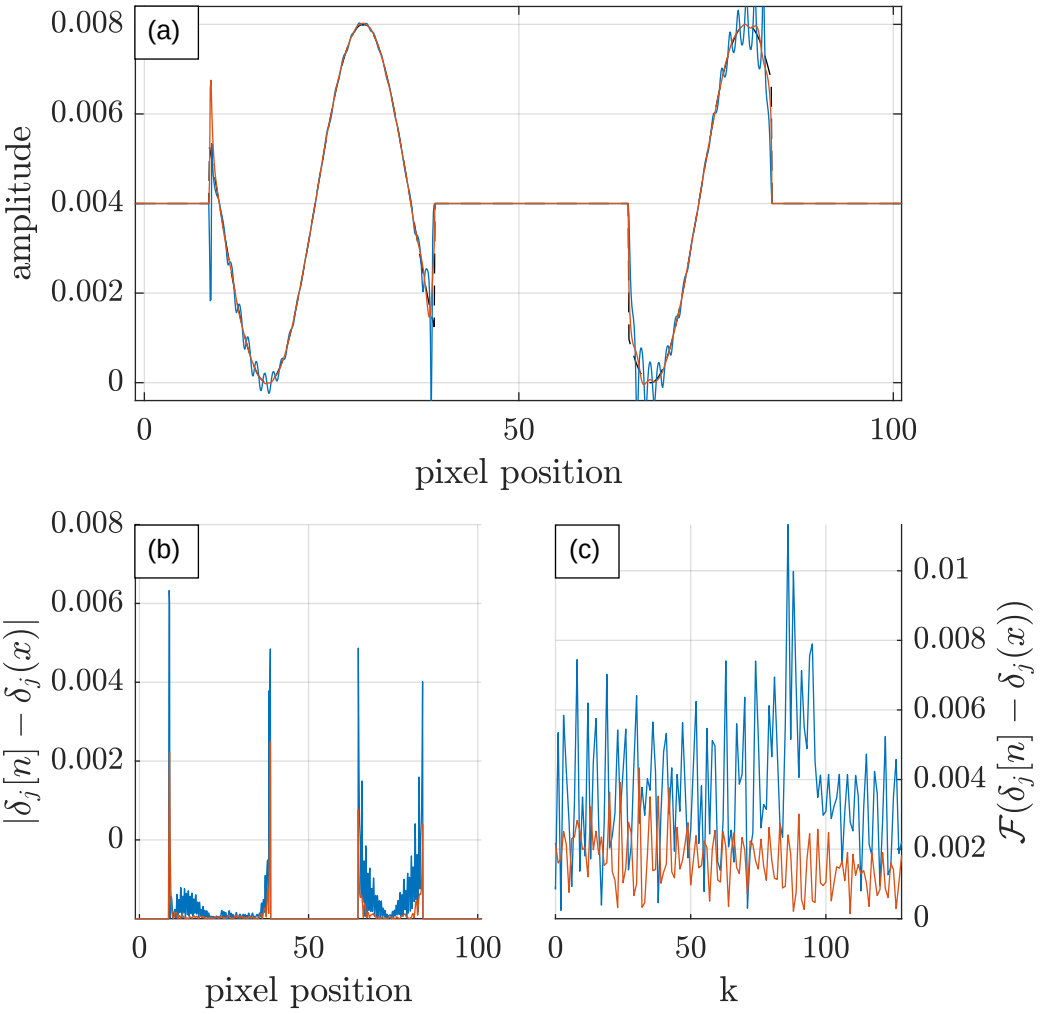

Figure A.10: Panel (a) depicts the simulated displacement $\delta_j(x)$, as well as the reconstructed displacements for the top-hat filter (blue) and the flat-response filter (red). The pattern is occluded at the edges and in the center. The quickly decaying flat-response filter ensures that boundary discontinuities are localized.
Panel (b) depicts magnitude of the error for each filter. Note that the errors are largest near the occlusion boundaries, however for the top-hat filter these errors propagate into the center of the reconstruction.
Panel (c) depicts the spectral amplitude of the error. Note that the error occupies all frequencies, implying that it cannot be easily removed with further filtering.

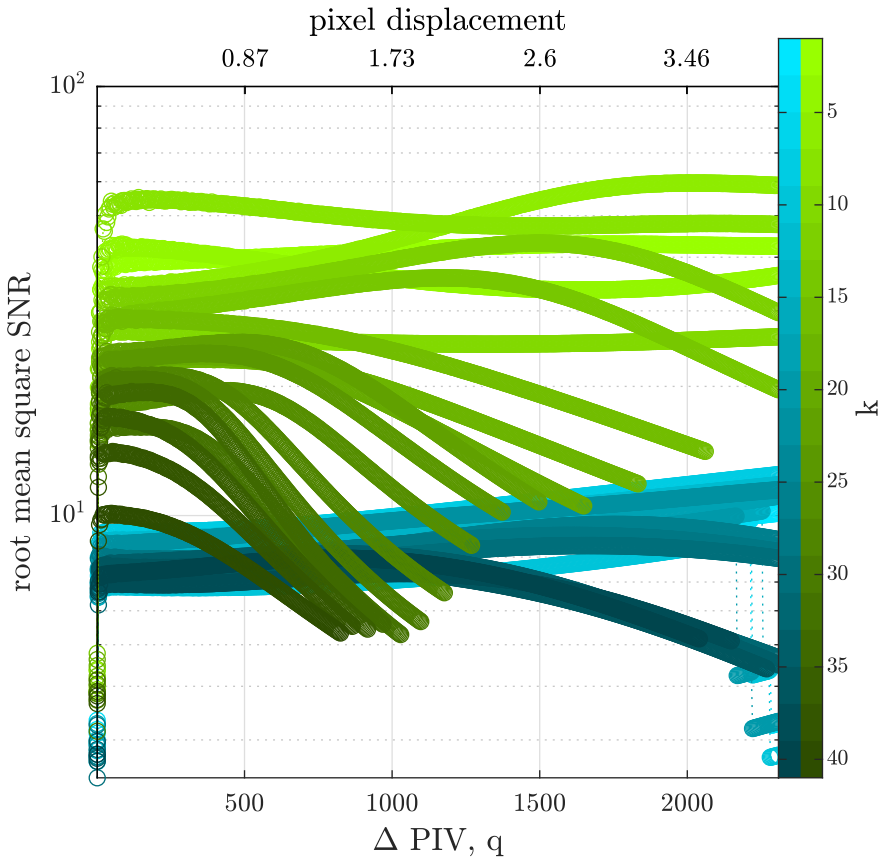

Figure A.11: The qSNR for a pattern obscurred at the boundaries, and in the center. The blue, and green-tone points represent the qSNR for the top-hat, and the flat-response filters respectively. The brightness of each color decreases with increasing ℓ.
The top-hat filter has a poor qSNR due to its lack of locality. However for large displacements and large ℓ, the flat-response filter performs poorly as well.

A.3 Implementation in the shaker experiment, the inclusion of noise

In this section, the Schlieren FTP method will be introduced, and the equations used for reconstruction will be given (without derivation). We will also provide values for the parameters A, k_0, N, and δ_0 introduced above.

In Takeda's original FTP paper, the pattern is projected onto a deformed surface with diffuse reflection, and the relationship between an observed optical displacement $\delta_j[n]$ and the height profile is simple enough to demonstrate in a single image (see Figure A.1). If refraction is used instead of reflection the optical geometry is not so simple, however similar geometric arguments allow one to relate the gradient of the height field $h(x, y)$ to observed displacements using the optical parameters of the system [83]:

$$\nabla h = -h_*^{-1}\delta\vec{x}, \tag{A.35}$$

where ∇h is the gradient of the height field, $\delta\vec{x}$ is the vector displacement (we need to measure two orthogonal displacements, δx and δy in order to invert the gradient operator), and h_* is an optical parameter given by

$$h_* = \left(\frac{1}{\alpha h_p} - \frac{1}{H}\right)^{-1}. \tag{A.36}$$

In the above, h_p is the distance between the pattern and the interface, H is the distance between the pattern and the camera, and α is a constant function of the index of refraction for both fluids:

$$\alpha = 1 - \frac{n_{\text{upper}}}{n_{\text{lower}}}. \tag{A.37}$$

The first methods utilized to obtain the displacements δx and δy, relied on digital image correlation (DIC) techniques and random 'speckle' patterns projected through the fluid interfaces [83]. DIC algorithms are quite complex, and for large data sets (reconstructing a large number of images) DIC is computationally expensive (see [116] for a review and further references). The first proposal to use a two-dimensional Fourier transform procedure to measure δx and δy can be found in [68], and our implementation is based on this approach.

When extended the previous analysis to two dimensions, one must consider two dimensional displacements $\delta_{j,x}(x,y)$ and $\delta_{j,y}(x,y)$. The corresponding measurements will be denoted $\delta_{j,x}[m,n]$ and $\delta_{j,y}[m,n]$, and it will be useful to again consider the Taylor expansion for small displacements. For two dimensional fields, a two dimensional pattern is required. The exact deformed pattern can be modeled as

$$P_t(x,y) = \sin\left(2\pi\vec{k}_0 \cdot \left(\vec{x} + \vec{\delta}_{\vec{\ell},j}\sin(2\pi\vec{\ell}\cdot\vec{x}+\varphi)\right) + \theta_0\right) \tag{A.38}$$

$$\begin{aligned} P_t(x,y) - P_0(x,y) \\ = \frac{1}{2}\sum_{\substack{\ell_x\in B_x \\ \ell_y\in B_y}} \vec{\delta}_{\vec{\ell},t}\Bigg(\sin\left(2\pi\,\vec{\ell}_+\cdot\vec{x}+\varphi_+\right) + \sin\left(2\pi\,\vec{\ell}_-\cdot\vec{x}+\varphi_-\right)\Bigg), \end{aligned} \tag{A.39}$$

where $\vec{\ell}_\pm = (\ell_x \pm k_0, \ell_y \pm k_0)^\top$, and $\varphi_\pm = \varphi \pm k_0$. The same bandwidth arguements that applied to the one-dimensional case apply here as well, except that now we need to make sure that the filter also acomodates the extra dimension of ℓ_y. As it turns out, this is easily accomplished with transformation called the Mclellan transformation [117], and is implemented in Matlab using the `ftrans2` function from the image processing toolbox.

The three core-steps listed in section A.2 are quite general, however in our experimental setup it was sensible to modify the general procedure to better suit our purposes.

The procedure used is as follows:

1. Using the indicator LED described in section 4.3.1, we separate out roughly 500 images of the system before the shaker-driver is initialized. This set of images will be denoted J_0.

2. We perform the Hilbert Transform on the set I_{J_0} extracting the complex x signal, and the complex y signal,

$$I_{J_0} \mapsto \begin{cases} \tilde{I}_{x,J_0} \\ \tilde{I}_{y,J_0} \end{cases} . \tag{A.40}$$

3. Averaging over the set J_0, we obtain our complex reference images in each direction,

$$\tilde{I}_{x,0} = \langle I_{x,J_0} \rangle, \tag{A.41}$$

$$\tilde{I}_{y,0} = \langle I_{y,J_0} \rangle. \tag{A.42}$$

We *define* our stationary interface relative to these reference values, which implies that each of $\tilde{I}_{x,0}$ and $\tilde{I}_{y,0}$ are noise-free.

4. For all other images in the data set, we perform the same Hilbert Transform,

$$I_j \mapsto \tilde{I}_{x,j} \tag{A.43}$$

$$I_j \mapsto \tilde{I}_{y,j}. \tag{A.44}$$

5. The coordinate transformation from the cartesian grid of the camera pixels to radial coordinates is accomplished by interpolating the data as described in section 5.1.2. To save on computational costs, we interpolate the data into a cylindrical coordinate system before extracting the phase differences:

$$\tilde{I}_{x,j}[m,n] \mapsto \tilde{I}_{x,j}[a,b], \tag{A.45}$$

$$\tilde{I}_{y,j}[m,n] \mapsto \tilde{I}_{y,j}[a,b], \tag{A.46}$$

where the indices $[a,b]$ represent the polar coordinate grid defined in 5.1.2.

6. The phase shifts $\delta\phi_{x,j}$ and $\delta\phi_{y,j}$ are computed according to equation (A.18), and phase-discontinuities are removed using an algorithm based on solving the Poisson equation using a discrete cosine transform [118, 119].

7. Using equations (A.18) and (A.35), we obtain the gradient of the height field in the x and y directions

$$\delta\phi_{x,j}[a,b] \mapsto \partial_x h[a,b], \tag{A.47}$$

$$\delta\phi_{y,j}[a,b] \mapsto \partial_y h[a,b]. \tag{A.48}$$

8. To prevent unnecessary integration errors at the boundaries, we want to integrate in the r and θ directions. To do this, we use the differential transformations,

$$\partial_r h = \frac{1}{r}\Big(x\partial_x h + y\partial_y h\Big), \tag{A.49}$$

$$\partial_\theta h = -y\partial_x h + x\partial_y h. \tag{A.50}$$

9. The gradient ∇h is converted to a height field $h[a,b]$ by integrating algebraically in Fourier space. In order to satisfy the periodic boundary conditions inherent in the FFT, we mirror $\partial_r h$ and $\partial_\theta h$ in the radial direction. We denote these $2N_r \times N_\theta$ matrices as $\underline{\partial_\square h}$, and the 2-dimensional FFT as the operator $\mathscr{F}$:

$$\mathscr{F}\underline{h}[k_r, k_\theta] = \frac{-ik_r\mathscr{F}(\underline{\partial_r h}) - ik_\theta\mathscr{F}(\underline{\partial_\theta h})}{k_r^2 + k_\theta^2}. \tag{A.51}$$

When extending the previous analysis to accomodate the physical experiment, the estimated minimum measureable displacement in equation (A.10) needs to be modified to include noise in the images. Since our reference images are noise free by definition, the noise can be modeled using $I_j[m,n]$ alone:

$$I_j[m,n] = +A[m,n]C(n,\vec{\delta}_j[m,n]) + B[m,n] + \sigma_j[m,n], \tag{A.52}$$

where σ_j is some spurious signal unrelated to the interface, and we have defined $\vec{\delta}_j = (\delta_{j,x}, \delta_{j,y})$, and

$$C(n,\vec{\delta}_j) = \cos\left(\frac{2\pi k_0}{N}\Big[n + \delta_{j,x}[m,n]\Big]\right) + \cos\left(\frac{2\pi k_0}{M}\Big[m + \delta_{j,y}[m,n]\Big]\right). \tag{A.53}$$

Here, we have assumed that $k_{0,x} = k_{0,y} \equiv k_0$, and $M = N$.

The exact magnitude and composition of σ_j is hard to estimate theoretically, however a measurement of σ_j from the set of stationary images I_{J_0} should provide a good approximation. This extension to I_j alters our estimation for the minimum measurable displacement. Since the pixel intensity still needs to increase by at least 1, we have

$$\begin{aligned} I_j[m,n] - I_0[m,n] &\simeq \left\lfloor \frac{4Ak_0}{N}\cdot\delta_j[m,n] + \sigma_j[m,n]\right\rfloor \geq 1 \\ &\implies \delta_j[m,n] > \frac{N}{4Ak_0}\left(1 + \sigma_j[m,n]\right). \end{aligned} \tag{A.54}$$

Equation (A.54) tells us that when $\sigma_j \sim 1$ or smaller, the error in our measurements will be mostly due to the quantization noise already presented, and our desired signal once again has the form $\delta_0 = \frac{N}{4Ak_0}$. On the other hand, if $\sigma_j \gg 1$, then the noise that we measure is

$$\tilde{\sigma}_j = \frac{N}{4Ak_0}\sigma_j = \sigma_j\delta_0, \tag{A.55}$$

and the SNR for a general $\delta_j = q_j\delta_0$ can therefore be approximated by

$$\text{SNR} = \frac{q_j\delta_0}{\sigma_j\delta_0} = \frac{q_j}{\sigma_j}. \tag{A.56}$$

At first glance, equation (A.56) seems as though it will reduce sensitivity of the method a great deal, however in the above, we have not considered the form of σ_j at all. In general, σ_j can be written in terms of its Fourier components.

$$\sigma_j[m,n] = \sum_f a_f \, \mathrm{e}^{\frac{i2\pi fj}{N_t}} \sum_{k_x,k_y} b_{k_x,k_y} \, \mathrm{e}^{\frac{i2\pi\vec{k}\cdot\vec{n}}{N}}, \tag{A.57}$$

where $\vec{n} = [m,n]$, and $\vec{k} = [k_x,k_y]$. Because we are careful in our choise of FTP filters, we know that we can preserve the amplitude of the pattern as well as the interface waves measured, and in general, the noise of the system has some spectral spread, usually across all frequencies measured. This means that the noise level drops whenever we filter. The first instance of this is in the FTP filtering, where we keep information only around k_0.

Figure A.12 depicts the noise for a stationary data set with no fluid interface. The lack of fluid interface implies that all variations measured in this data set are inherent in the detection method itself. In what follows, we will assume that the noise is well-approximated by the standard deviation. For a general 3-dimensional variable $\alpha_j[m,n]$, we define

$$\text{std}_j(\alpha_j[m,n]) = \frac{1}{N_j}\sum_j (\alpha - \mu_j)^2, \tag{A.58}$$

where μ_j represents the mean over the index j.

Since the standard deviation is equivalent to the RMS of a signal when the mean is zero, the standard deviation can be represented in the frequency domain as $\frac{1}{\sqrt{2}}\mathscr{F}_t\mathscr{F}_\theta\tilde{I}_{J_0,x}[a,b]$. This allows us to estimate the spectral noise

density of the stationary data, and we can see that with each additional spectral decomposition, we obtain a lower noise-level.

This is important if (for example), we are analysing individual azimuthal modes in the system across a narrow temporal frequency band. In Figure A.12, we can see that after two spectral decompositions, the RMS of the remaining noise spectrum has magnitude of order 10^{-1}.This means that even when considering a finite band of frequencies, the noise present is likely to be negligible.

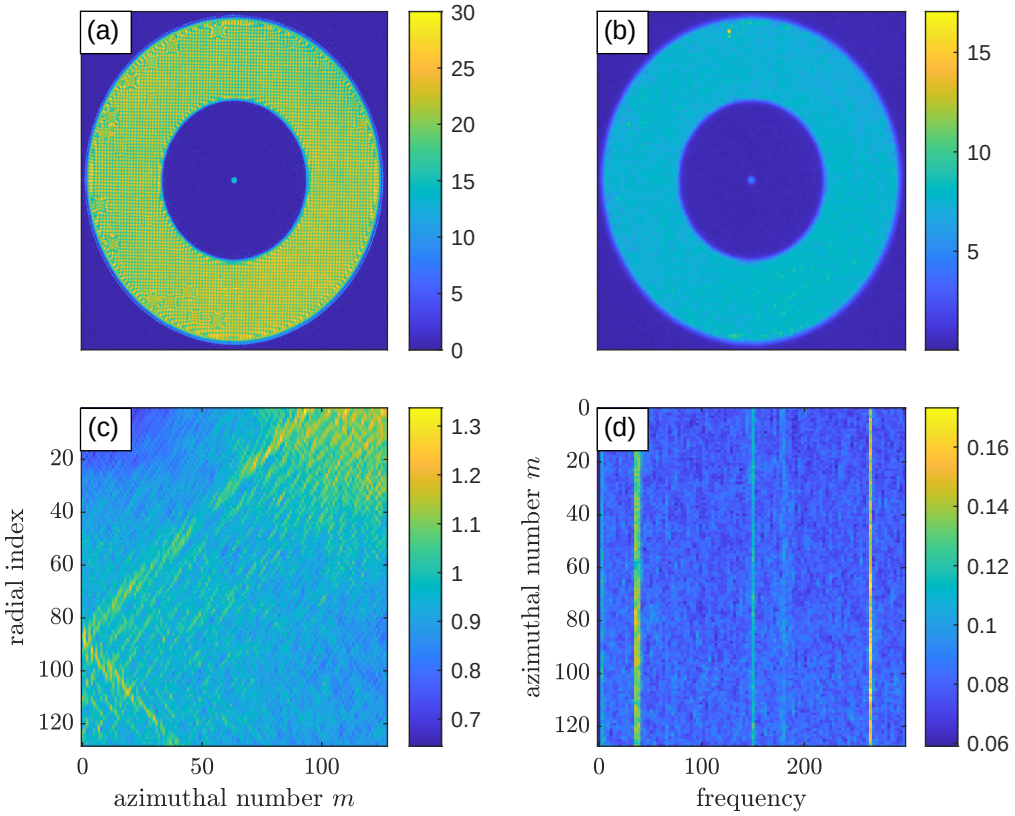

Figure A.12: Panel (a) depicts the standard deviation in time of all of the images in the interface-free data set, I_J.
Panel (b) depicts depicts the standard deviation for the same set of images after we have used the FTP filter in the x direction. Note that the standard deviation of $\tilde{I}_{J,x}$ is greatly reduced.
Panel (c) shows the standard deviation of the same data in polar coordinates, decomposed into its azimuthal Fourier modes: $\text{std}_j\left(\mathscr{F}_\theta \tilde{I}_{j,x}[a,b]\right)$. The vertical axis indicates the radial index. The horizontal axis indicates the azimuthal mode number. Once again, we see that there is a reduction in the noise level as we have defined it. (The apparent signal is not due to an interface, since there is no interface present.)
Panel (d) shows the temporal frequency dependence of $\mathscr{F}_t\mathscr{F}_\theta \tilde{I}_{J_0,x}[a,b]$. The strong signal present at 36 Hz is of unknown origin, though it is thought to be mechanical (and may account for the apparent signal in (c)).

Appendix B: Accelerometer calibration and shaker alignment

In this section, the calibration and vertical alignment procedures for the accelerometer will be detailed. First, the calibration procedure will be detailed. Then, an example of the alignment process will be given.

B.0.1 Calibration procedure

The accelerometer [1] used is a microelectromechanical device designed to have low voltage-drift [2] a very low spectral noise density floor of less than $0.1\text{mV}\sqrt{\text{Hz}}$ [120], as well as a temperature measurement. The accelerometer measures three orthogonal axes which we will label x_1, x_2 and x_3 (corresponding to x, y and z respecively). Each of the three acceleration outputs, from here on denoted V_1, V_2 and V_3 have a voltage offset b_j (corresponding to the voltage measured when the acceleration is zero), and a voltage gain G_j (a linear factor with units of $\frac{V}{\text{ms}^{-2}}$). For a given acceleration $\vec{a}$, the voltage output of the accelerometer will then be

$$\vec{V}_{\text{acc}}(\vec{a}) = \begin{pmatrix} G_1 a_1 + b_1 \\ G_2 a_2 + b_2 \\ G_3 a_3 + b_3 \end{pmatrix}. \tag{B.1}$$

The device used, powered through the voltage regulated power supply should produce an offset of $b_j = 0.900\text{V}$, and a gain of $G_j = \frac{0.0400}{9.81}\frac{V}{\text{ms}^{-2}}$ for each axes [120], howevever even small deviatitions can produce unaccepatable errors when leveling the system. [3] In order to eliminate these errors, a stationary callibration procedure has been developed. The device is mounted onto a box which is precisely made so that opposite faces are parallel, and adjacent faces are orthogonal.

[1] Analog Devices, ADXL354C

[2] Voltage-drift corresponds to very low frequency (periods of hours and days) variations in the output voltage for a constant acceleration.

[3] This was discovered when comparing optical position measurements to the integrated acceleration measurements. Small deviations in the assumed offset and gain values produced large deviations in the integrated position.

Six stationary measurements of the acceleration due to gravity, g are made (one for each face of the box). If we call the input acceleration for each of these measurements $\pm\vec{g}_1$, $\pm\vec{g}_2$ and $\pm\vec{g}_3$, then we can obtain the offsets for each axis by calculating

$$b_j = \frac{1}{2}\big(\vec{V}_{\text{acc}}\left(\vec{g}_j\right) + \vec{V}_{\text{acc}}\left(-\vec{g}_j\right)\big). \tag{B.2}$$

Similarly, we can separate the gain components. We define

$$\vec{G}\left(\vec{g}_j\right) = \frac{1}{2}\big(\vec{V}_{\text{acc}}\left(\vec{g}_j\right) - \vec{V}_{\text{acc}}\left(-\vec{g}_j\right)\big). \tag{B.3}$$

Unless the accelerometer is perfectly aligned with the faces of the callibration box, each axes of the accelerometer will measure some acceleration due to gravity for each orientation of the box. The magnitude of these measurements together must equal the acceleration due to gravity. Considering the jth axis of the accelerometer on its own, we have our equation for the voltage gain in the x_j axis:

$$-gG_j = \sqrt{\vec{G}\left(\vec{g}_1\right)\cdot\hat{x}_j + \vec{G}\left(\vec{g}_2\right)\cdot\hat{x}_j + \vec{G}\left(\vec{g}_3\right)\cdot\hat{x}_j}. \tag{B.4}$$

The values for b_j and G_j must (in theory) only be determined once. In practice, this procedure was repeated at the start of every automation process.

B.0.2 Shaker alignment

The following provides an example of the alignment procedure. There are three adjustment screws, acting as three legs for the shaker (see figure B.1, and section 4.1). One of them is labeled A, the other B, and the third is held fixed. To align the shaker, the system is set to shake at a given frequency.

Defining $a_{\{x,y,z\}}$ to be the acceleration in the x, y, z directions, $\tilde{a}$ to be the Fourier transform of the acceleration, and f_d to be the driving frequency (see figure B.2), we set

$$R_{\tilde{a}}(f_d) = \frac{\sqrt{|\tilde{a}_x(f_d)|^2 + |\tilde{a}_y(f_d)|^2}}{|\tilde{a}_z(f_d)|}. \tag{B.5}$$

After each shake, the alignment screws are adjusted to reduce $R_{\tilde{a}}$. Table B.1 provides an example of this procedure, taken from a lab-book entry dated August, 2020.

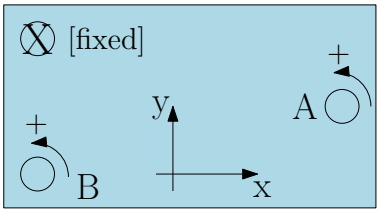

Figure B.1: Leveling screws schematic. The indicated x and y directions represent the approximate x and y axes of the accelerometer. The leveling screws described in section—4.1 can be turned in either direction to reduce $R_{\tilde{a}}$.

(adjustment)	$\tilde{a}_x(f_d)$	$\tilde{a}_y(f_d)$	$R_{\tilde{a}}(f_d)$
(start)	.0063	.0138	.0087
$(B, +1/2)$	.0067	.0182	.0110
$(B, -1)$	.0064	.0069	.0054
$(B, -1/2)$	.0072	.0028	.0044
$(B, -1/2)$	.0085	.0044	.0055
$(B, +1/2)$	.0073	.0022	.0044
$(A, +1/2)$	.0061	.0021	.0038
$(A, +1/2)$	.0071	.0026	.0044
$(A, -1/2)$	.0065	.0028	.0041
(lock screws)	.0065	.0029	.0041

Table B.1: Example alignment steps

The resulting transverse motion in our setup should be compared to the motion of commercially available industrial shakers. ISO 16063 defines 'Methods for the calibration of vibration and shock transducers.' The standards are given for various different types of setups, the most applicale probably being ISO 16063-31: 'Testing of transverse vibration sensitivity.' According to this document [121],

> The amplitude of the transverse acceleration of the fixture due to transverse motion inherent in the vibration exciter shall be less than 1% of the acceleration amplitude in the Z-direction at each of the test frequencies.

However, many companies follow the recommendations of ISO 16063-11, and 16063-21 for high frequencies, where transverse accelerations under 10% are tolerated [122], and this is standard followed by manufacturers [123].

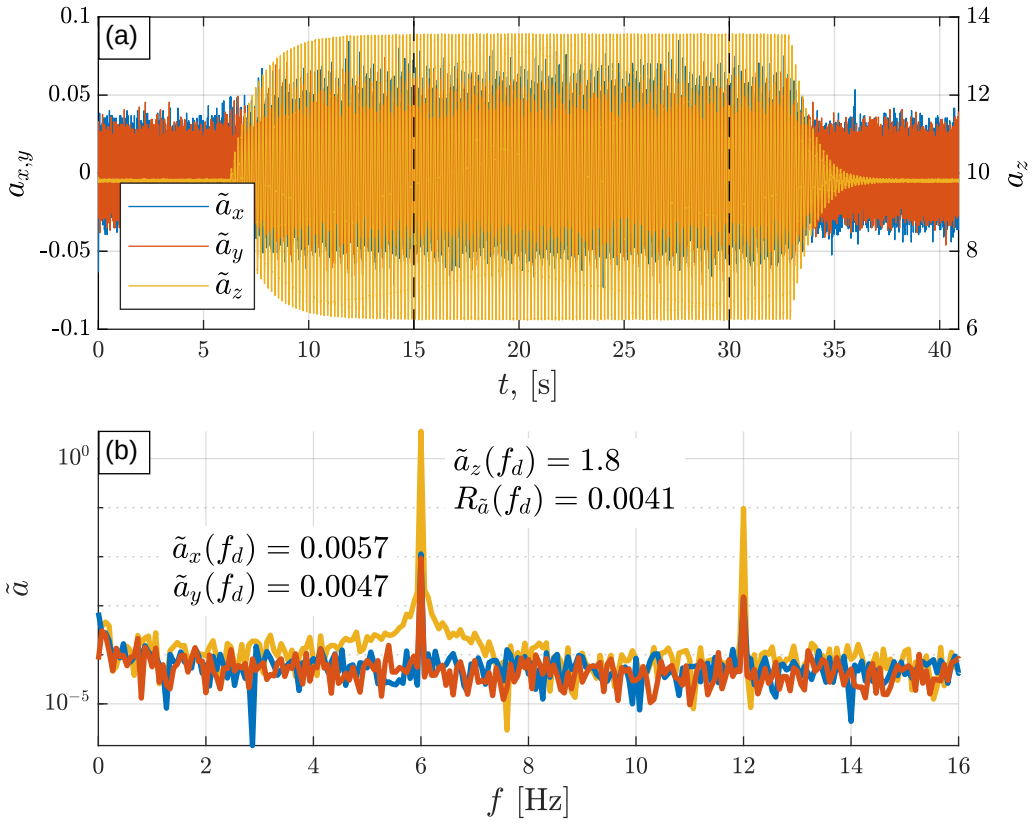

Figure B.2: Accelerometer data from the shaker .
Panel (a) depicts the acceleration versus time for each of the three axis. Note the scale used for $a_{x,y}$ is two orders of magnitude smaller than the scale used for a_z. The vertical, dashed lines indicate the window used for the Fourier transform in panel (b).
Panel (b) depicts the spectral amplitude for each of the three filters. The spectral amplitude of the x, y and z components are listed, along with the ratio $R_{\tilde{a}}$.

Bibliography

[1] S. Dodelson and F Smith. *Modern Cosmology*. Academic Press (London ; 1941-1969), 2003.

[2] H. Kragh and M. Longair. *The Oxford Handbook of the History of Modern Cosmology*. Oxford Handbooks. OUP Oxford, 2019.

[3] Edwin Hubble. A relation between distance and radial velocity among extra-galactic nebulae. *Proceedings of the National Academy of Sciences*, 15(3):168–173, 1929.

[4] A. H. Guth. The Inflationary Universe: A Possible Solution to the Horizon and Flatness Problems. *Phys. Rev. D*, 23:347–356, 1981.

[5] A. D. Linde. A New Inflationary Universe Scenario: A Possible Solution of the Horizon, Flatness, Homogeneity, Isotropy and Primordial Monopole Problems. *Phys. Lett.*, 108B:389–393, 1982.

[6] D Baumann. *The Physics of Inflation*. CreateSpace Independent Publishing Platform, 2015.

[7] Viatcheslav Mukhanov. *Physical foundations of cosmology*. Cambridge University Press, 1 2005.

[8] Ivana Kovacic, Richard Rand, and Si Mohamed Sah. Mathieu's equation and its generalizations: overview of stability charts and their features. *Applied Mechanics Reviews*, 70(2), 2018.

[9] Alex DD Craik. The origins of water wave theory. *Annu. Rev. Fluid Mech.*, 36:1–28, 2004.

[10] L. D. Landau and E. M. Lifshitz. *Fluid Mechanics: Transl. from the Russian by JB Sykes and WH Reid*. Addison-Wesley, 1959.

[11] William Thomson. XLVI. Hydrokinetic solutions and observations. *The London, Edinburgh, and Dublin Philosophical Magazine and Journal of Science*, 42(281):362–377, 1871.

[12] R.P. Feynman, R.B. Leighton, and M. Sands. *The Feynman Lectures on Physics, Vol. I: The New Millennium Edition: Mainly Mechanics, Radiation, and Heat*. Basic Books, 2015.

[13] WG Unruh. Map and Territory in Physics: The Role of an Analogy in Black Hole Physics. In *The Map and the Territory*, pages 233–243. Springer, 2018.

[14] Stephen W Hawking. Black hole explosions? *Nature*, 248(5443):30–31, 1974.

[15] W. G. Unruh. Experimental black hole evaporation. *Phys. Rev. Lett.*, 46:1351–1353, 1981.

[16] Matt Visser. Acoustic black holes: horizons, ergospheres and Hawking radiation. *Classical and Quantum Gravity*, 15(6):1767, 1998.

[17] Matt Visser. Acoustic propagation in fluids: An unexpected example of Lorentzian geometry. *arXiv preprint gr-qc/9311028*, 1993.

[18] Ralf Schützhold and William G. Unruh. Gravity wave analogues of black holes. *Phys. Rev. D*, 66:044019, Aug 2002.

[19] Luis Javier Garay, JR Anglin, J Ignacio Cirac, and P Zoller. Sonic analog of gravitational black holes in Bose-Einstein condensates. *Physical Review Letters*, 85(22):4643, 2000.

[20] Luis Javier Garay, JR Anglin, J Ignacio Cirac, and P Zoller. Sonic black holes in dilute Bose-Einstein condensates. *Physical Review A*, 63(2):023611, 2001.

[21] Carlos Barcelo, Stefano Liberati, and Matt Visser. Analogue gravity from Bose-Einstein condensates. *Classical and Quantum Gravity*, 18(6):1137, 2001.

[22] Carlos Barceló, Stefano Liberati, and Matt Visser. Towards the observation of Hawking radiation in Bose–Einstein condensates. *International Journal of Modern Physics A*, 18(21):3735–3745, 2003.

[23] Grigorii Efimovich Volovik. Black-hole horizon and metric singularity at the brane separating two sliding superfluids. *Journal of Experimental and Theoretical Physics Letters*, 76(5):240–244, 2002.

[24] Grigori Volovik. Effective gravity and quantum vacuum in superfluids. In *Artificial Black Holes*, pages 127–177. World Scientific, 2002.

[25] Thomas G Philbin, Chris Kuklewicz, Scott Robertson, Stephen Hill, Friedrich König, and Ulf Leonhardt. Fiber-optical analog of the event horizon. *Science*, 319(5868):1367–1370, 2008.

[26] F Belgiorno, SL Cacciatori, G Ortenzi, L Rizzi, V Gorini, and D Faccio. Dielectric black holes induced by a refractive index perturbation and the Hawking effect. *Physical Review D*, 83(2):024015, 2011.

[27] S. Weinfurtner, E. W. Tedford, M. C. J. Penrice, W. G. Unruh, and G. A. Lawrence. Measurement of Stimulated Hawking Emission in an Analogue System. *Phys. Rev. Lett.*, 106:021302, Jan 2011.

[28] T. Torres, S. Patrick, A. Coutant, M. Richartz, E. W. Tedford, and S. Weinfurtner. Rotational superradiant scattering in a vortex flow. *Nature Physics*, 2017.

[29] Sam Patrick, Antonin Coutant, Maurício Richartz, and Silke Weinfurtner. Black hole quasibound states from a draining bathtub vortex flow. *Physical review letters*, 121(6):061101, 2018.

[30] Sam Patrick, Harry Goodhew, Cisco Gooding, and Silke Weinfurtner. Backreaction in an analogue black hole experiment. *Physical Review Letters*, 126(4):041105, 2021.

[31] P. O. Fedichev and U. R. Fischer. "Cosmological" quasiparticle production in harmonically trapped superfluid gases. *Physical Review A*, 69(3):033602, 2004.

[32] C. Barcelo, S. Liberati, and M. Visser. Analogue models for FRW cosmologies. *International Journal of Modern Physics D*, 12(09):1641–1649, 2003.

[33] S. Weinfurtner, P. Jain, M. Visser, and C. W. Gardiner. Cosmological particle production in emergent rainbow spacetimes. *Classical and Quantum Gravity*, 26(6):065012, 2009.

[34] P. Jain, S. Weinfurtner, M. Visser, and C. W. Gardiner. Analog model of a Friedmann-Robertson-Walker universe in Bose-Einstein condensates: Application of the classical field method. *Physical Review A*, 76(3):033616, 2007.

[35] S.-Y. Chä and U. R Fischer. Probing the Scale Invariance of the Inflationary Power Spectrum in Expanding Quasi-Two-Dimensional Dipolar Condensates. *"Phys. Rev. Lett."*, 118(13):130404, 2017.

[36] Uwe R. Fischer and Ralf Schutzhold. Quantum simulation of cosmic inflation in two-component Bose-Einstein condensates. *Phys. Rev. A*, 70:063615, 2004.

[37] J.-C. Jaskula, G. B. Partridge, M. Bonneau, R. Lopes, J. Ruaudel, D. Boiron, and C. I. Westbrook. Acoustic analog to the dynamical Casimir effect in a Bose-Einstein condensate. *"Phys. Rev. Lett."*, 109(22):220401, 2012.

[38] C.-L. Hung, V. Gurarie, and C. Chin. From Cosmology to Cold Atoms: Observation of Sakharov Oscillations in a Quenched Atomic Superfluid. *Science*, 341(6151):1213–1215, 2013.

[39] Stephen Eckel, Avinash Kumar, Theodore Jacobson, Ian B Spielman, and Gretchen K Campbell. A rapidly expanding Bose-Einstein condensate: an expanding universe in the lab. *Physical Review X*, 8(2):021021, 2018.

[40] Andreas Finke, Piyush Jain, and Silke Weinfurtner. On the observation of nonclassical excitations in Bose-Einstein condensates. *New Journal of Physics*, 18(11):113017, 2016.

[41] Stéphane Douady. Experimental study of the Faraday instability. *Journal of Fluid Mechanics*, 221:383–409, 1990.

[42] John Bechhoefer, Valerie Ego, Sebastien Manneville, and Brad Johnson. An experimental study of the onset of parametrically pumped surface waves in viscous fluids. *Journal of Fluid Mechanics*, 288:325–350, 1995.

[43] Krishna Kumar and Laurette S Tuckerman. Parametric instability of the interface between two fluids. *Journal of Fluid Mechanics*, 279:49–68, 1994.

[44] S. Chandrasekhar. *Hydrodynamic and Hydromagnetic Stability*. Dover Books on Physics. Dover Publications, 2013.

[45] KM Case and WC Parkinson. Damping of surface waves in an incompressible liquid. *Journal of Fluid Mechanics*, 2(2):172–184, 1957.

[46] M. D. Simon and A. K. Geim. Diamagnetic levitation: flying frogs and floating magnets. *Journal of Applied Physics*, 87(9):6200–6204, 2000.

[47] M. V. Berry and A. K. Geim. Of flying frogs and levitrons. *European Journal of Physics*, 18(4):307, 1997.

[48] M. M. Scase, K. A. Baldwin, and R. J. A. Hill. Rotating Rayleigh-Taylor instability. *Physical Review Fluids*, 2(2):024801, February 2017.

[49] L. Liao and R. J. A. Hill. Shapes and fissility of highly charged and rapidly rotating levitated liquid drops. *"Phys. Rev. Lett."*, 119(11):114501, 2017.

[50] Zack Fifer, Theo Torres, Sebastian Erne, Anastasios Avgoustidis, Richard J. A. Hill, and Silke Weinfurtner. Analog cosmology with two-fluid systems in a strong gradient magnetic field. *Phys. Rev. E*, 99:031101, Mar 2019.

[51] Michael Faraday. On a peculiar class of acoustical figures; and on certain forms assumed by groups of particles upon vibrating elastic surfaces. In *Abstracts of the Papers Printed in the Philosophical Transactions of the Royal Society of London*, pages 49–51. The Royal Society London, 1837.

[52] Thomas Brooke Benjamin and Fritz Joseph Ursell. The stability of the plane free surface of a liquid in vertical periodic motion. *Proceedings of the Royal Society of London. Series A. Mathematical and Physical Sciences*, 225(1163):505–515, 1954.

[53] John Miles and Diane Henderson. Parametrically forced surface waves. *Annual Review of Fluid Mechanics*, 22(1):143–165, 1990.

[54] Zhang Shi, Yi Zhang, Mingchao Liu, Dorian AH Hanaor, and Yixiang Gan. Dynamic contact angle hysteresis in liquid bridges. *Colloids and Surfaces A: Physicochemical and Engineering Aspects*, 555:365–371, 2018.

[55] G. Kaiser. *A Friendly Guide to Wavelets*. Modern Birkhäuser Classics. Birkhäuser Boston, 2010.

[56] Viatcheslav F Mukhanov and Sergei Winitzki. Introduction to quantum fields in classical backgrounds. *Lecture notes-2004*, 2007.

[57] N. D. Birrell and P. C. W. Davies. *Quantum Fields in Curved Space*. Cambridge Monographs on Mathematical Physics. Cambridge University Press, 1982.

[58] Juan Ramon Munoz De Nova, Katrine Golubkov, Victor I Kolobov, and Jeff Steinhauer. Observation of thermal Hawking radiation and its temperature in an analogue black hole. *Nature*, 569(7758):688–691, 2019.

[59] K. A. Baldwin, M. M. Scase, and R. J. A. Hill. The inhibition of the Rayleigh-Taylor instability by rotation. *Scientific reports*, 5:11706, 2015.

[60] JC Picoche, P Rub, and H-J Schneider-Muntau. The high field magnet laboratory of Grenoble. *Journal of Magnetism and Magnetic Materials*, 11(1-3):308–316, 1979.

[61] M. M. Scase, K. A. Baldwin, and R. J. A. Hill. The Rotating Rayleigh-Taylor instability. *arXiv:1603.00675*, 2017.

[62] J. B. Hartle and S. W. Hawking. Wave Function of the Universe. *Phys. Rev. D*, 28:2960–2975, 1983.

[63] J. B. Hartle, S. W. Hawking, and T. Hertog. No-Boundary Measure of the Universe. *Phys. Rev. Lett.*, 100:201301, 2008.

[64] A. Albrecht, P. Ferreira, M. Joyce, and T. Prokopec. Inflation and squeezed quantum states. *Phys. Rev. D*, 50:4807–4820, 1994.

[65] L. P. Grishchuk and Y. V. Sidorov. Squeezed quantum states in theory of cosmological perturbations. In *5th Seminar on Quantum Gravity Moscow, USSR, May 28-June 1, 1990*, pages 678–688, 1990.

[66] C. Gardiner and P. Zoller. *Quantum noise: a handbook of Markovian and non-Markovian quantum stochastic methods with applications to quantum optics*, volume 56. Springer Science & Business Media, 2004.

[67] J. W. Whalen. Physical chemistry of surfaces, fourth edition (Adamson, Arthur W.). *Journal of Chemical Education*, 60(11):A322, 1983.

[68] Sander Wildeman. Real-time quantitative Schlieren imaging by fast Fourier demodulation of a checkered backdrop. *Experiments in Fluids*, 59(6):1–13, 2018.

[69] L.E. Kinsler, A.R. Frey, A.B. Coppens, and J.V. Sanders. *Fundamentals of Acoustics*. Wiley, 2000.

[70] H. Lamb. *Hydrodynamics*. Dover Books on Physics. Dover publications, 1945.

[71] C.K. Batchelor and G.K. Batchelor. *An Introduction to Fluid Dynamics*. Cambridge Mathematical Library. Cambridge University Press, 2000.

[72] P.G. Drazin, N. Riley, London Mathematical Society, and London Mathematical Society Staff. *The Navier-Stokes Equations: A Classification of Flows and Exact Solutions*. Number v. 13 in London Mathematical Society Lecture Note Series. Cambridge University Press, 2006.

[73] L.D. Landau, E.M. Lifshitz, J.B. Sykes, and J.S. Bell. *Mechanics: Volume 1*. Course of theoretical physics. Elsevier Science, 1976.

[74] Vitor B.Silviera. personal communication. 12-06-2021.

[75] Peilong Chen. Nonlinear wave dynamics in Faraday instabilities. *Physical Review E*, 65(3):036308, 2002.

[76] AC Skeldon and AM Rucklidge. Can weakly nonlinear theory explain Faraday wave patterns near onset? *Journal of Fluid Mechanics*, 777:604–632, 2015.

[77] Jean Rajchenbach and Didier Clamond. Faraday waves: their dispersion relation, nature of bifurcation and wavenumber selection revisited. *Journal of Fluid Mechanics*, 777, 2015.

[78] Fritz Ursell. Edge waves on a sloping beach. *Proceedings of the royal society of London. Series A. Mathematical and Physical Sciences*, 214(1116):79–97, 1952.

[79] M. Abramowitz and I.A. Stegun. *Handbook of Mathematical Functions with Formulas, Graphs, and Mathematical Tables*. Applied mathematics series. U.S. Government Printing Office, 1965.

[80] KD Nguyem Thu Lam and H Caps. Effect of a capillary meniscus on the Faraday instability threshold. *The European Physical Journal E*, 34(10):1–5, 2011.

[81] OAV Air Bearings; 20 mm Frictionless Air Bushing Specifications. Accessed again on: 15 Apr. 2021.

[82] Mitsuo Takeda and Kazuhiro Mutoh. Fourier transform profilometry for the automatic measurement of 3-D object shapes. *Applied optics*, 22(24):3977–3982, 1983.

[83] Frédéric Moisy, Marc Rabaud, and Kévin Salsac. A synthetic Schlieren method for the measurement of the topography of a liquid interface. *Experiments in Fluids*, 46(6):1021–1036, 2009.

[84] Inc. Thorlabs. N-BK7 Plano-Convex Lenses. Accessed again on: May 12, 2021.

[85] Datasheet: 60V Two Terminal Constant Current LED Driver PowerDI, (pt. no: AL5809).

[86] daq.createSession. Accessed again on: 18 Apr. 2021.

[87] L. Civitello. *Baking Powder Wars: The Cutthroat Food Fight that Revolutionized Cooking*. Heartland Foodways. University of Illinois Press, 2017.

[88] D.R. Lide. *CRC Handbook of Chemistry and Physics, 85th Edition*. Number v. 85 in CRC Handbook of Chemistry and Physics, 85th Ed. Taylor & Francis, 2004.

[89] Alfa Aesar 1-Butanol, 99%. Accessed again on: 2021-Apr-14.

[90] Fisher Scientific. *Safety Data Sheet: Butanol, Reagent Grade*, 10 2015. Created by Global Safety Management.

[91] ThermoFisher Scientific. *Safety Data Sheet: Propylene Carbonate*, 1 2018.

[92] KR Stone. Environmental profile for propylene carbonate. *US Environmental Protection Agency*, 1998.

[93] Steve" "Mould. Mystery blue and white beads, 2016. Accessed again on: 2021-Apr-12.

[94] B. Boashash. Estimating and interpreting the instantaneous frequency of a signal. I. Fundamentals. *Proceedings of the IEEE*, 80(4):520–538, 1992.

[95] Izrail Solomonovich Gradshteyn and Iosif Moiseevich Ryzhik. *Table of integrals, series, and products*. Academic press, 2014.

[96] C. Gerry and P. Knight. *Introductory Quantum Optics*. Cambridge University Press, 2005.

[97] Silke Weinfurtner, Piyush Jain, Matt Visser, and C W Gardiner. Cosmological particle production in emergent rainbow spacetimes. *Classical and Quantum Gravity*, 26(6):065012, 2009.

[98] Renaud Parentani. personal communication. 13-02-2020.

[99] David Campo and Renaud Parentani. Inflationary spectra and partially decohered distributions. *Physical Review D*, 72(4):045015, 2005.

[100] Christopher J Seeton. Viscosity-temperature correlation for liquids. In *International Joint Tribology Conference*, volume 42592, pages 131–142, 2006.

[101] David R Howell, Ben Buhrow, Ted Heath, Conor McKenna, Wook Hwang, and Michael F Schatz. Measurements of surface-wave damping in a container. *Physics of Fluids*, 12(2):322–326, 2000.

[102] L.D. Landau and E.M. Lifshitz. *Statistical Physics: Volume 5*. Number v. 5 in Courses on Theoretical Physics. Elsevier Science, 2013.

[103] Gian-Carlo Wick. The evaluation of the collision matrix. *Physical review*, 80(2):268, 1950.

[104] Leon Isserlis. On a formula for the product-moment coefficient of any order of a normal frequency distribution in any number of variables. *Biometrika*, 12(1/2):134–139, 1918.

[105] A. Stuart and K. Ord. *Kendall's Advanced Theory of Statistics: Volume 1: Distribution Theory*. Number v. 1; v. 1994 in Kendall's Advanced Theory of Statistics. Wiley, 2009.

[106] A.N. Shiryaev and D.M. Chibisov. *Probability-1*. Graduate Texts in Mathematics. Springer New York, 2016.

[107] August Geelmuyden. personal communication. 02-12-2021.

[108] Daniel M Harris and John WM Bush. Generating uniaxial vibration with an electrodynamic shaker and external air bearing. *Journal of Sound and Vibration*, 334:255–269, 2015.

[109] D.B. Judd. *Color in Business, Science, and Industry*. Aquinas Society of London. Aquinas paper; https://books.google.co.uk/books?id=t4HKf8W5-DMC. Wiley, 1952.

[110] Walt Kester. Taking the Mystery out of the Infamous Formula, "SNR = 6.02N + 1.76dB, " and Why You Should Care. *Analog Devices*, 10 2008.

[111] W. R. Bennett. Spectra of quantized signals. *The Bell System Technical Journal*, 27(3):446–472, 1948.

[112] Peter J Schreier and Louis L Scharf. *Statistical signal processing of complex-valued data: the theory of improper and noncircular signals*. Cambridge university press, 2010.

[113] Lei Huang, Qian Kemao, Bing Pan, and Anand Krishna Asundi. Comparison of Fourier transform, windowed Fourier transform, and wavelet

transform methods for phase extraction from a single fringe pattern in fringe projection profilometry. *Optics and Lasers in Engineering*, 48(2):141–148, 2010.

[114] Jingang Zhong and Jiawen Weng. Spatial carrier-fringe pattern analysis by means of wavelet transform: wavelet transform profilometry. *Applied optics*, 43(26):4993–4998, 2004.

[115] John R Carson. Notes on the theory of modulation. *Proceedings of the Institute of Radio Engineers*, 10(1):57–64, 1922.

[116] Bing Pan. Digital image correlation for surface deformation measurement: historical developments, recent advances and future goals. *Measurement Science and Technology*, 29(8):082001, 2018.

[117] R Mersereau, W Mecklenbrauker, and T Quatieri. McClellan transformations for two-dimensional digital filtering-Part I: Design. *IEEE Transactions on Circuits and Systems*, 23(7):405–414, 1976.

[118] Zixin Zhao. Robust 2D phase unwrapping algorithm. Accessed again on: April 23, 2021.

[119] Zixin Zhao, Hangying Zhang, Changqing Ma, Chen Fan, and Hong Zhao. Comparative study of phase unwrapping algorithms based on solving the Poisson equation. *Measurement Science and Technology*, 31(6):065004, 2020.

[120] Analog Devices; Low Noise, Low Drift, Low Power, 3-Axis MEMS Accelerometers Data Sheet: ADXL354/ADXL355. Rev. B.

[121] *Methods for the calibration of vibration and shock transducers; Part 31: Testing of transverse vibration sensitivity.* Geneva, CH, 2009.

[122] Richard W Bono and Eric J Seller. The effect of high transverse inputs on accelerometer calibration. *Cal Lab-International Journal of Metrology*, 18(1):31, 2011.

[123] Andrew Ramage. personal communication with group member. 08-02-2021.